

Hot Deformation Behavior of AISI Type 316 LN Austenitic Stainless Steel

By
SANTOSH KUMAR
ENGG02201204004

Indira Gandhi Centre for Atomic Research, Kalpakkam

*A thesis submitted to the
Board of Studies in Engineering Sciences*

*In partial fulfillment of requirements
for the Degree of*

DOCTOR OF PHILOSOPHY

of

HOMI BHABHA NATIONAL INSTITUTE

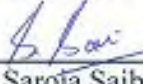
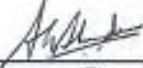


August, 2018

Homi Bhabha National Institute¹

Recommendations of the Viva Voce Committee

As members of the Viva Voce Committee, we certify that we have read the dissertation prepared by Santosh Kumar entitled "**Hot Deformation Behavior of AISI Type 316 LN Austenitic Stainless Steel**" and recommend that it may be accepted as fulfilling the thesis requirement for the award of Degree of Doctor of Philosophy.

 Chairman - Dr. Saroja Saibaba	12/06/2019 Date:
 Guide / Convener - Dr. A. K. Bhaduri	12/6/2019 Date:
 Examiner - Prof. K. S. Suresh	Date: 12.6.19.
 Member 1- Dr. Shaju K Albert	Date: 12.6.19
 Member 2- Dr. K. Velusamy	18.6.19 Date:
 Technology Advisor - Shri Utpal Borah	Date: 14.06.2019

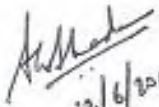
Final approval and acceptance of this thesis is contingent upon the candidate's submission of the final copies of the thesis to HBNI.

I/We hereby certify that I/we have read this thesis prepared under my/our direction and recommend that it may be accepted as fulfilling the thesis requirement.

Date: 12/6/2019

Place: KALPAK KAT

Guide

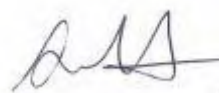

12/6/2019

¹ This page is to be included only for final submission after successful completion of viva voce.

STATEMENT BY AUTHOR

This dissertation has been submitted in partial fulfillment of requirements for an advanced degree at Homi Bhabha National Institute (HBNI) and is deposited in the Library to be made available to borrowers under rules of the HBNI.

Brief quotations from this dissertation are allowable without special permission, provided that accurate acknowledgement of source is made. Requests for permission for extended quotation from or reproduction of this manuscript in whole or in part may be granted by the Competent Authority of HBNI when in his or her judgment the proposed use of the material is in the interests of scholarship. In all other instances, however, permission must be obtained from the author.



Santosh Kumar

DECLARATION

I, hereby declare that the investigation presented in the thesis has been carried out by me. The work is original and has not been submitted earlier as a whole or in part for a degree / diploma at this or any other Institution / University.



Santosh Kumar

List of Publications arising from the thesis

Journal

1. “Dependency of rate sensitive DRX behavior on interstitial content of austenitic stainless steel”, **Santosh Kumar**, Dipti Samantaray, B. Aashranth, Nachiket Kelskar, M. Arvinth Davinci, Utpal Borah, Dinesh Srivastava and A.K.Bhaduri, *Materials Science & Engineering A*, **2019**, 743, 148-158.
2. “Influence of nitrogen on kinetics of dynamic recrystallization in Fe-Cr-Ni-Mo steel”, **Santosh Kumar**, B. Aashranth, Dipti Samantaray, M. Arvinth Davinci, Utpal Borah, A.K.Bhaduri, *Vacuum*, **2018**, 156, 20-29.
3. “Assessing constitutive models for prediction of high temperature flow behavior of austenitic steels with varying nitrogen content”, **Santosh Kumar**, Aashranth B, M. Arvinth Davinci, Dipti Samantaray, Utpal Borah and A.K. Bhaduri, *Journal of Materials Engineering and performance*, **2018**, 27, 2024-2037.
4. “Analysis of elevated temperature flow behavior of a nitrogen enhanced 316L stainless steel under compressive loading”, **Santosh Kumar**, Dipti Samantaray, Utpal Borah and A.K. Bhaduri, *Transaction of Indian Institute of Metals*, **2017**, 70, 1857-1867.
5. “Plastic deformation of SS 316LN: Thermo-mechanical and microstructural aspects”, Dipti Samantaray, Aashranth B, **Santosh Kumar**, M. Arvinth Davinci, Utpal Borah, Shaju K. Albert and A.K. Bhaduri, *Procedia Engineering*, **2017**, 207, 1785-1790.
6. “Hot deformation and microstructural characteristics of nitrogen enhanced 316L stainless steel”, **Santosh Kumar**, Aashranth B, M. Arvinth Davinci, Dipti Samantaray, Utpal Borah and A.K. Bhaduri, *Key Engineering Materials*, **2016**, 716, 317-322.
7. “Investigation on grain boundary character distribution during dynamic recrystallization of austenitic stainless steel during hot deformation”, **Santosh Kumar**, B. Aashranth, Dipti Samantaray, M Arvinth Davinci. Utpal Borah and AK Bhaduri, *Materials Performance and Characterization*, **2019** (Accepted).
8. “Formation of deformation bands in hot worked SS 316LN”, **Santosh Kumar**, B. Aashranth, M. Arvinth Davinci, Dipti Samantaray, Utpal Borah and A.K. Bhaduri, *The Journal of The Minerals, Metals & Materials Society (TMS)*, (Under Review).
9. “Influence of interstitial content on deformability of SS 316LN”, **Santosh Kumar**, M. Arvinth Davinci, Dipti Samantaray, B. Aashranth, Utpal Borah and A.K. Bhaduri, *Journal of Manufacturing Process*, (Communicated).

Chapters in books

1. “Model D8B: An empirical constitutive equation to depict the flow behavior of 316LN stainless steel during instability”, **Santosh Kumar**, Arvinth Davinci, Aashranth B., Dipti Samantaray, Utpal Borah and A.K. Bhaduri, *Thermo-Mechanical Simulation and Processing of Steels*, **2016**, Chapter 28 , 279-287, Viva Books Private Limited.

Conferences

1. “Strain rate effects on dynamic recrystallization during hot deformation of nitrogen enhanced austenitic stainless steel”, **Santosh Kumar**, Dipti Samantaray, Aashranth B, M. Arvinth Davinci, Utpal Borah and A.K. Bhaduri, *Research Scholar Meet on Material science and Engineering of Nuclear Materials (RSM-MSENM 2018)*, May 7-9th, 2018, Kalpakkam, India.
2. “Analysis of Grain Boundary Character Distribution of 316LN Austenitic stainless steel during hot deformation”, **Santosh Kumar**, Dipti Samantaray, Aashranth B, M. Arvinth Davinci, Utpal Borah and A.K. Bhaduri, *EMSI, International Conference XXXVIII Annual Meeting, (EMSI 2017)*, July 17-19th, 2017, Mahabalipuram, India.
3. “Hot deformation characteristics of 316L austenitic stainless steel with varying nitrogen content using Dynamic Material Modeling”, **Santosh Kumar**, M. Arvinth Davinci, Aashranth B, Dipti Samantaray, Utpal Borah and A.K. Bhaduri, *National Metallurgist Day- Annual Technical Meeting (NMD-ATM 2015)*, November 13-16, 2015, PSG Tech, Coimbatore, India.
4. “A comparative study on Model D8A and Arrhenius type constitutive models to predict the high temperature flow behaviour of SS 316L(0.14N)”, **Santosh Kumar**, Dipti Samantaray, Utpal Borah and A.K. Bhaduri, *International Symposium for Research Scholars on Metallurgy, Materials Science and Engineering (ISRS 2014)* December 11-13, 2014, IITM, Madras, India.



Santosh Kumar

Dedicated to

**All the engineers and researchers
who work towards the development of the nation**

Acknowledgements

“Every journey has an end and a good company in a journey makes the way seem shorter”

My Ph.D. journey has come to an end with this thesis successfully with the support and encouragement of various people. I would like to express my thanks to all those people who are responsible for the accomplishment of this thesis work and made it a memorable experience for me. I am privileged for being a research scholar at Indira Gandhi Centre for Atomic Centre (IGCAR), Kalpakkam and getting an opportunity to register Ph.D. in Homi Bhabha National Institute.

Firstly, I would like to express my sincere gratitude to my guide, Dr. A.K. Bhaduri, Director, IGCAR, Kalpakkam, for his continuous support to my Ph.D., for his patience, motivation, and immense knowledge. The door to his office was always open, whenever I needed help. His guidance helped me at all the times of research and writing of the thesis. I could not have imagined having a better guide and mentor for my Ph.D.

Besides my guide, I would like to thank the doctoral committee members: Dr. Saroja Saibaba, Dr. S. Venugopal and Dr. K. Velusamy for their insightful comments and encouragement, but also for the hard question which incited me to widen my research from various perspectives. I am also grateful to Dr. C. Phaniraj for the initial inputs and guidance for my Ph.D. work. I am extremely indebted to Dr. Shaju K. Albert, who has introduced me to this project and supporting till the end. I am thankful to Dr. G. Sasikala and Dr. Anish Kumar for the ease of administrative works and suggestions.

My heartfelt thanks to my technology advisor, Shri. Utpal Borah, for his unconditional moral and technical support during this period.

I am wholeheartedly indebted to Dr. Dipti Samantaray, who has played a crucial role in the shaping of my Ph.D. work, manuscript and thesis. She has consistently allowed this work to be my own work, but steered me in the right direction whenever she thought I needed it. I would remain faithful to her forever for treating me as one of her own family member and mentoring me in both technical and mental support.

My sincere thanks to Dr. G. Amarendra, Dr. T.S. Lakshmi Narasimhan and Dr. M. Saibaba for all the administrative work and accommodations at JRF Enclave. I also take this opportunity to sincerely acknowledge to Science and Engineering Research Board for International travel grant to attend a conference at Krakow, Poland.

Most of these results in the present work would not have been possible without the close collaboration of other groups and institutions. I would like to acknowledge Dr. Dinesh Srivastava, Chairman, NFC and Shri. Nachiket Keskar, BARC for timely help received in EBSD characterization. I would also like to extend my acknowledgments to Shri. V. Ganesan from MDTD, Dr. Atanu Chaudhri from IISC, Dr. Arup Das Gupta and Shri. Pradyumna Parida

from PMG and UGC-DAE for EBSD characterization. I sincerely thank Dr. Amitha Pandiyan from MSG for his help in TEM characterization. I would acknowledge my friends from IISC, Rajshekar for XRD characterization and Dr. K.G. Raghavendra for sample preparations on time, even in their busy schedule.

I sincerely acknowledge Shri. M. Arvinth Davinci whose expertise in mechanical testing machines is the prime reason for the smooth conduct of my Ph. D. experimental works. I expand my thanks to Shri. B. Aashranth, my colleague and a friend for having brain-storming discussions, implementing ideas and help in manuscript preparations. I thankfully record the help received from Sameer Kumar Paul in metallography. I am thankful to Gaddam Arunkumar who had been an excellent junior and also has an important contribution in my thesis work. I would also like to thank Dr. N. L. Parthasarathi, A. Arasu and Sivapatham from MFTS section for constant help and support.

I would like to extend my gratitude to Nani Babu, Shashank, David, Manmath, Saroj, Purushotham and Syed for their support and suggestions. I would like to thank all my teachers and well-wishers who have helped me to come to this position.

I am indebted to all my seniors -cum friends Devi, Karthick, Kalyan, Manas, Mahendran, Masi, Prema, Ravi , Sharath, Sanjay, Sadu, Thangam, Samba and Subu for their support and encouragement. I also acknowledge my batchmates, Naveen, Gopi, Sumathi, Srinu, Abuthair, Bharath, Bala, Aishwariya, Greeshma, Sivadasan, Chandan, Preethi, Rama and Yadagiri for constantly supporting me.

I also thanks my juniors Radi, Lax, Vairavel, Panda, Nila, Irshad, Manoj, Shivang , Nidhin, Sumathi, Zaibudeen, Anuj, Sai, Raghavendran, Suresh, Siva, Aditya, Ronit, Chandan Reddy, Nagendra, Balaji, Shiva, Sahoo, Arnab, Teena, Anisha, Vikas, Darpan, DJ, Prashanth, Rajneesh, Anoop, Sumit, Revanth ,Suman, Bala, Sarvajith, Uday ,Saitya, Paul, Vaishu, Valli, Lavanya, Manu, Bijay ,Thiru and Barik for bearing me and keeping me active all these days. IECL, EBL, Jackie journey and Kudla club were the best part to overcome my Ph.D. frustrations and stay motivated.

With great affection, I recognize and appreciate the role of Shashwat, Vipin, CV, Rohith, Sumana, Pavan, Sravs, Mady, Suma, Smita and Lavanya as true friends in my Ph.D. life. These people have shared my happiness and sorrow, due to which I never felt homesickness at Kalpakkam.

Finally, I express my deepest gratitude to my parents and family members. My Dad (Suresh) and Mom (Savithri) have always been supportive, encouraging and trusting me to finish my Ph.D. I am extremely fortunate to have devilish sis's (Baghya, Pavi and Sumi), who has always been with me in my hard times and regenerates me every time. This accomplishment would not have been possible without them. Thank you.

Santosh Kumar

Synopsis

The prime objective of the work is to explain the effect of nitrogen content on flow behavior and microstructural evolution of 316LN Austenitic Stainless Steel (SS) during hot deformation. In view of the above, three variants of 316LN SS containing 0.07 wt.% (7N), 0.11 wt.% (11N) and 0.22 wt.% (22N) nitrogen have been studied using hot isothermal uniaxial compression test in the temperature range of 1123-1473 K and at constant true strain rates of 0.001, 0.01, 0.1, 1 and 10 s⁻¹. In this work detailed microstructural investigation was carried out on the deformed specimens using optical microscopy. Selected specimens were characterized using Electron Back Scattered Diffraction (EBSD) and Transmission Electron Microscopy (TEM) and X-ray Diffraction technique. This study elucidates influence of nitrogen on workability and hot deformation behavior on the basis of flow behavior analysis and the microstructural findings.

Flow behavior analysis indicates that with increase in nitrogen content, the resistance of the material to deformation increases. To describe flow behavior of 316LN SS with various nitrogen contents, utility of different constitutive models such as Strain compensated Arrhenius model (SCA), Modified Johnson–Cook (MJC) model, model D8A and Artificial Neural Network (ANN) has been evaluated from the perspective of alloy development. However, none of the models found to comprehensively describe the flow behavior of 316LN with varying nitrogen content. On the basis of the flow behavior analysis N-amended D8A model is proposed, which takes nitrogen content along with the process parameters such as temperature, strain and strain rate into account. The work provides detailed insights into the usual statistical

error analysis technique and frames five additional criteria which must be considered when a model is analyzed from the perspective of alloy development.

With the addition of nitrogen the critical condition for DRX nucleation is accelerated, however, the grain growth is delayed. The association between the chemical composition of a material, its stacking fault energy (SFE) and dynamic recrystallization (DRX) behavior is established. Higher nitrogen content suppresses the strain rate sensitivity of DRX in the steel. The alloy with minimum interstitial content exhibits a sluggish DRX behavior in the strain rate domain $0.1-1s^{-1}$. The rate-dependency of nucleation is explained on the basis of interstitial content, which changes the SFE. This investigation also elucidates the rate- dependent grain growth.

The study also reports significant effect of nitrogen on workability of 316LN SS. New deformation maps were developed to study the workability of 316LN with varying nitrogen content, strain and temperature. 7N variant is found suitable for majority of high temperature deformation processes such as rolling, forging and extrusion. However, 11N and 22N variants of 316LN SS can be safely used for forgings where low reduction ratio is achieved in one step. With increase in nitrogen content in 316LN SS, the steel becomes more prone to form adiabatic shear bands when deformed at higher strain rates. The critical criterion for shear band formation is easily satisfied at low strain levels. On the basis of the micro structural observations, a mechanism of ASB formation in 316LN SS is proposed.

The results of the current investigation can be taken as input for optimization of processing variables for in order to achieve the desired property during fabrication of 316LN SS.

Contents

Synopsis	i
Contents	iii
List of Figures	vii
List of Tables	xii
Nomenclature	xiii
Chapter 1. Introduction	1-3
1.0. Objective	2
1.1. Thesis Layout	3
Chapter 2. Review of Literature	4-17
2.0. Preamble	4
2.1. Importance of nitrogen as interstitial element on austenitic stainless steel	4
2.2. Effect of nitrogen content on high temperature flow behavior and constitutive analysis	7
2.3. Effect of nitrogen content on microstructural evolution	10
2.4. Influence of nitrogen content on workability of material	13
2.5. Metallurgical instabilities during processing at high strain rates	15
2.6. Scope of the present study	16

Chapter 3.	Experimental Details	18-24
3.0.	Preamble	18
3.1.	Material	18
3.2.	Hot Isothermal Compression Test	19
3.3.	Microstructural Characterization	21
3.3.1.	Optical and Confocal Microscopy	21
3.3.2.	Electron Backscattered Diffraction	21
3.3.3.	Transmission electron Microscopy	24
3.3.4.	X-Ray diffraction	24
Chapter 4.	Flow behaviour analysis of 316LN stainless steel at elevated temperature	25-52
4.0.	Preamble	25
4.1.	Deformation behaviour of different variants of 316LN SS	25
4.2.	Constitutive modeling	31
4.2.1.	Strain Compensated Arrhenius Model (SCA)	32
4.2.2.	Modified Johnson-Cook Model (MJC)	33
4.2.3.	Model D8A	34
4.2.4.	Artificial Neural Network (ANN)	36
4.3.	Various aspects of thermo-viscoplastic constitutive models	37
4.3.1.	Statistical Evaluation	37
4.3.2.	Ability to correctly represent flow instabilities in the tested domain	40

4.3.3. Provision for easy integration of additional variables: integration of chemical composition	43
4.3.4. Possibility of usage of the model for extrapolation	47
4.3.5. Ease of usage	48
4.3.6. Ability to connote the metallurgical properties	49
4.4. Conclusions	52
Chapter 5. Role of nitrogen on dynamic recrystallization in 316LN during hot working	53-75
5.0. Preamble	53
5.1. DRX characteristics	53
5.2. Temperature sensitivity of DRX in 316LN	54
5.3. Strain rate sensitivity of DRX in 316LN	57
5.3.1. Prediction of SFE in hot working domain by varying interstitial content	60
5.3.2. Correlation between SFE and DRX	63
5.4. Effect of nitrogen content on grain size evolution	70
5.5. Influence of nitrogen on special boundaries	71
5.6. Conclusions	74
Chapter 6. Effect of nitrogen content on workability of 316LN SS	76-86
6.0. Preamble	76
6.1. Processing Maps	76
6.2. Nitrogen content and workability domain	82
6.3. Conclusions	85

Chapter 7.	Flow instabilities in 316LN austenitic stainless steel at high strain rate	87-108
7.0.	Preamble	87
7.1.	Instability at high strain rates : Adiabatic Shear banding (ASB)	87
7.1.1.	Critical strain for formation of adiabatic shear bands	88
7.2.	Intensity of the adiabatic shear band	93
7.2.1.	Microstructural changes as a function of temperature in ASB	93
7.2.2.	Effect of strain rate on microstructures inside ASBs	97
7.2.3.	Effect of geometry on ASB formation and propagation	99
7.2.4.	Influence of nitrogen content on ASB formation	101
7.3.	Mechanism behind the formation of ASB in hot isothermal forging	103
7.4.	Conclusions	108
Chapter 8.	Conclusions and Future Work	109-111
8.0	Conclusions	109
8.1	Suggestions for future work	111
References		112-125
Appendix		126-131

List of Figures

Figure No.	Figure Caption	Page No.
2.1	Schematic effect of main alloying elements used for high nitrogen austenitic stainless steels on austenite stability, pore formations and nitrogen solubility.	6
2.2	A typical flow curves showing the DRV curve and DRX curve with respect to stress and strain.	10
2.3	Flow chart showing various types of DRX.	11
3.1	High temperature constant true strain rate compression testing machine.	22
3.2	Schematic illustration of the experimental procedure. Typical appearance of sample before and after deformation.	22
3.3	Inverse pole figure (IPF) maps of (a) 7N, (b) 11N and (c) 22N variants in solution-annealed condition.	23
4.1	True stress – strain curves of 7N at (a) 1123K, (b) 1223K, (c) 1323K and (d) 1423K at different strain rates.	27
4.2	True stress – strain curves of 11N at (a) 1123K, (b) 1223K, (c) 1323K and (d) 1423K at different strain rates.	28
4.3	True stress – strain curves of 22N at (a) 1123K, (b) 1223K, (c) 1323K and (d) 1423K at different strain rates.	29
4.4	Figure 4.4: Variation of flow stress with temperature at a)7N, b)11N, c)22N at 0.6 strain. Marked regions represent the instabilty zone.	30
4.5	True stress – strain curves of 0.1s^{-1} at (a) 1123K, (b) 1223K, (c) 1323K and (d) 1423K.	30
4.6	Experimentally obtained and SCA-predicted flow curves for 7N and 22N grades of 316LN in the temperature domain of 1123-1423K at strain rate (a) 0.01 s^{-1} and (b) 1 s^{-1} .	35

4.7	Experimentally obtained and MJC-predicted flow curves for 7N and 22N grades of 316LN in the temperature domain of 1123-1423K at strain rate (a) 0.01 s^{-1} and (b) 1 s^{-1} .	35
4.8	Experimentally obtained and model D8A-predicted flow curves for 7N and 22N grades of 316LN in the temperature domain of 1123-1423K at strain rate (a) 0.01 s^{-1} and (b) 1 s^{-1} .	35
4.9	Artificial Neural network architecture used in the present study	36
4.10	Experimentally obtained and ANN-predicted flow curves for 7N and 22N grades of 316LN in the temperature domain of 1123-1423K at strain rate (a) 0.01 s^{-1} and (b) 1 s^{-1} .	36
4.11	Statistical evaluation of different models using the same dataset. Numbers on arrows indicate deviation from ideal model.	41
4.12	Comparison of experimentally obtained and predicted flow curves by various models in unstable domain for (a) 7N and (b) 22N grades of 316LN.	42
4.13	Comparison of experimentally obtained and predicted flow curves by N-amended MJC, N-amended D8A and ANN model for (a) 11N at 0.001s^{-1} and (b) 11N at 1s^{-1} and (b) 14N at 0.1s^{-1} .	46
4.14	Radar chart comparing performance of different models on the basis of six factors.	51
5.1	Typical θ - σ plot obtained from flow curves to determine the various stress parameters.	55
5.2	(a) θ - σ plot at different temperatures and (b) critical strain vs temp obtained at 0.001s^{-1} strain rates for 7N, 11N and 22N variants of 316LN SS.	55
5.3	Grain Orientation Spread maps of partitioned DRX grains for 22N variant deformed at strain rate 0.001 s^{-1} at , (a) 1123K and (b) 1423K where the colored region represents DRX grains.	56
5.4	Variation of critical strain with strain rate for different variation of nitrogen content at 1323K.	56

5.5	GOS maps of partitioned DRX grains for 7N variant deformed at 1323 K, (a) 0.001 s^{-1} , (b) 1 s^{-1} and (c) 10 s^{-1} where the colored region represents DRX grains.	59
5.6	GOS maps of partitioned DRX grains for 11N variant deformed at 1323 K, (a) 0.001 s^{-1} , (b) 1 s^{-1} and (c) 10 s^{-1} where the colored region represents DRX grains.	59
5.7	GOS maps of partitioned DRX grains for 22N variant deformed at 1323 K, (a) 0.001 s^{-1} , (b) 1 s^{-1} and (c) 10 s^{-1} where the colored region represents DRX grains.	59
5.8	Variation of DRX fraction with strain rate for 7N, 11N, 22N variants at 1323K.	60
5.9	Stacking fault energy with varying interstitial content at various temperature.	65
5.10	Change in stacking fault probability and micro-strain (ϑ) values on (111) plane for 7N, 11N and 22N variants deformed at 1323K.	66
5.11	Variation of average DRX grain size with nitrogen (a) at various temperatures at 0.001 s^{-1} (b) at various strain rate at 1323K with a confidence interval of 95%.	71
5.12	Variation of average DRX grain size with strain rate at 1323K (with a confidence interval of 95%).	72
5.13	Twin Boundary frequency of 7N, 11N and 22N steels at 0.001 s^{-1} .	72
6.1	Processing maps of 7N at various temperature and strain rates at a true strain of 0.65. The marked region indicates the region of flow localization and shear bands.	79
6.2	Processing maps of 11N at various temperature and strain rates at a true strain of 0.65. The marked region indicates the region of flow localization and shear bands.	80
6.3	Processing maps of 22N at various temperature and strain rates at a true strain of 0.65. The marked region indicates the region of flow localization and shear bands.	81

6.4	Processing maps of 316LN SS at various temperature and nitrogen content at (a) $0.001s^{-1}$, (a) $0.01s^{-1}$, (c) $1s^{-1}$ and (d) $10s^{-1}$ at a true strain of 0.65.	84
6.5	Processing maps of 316LN SS at various strain and nitrogen content at (a) $1s^{-1}$ and (b) $10s^{-1}$ at temperature 1423K.	84
7.1	Confocal micrograph of cross section view of compressed sample (a) X shaped banding (b) heavily densed banding in one direction.	91
7.2	Variation of ϵ_{ASB} at different temperature with increasing nitrogen content.	91
7.3	Experimentally measured and calculated values of adiabatic temperature rise during deformation at different temperature for (a) 7N and (b) 22N at $10s^{-1}$.	92
7.4	Relationship between peak strain(ϵ_p) and ϵ_{ASB} in 7N grade at various temperature.	92
7.5	Optical microstructures of 7N at $10s^{-1}$ (a) 1123K (the box indicates heavily deformed and highly localized region); (b) 1223K (the box shows the fine nucleation) (c) 1323K and (d) 1423K.	95
7.6	Microstructure of 7N grade steel at $10s^{-1}$, taken at temperature : (a) 1123K, IPF map (b) 1123K, intragranular misorientation map, (c)1323K, IPF map, (d) 1323K, intragranular misorientation map.	96
7.7	Optical microstructures of 7N at 1123K (a) $0.001s^{-1}$ (b) $0.1s^{-1}$ (pockets of strain localizations are marked and (c) $10s^{-1}$ (the arrow indicates the shear banding).	97
7.8	Inverse pole figure mapping of 7N at 1123K at a) $0.01s^{-1}$ (arrow indicates the necklace structure) and b) $10s^{-1}$ (arrow indicates the fine DRX grains). The black lines indicates the grain boundaries $>15^\circ$ and red lines indicates	98

	grainboundries $>10^\circ$. TEM images of 7N at 1123K at c) $0.01s^{-1}$ and d) $10s^{-1}$.	
7.9	Microstructures of 7N at 1123K, $10s^{-1}$ at 25X and 500X : (a,b) rectangular cross-section, (c,d) circular cross-section ; (e,f) square cross-section.	101
7.10	Inverse pole figure mapping and TEM images at 1123K, $10s^{-1}$ at 0.5 strain of (a, b) 7N and (c, d) 22N respectively.	102
7.11	Band contrast imaging of 7N at 1123K, $10s^{-1}$ at 0.3 strain. The arrows indicates the formation of micro bands.	105
7.12	EBSD maps of 7N at 1123K, $10s^{-1}$ at 0.5 strain: (a) IPF map and (b) Grain boundary map. The marked area shows the formation of low angle grain boundaries along the bandings.	105
7.13	Schematic illustration of the formation process of nucleation of sub grain inside the microbands in a grain in ASB region.	106
7.14	TEM images with SAD pattern of 7N at 1123K, $10s^{-1}$ at (a) 0.3 strain and (b) 0.5 strain (arrow indicates the secondary twins).	106

List of Tables

Table No.	Table Caption	Page No.
2.1	Typical ranges of strain rates of various manufacturing process.	14
3.1	Chemical composition of 316LN (wt. %).	18
3.2	Test conditions used for hot compression test in the present study.	20
4.1	Coefficient of the polynomial functions shown in Eq.1 for the grades 7N and 22N.	33
4.2	Material constants of MJC model for the grades 7N and 22N.	34
4.3	Material constants of Model D8A for the grades 7N and 22N.	34
4.4	Statistical parameters obtained for predictions by various models.	41
4.5	Material constants for N-amended D8A.	45
4.6	Material constants for N- amended MJC model.	46
4.7	Statistical parameters obtained for predictions by various models.	47
5.1	Experimental and predicted values of stacking fault energy of 7N, 11N and 22N at room temperature.	63
7.1	Thermal conductivity values (W/mK) for 7N, 11N and 22N at various temperatures calculated from JMATPRO 7.0.	89
I	Values of various parameters and functions used for the thermodynamic calculation of stacking fault energy.	130

Nomenclature

a	Lattice parameter
α'	Flow localization parameter
α, n', A	Material constants for SCA
α_p	Stacking fault probability
$A_1, A_2, A_3, A_4, \lambda_1, \lambda_2$	Material constants for MJC
β	Magnetic moment
$B_1, B_2, B_3, B_4, B_5, B_6, B_7, \mu_1, \mu_2, \mu_3$	Material constants of N-amended MJC
β_{ASB}	Fraction of plastic work converted to heat
C_p	Specific heat
ΔG	Free energy
$\Delta G_{chemical}^{\gamma \rightarrow \zeta}$	Free energy change due to chemical segregation due to Suzuki interaction
$\Delta G_{surface}^{\gamma \rightarrow \zeta}$	Free energy change due to surface segregation between matrix and stacking fault
$\Delta G_{elastic}^{\gamma \rightarrow \zeta}$	Free energy change due to elastic segregation effect due to difference in atomic size
$\Delta G_{bulk}^{\gamma \rightarrow \zeta}$	Change in bulk free energy
$\Delta G_{Mag}^{\gamma \rightarrow \zeta}$	Change in free energy due to magnetic contribution
$\Delta G_{Seg}^{\gamma \rightarrow \zeta}$	Change in free energy due to segregation,
$\Delta G_{(sub)}^{\gamma \rightarrow \zeta}$	Free energy change contribution from substitutional elements
$\Delta G_{(int)}^{\gamma \rightarrow \zeta}$	Free energy change contribution from interstitial elements

ΔU_{ij}	Change in interaction energy between λ and each substitutional alloying element pair $i-j$
D_1	Yield stress
D_2	Strain hardening coefficient
D_3	Represents the absolute effect of temperature
D_4	Represents the coupled effect of temperature and strain
D_5	Signifies the absolute effect of strain rate
D_6	Represents the coupled effect of temperature and strain rate
ΔT	Adiabatic temperature rise
ε	True Strain
ε^{r*}	Dimensionless parameter
ε'_0	Reference strain rate
ε'	Strain rate
$E_1, E_2, E_3, E_4, E_5, E_6, E_7, m_1, m_2$	Material constants of N-amended D8A
ε_{ASB}	Critical strain for initiation of adiabatic shear band
ε_χ	Critical strain
ε_ρ	Average critical strain for recovery
G'	Shear modulus
G	Power content
γ	FCC
γ_{SFE}	Stacking fault energy
η	Power dissipation efficiency
I	Intercept
J	Power co-content
J_{max}	maximum value of J
K'	Constant

Λ	Denotes the interaction energy between nitrogen atom and dislocations in FCC matrix
L	average crystallite size
λ	wavelength
m	Strain rate sensitivity of the material
ν	Poisson's ratio
ϑ	Microstrain
N	Symbolizes the nitrogen content in % (by weight)
n	Strain hardening exponent
N'	Total number of experimental data points
N_A	Avogadro number
P	Power Dissipated
p	Fraction of magnetic enthalpy absorbed above T_{Neel}
θ	Work hardening rate
θ_b	Bragg's angle
Q	Activation Energy
R	Correlation coefficient
R'	Universal gas constant
ρ_{steel}	Density of steel
S	Slope
σ	True Stress
σ_{exp}	Experimental flow stress
σ_{pre}	Predicted flow stress
$\overline{\sigma_{pre}}$	Mean predicted stress
$\overline{\sigma_{exp}}$	Mean experimental stress values
σ_χ	Critical stress
SD	Standard deviation

σ_{IE}	Interfacial energy in the faulted region
σ_{π}	Peak stress
σ_{sat}	Saturation stress
σ_{ss}	Steady state stress
t	Time
T	Temperature
T_{Neel}	Neel temperature
t_c	Time threshold
Tr	Reference temperature
V	Molar volume of the alloy
$\Omega_{ij}^{\gamma \rightarrow \zeta}$	Excess free energy
ζ	HCP
$\xi(\varepsilon')$	Instability parameter
X_g^i	Weights assigned to lattice distortion characterized by microstrain
X_T^i	Weights assigned to temperature
X_t^i	Weights assigned to time
χ_i	Molar fraction of i^{th} element
$\chi_{N(Seg)}$	Fraction of nitrogen segregated in the faulted region
χ_{λ}	Mole fraction of the interstitial element ‘ λ ’
Ψ	Molar surface density of (111)

Chapter 1

Introduction

Electricity is one of the fundamental necessities of people to lead a normal life. Recently, Indian Brand Equity Foundation (IBEF) has indexed India, as the third largest producer and fourth largest consumer of electricity [1]. However, the per capita electricity consumption is still below the world average. The requirement of energy security and urgent necessity to minimize the environmental impact has led us to maximize the utilization of every possible alternate to the fossil fuel. Nuclear power is one of the reliable sources of clean power. To maximize the utilization of the heavy metal resources of the country in a sustainable way, the Indian nuclear program has been planned to have three stages [2]. The first stage is about building Pressurized Heavy Water Reactor (PHWR) with natural uranium (U) as the fuel and the technology is now well established. The second stage is about using fast breeder reactor (FBR) where the plutonium (Pu) produced from the PHWR operation is to be utilized as fuel. The FBRs are to be used to breed Pu from ^{238}U and ^{233}U from abundantly available thorium in the country. Ultimately, the ^{233}U produced from the second stage would be utilized as fuel in the advanced heavy water reactors planned in the third stage.

Worldwide, type 316L austenitic stainless steel (SS) has been chosen as major material for FBR structural components like main vessel, intermediate heat exchange and grid, as it offers good high temperature strength, liquid sodium compatibility, weld ability [3] and corrosion resistance in radioactive environment [4]. However, for Indian Prototype Fast Breeder Reactor (PFBR), the 316L SS is replaced with 316LN SS (0.08wt. %N) [2], as the addition of nitrogen (N) enhances the room temperature strength by interstitial strengthening [5]. Addition of nitrogen also improves creep strength [6],

fatigue [7] and corrosion resistance [8] of the steel. It is envisaged to increase the present design life of the reactor i.e. from 40 to 60 years in order to achieve maximum return of capital investment. This essentially requires in further improvement in the above mentioned properties. To achieve these requirement, various grades of nitrogen enhanced austenitic stainless steel containing 0.07 to 0.22 wt. % N are developed and the properties are currently being investigated [9]. As any steel under development has to be finally fabricated into a component, along with obtaining the mechanical properties that is needed for component design, it is also necessary to optimize the processing parameters that is required for thermomechanical processing. Usually, thermo-mechanical processes, such as extrusion, rolling and forging, are used for fabrication of the reactor structural components. Prior to fabrication of the large reactor structural components, the thermo-mechanical processes need to be carefully designed to minimize production of defective components. Given the criticality and reliability demanded by these applications, a thorough understanding of plastic deformation [10, 11] and microstructural mechanisms [12, 13] in 316LN SS acquires special importance. In view of the above, the present thesis deals with the analysis of three grades of nitrogen (N) enhanced developed 316LN austenitic stainless steel containing 0.07, 0.11, and 0.22wt. % N.

1.0. Objective

The objectives of the present work are as follows:

- To understand the flow behavior and to find/ develop a suitable material model to depict the flow stress of 316LN SS with varying nitrogen content.
- To study the influence of nitrogen content in 316LN SS on its dynamic recrystallization (DRX) behavior.

- To identify the effect of nitrogen content on optimum workability domain of 316LN SS for thermo-mechanical processing.
- To characterize the flow instability in 316LN SS that occurs during deformation at high strain rates.

1.1. Thesis Layout

The present thesis work aims to study the effect of nitrogen content during hot deformation studies of 316LN austenitic stainless steel over a wide range of temperature and strain rate. The first part of the thesis is dedicated for analysis of flow behavior and optimizing the processing domains. The later part is devoted to understand the underlying microstructural mechanism occurring during hot workability. Literatures available on hot deformation behavior of materials are briefly reviewed in Chapter 2. The alloys composition, experimental procedures and characterization details are listed in Chapter 3. Chapter 4 deals with the effect of nitrogen content on flow behavior. On the basis of the flow behavior analysis a constitutive equation has been developed, which incorporates the effect of process parameter and nitrogen content. The DRX behavior of 316LN austenitic stainless steel with varying nitrogen contents are studied and mechanism are discussed in Chapter 5. Chapter 6 presents the influence of nitrogen content on the workability of the steel through processing maps. Chapter 7 provides the results of investigation carried out on the formation and development of Adiabatic Shear Banding (ASB) during hot deformation of 316LN SS at higher strain rates ($10s^{-1}$). The final chapter, summarizes the salient features of the present thesis work and the future scopes for further research.

Chapter 2

Review of Literature

2.0. Preamble

This chapter presents a review of literature related to the current investigation. First part of the chapter describes evolution of 316LN SS and various modeling techniques used to describe constitutive behavior. The second part reviews about the various mechanisms associated with the deformation at elevated temperatures.

2.1. Importance of nitrogen as interstitial element on austenitic stainless steel

Austenitic stainless steels (SS) are widely used in various industrial sectors and strategic sectors as well. The most commonly used SS is the 300 grade austenitic stainless steel. These alloys typically contain from 16-20% Cr, 8-20% Ni and 1.5% of Mn. Other elements such as Ti, Nb and Mo are added to improve high temperature properties of the steel. 316 SS is one such variety which contains 2 wt.% molybdenum along with 18 wt. % Cr, 12 wt.% Ni and 0.06 wt. % C [14]. However, it was seen that these steels are prone to sensitization. In order to avoid sensitization the carbon content in the alloy is restricted to 0.03 wt. %. The low carbon variety 316L SS, however, exhibited inferior mechanical properties compared to 316 SS. On one hand to achieve high mechanical strength and on the other hand to avoid sensitization, a new variant 316LN SS was developed by partially substituting carbon with nitrogen in 316 SS. Typically, 316LN with 0.08 wt. % nitrogen is the major structural material for Prototype Fast Breeder Reactor (PFBR) at Kalpakkam. A brief review of literature shows that an increase in nitrogen content helps in improving the room temperature strength by interstitial strengthening [5], improves creep strength

[6], ductility and corrosion resistance [8] of the steel. Therefore, development of high nitrogen grade 316LN SS has drawn both industrial as well as academic attention.

The concept of atoms occupying interstitial sites in a crystalline lattice frequently arises in metallurgy, and is perhaps surpassed only by the concept of dislocations. First reported in 1926 [15, 16], interstitial atoms are now central to diverse disciplines within materials science. This can be attributed to the disproportionate impact that a small volume fraction of interstitials can have on material behavior; be it steel strengthened by interstitial carbon [17], strain ageing phenomena promoted by interstitial solutes [18], or irradiation-induced defects [19]. The phenomena of interstitial-dislocation interaction and interstitial-grain boundary interaction necessitate meso-scale and macro-scale investigations. This is best exemplified by the beneficial effects resulting from addition of nitrogen to austenitic stainless steels. Prominent is the high degree of solid solution strengthening due to nitrogen [20]. This cannot be explained on the basis of conventional interstitial-dislocation interactions, since N atoms in octahedral sites of FCC should cause symmetric distortions, and thus, should not be able to bind screw dislocations in the manner C does in the BCC matrix of carbon steel [5]. Instead, it is found that asymmetric distortions occur due to the formation of Fe-N complexes [5]. This phenomenon of complex formation is due to the unique electronic configuration of N, a feature that also results in short range ordering [21], secondary strengthening of N-containing austenitic steel [5] and affects the stacking fault energy (SFE). At elevated temperatures, N-containing austenitic steels have a good combination of strength, ductility and toughness. These are attributed to the influence of N on SFE as well as grain boundary strengthening [5, 22]. However, the low solubility of nitrogen in austenitic leads to difficulty in production. Fig. 2.1 shows a schematic effect of major alloying elements used for high nitrogen steel [23].

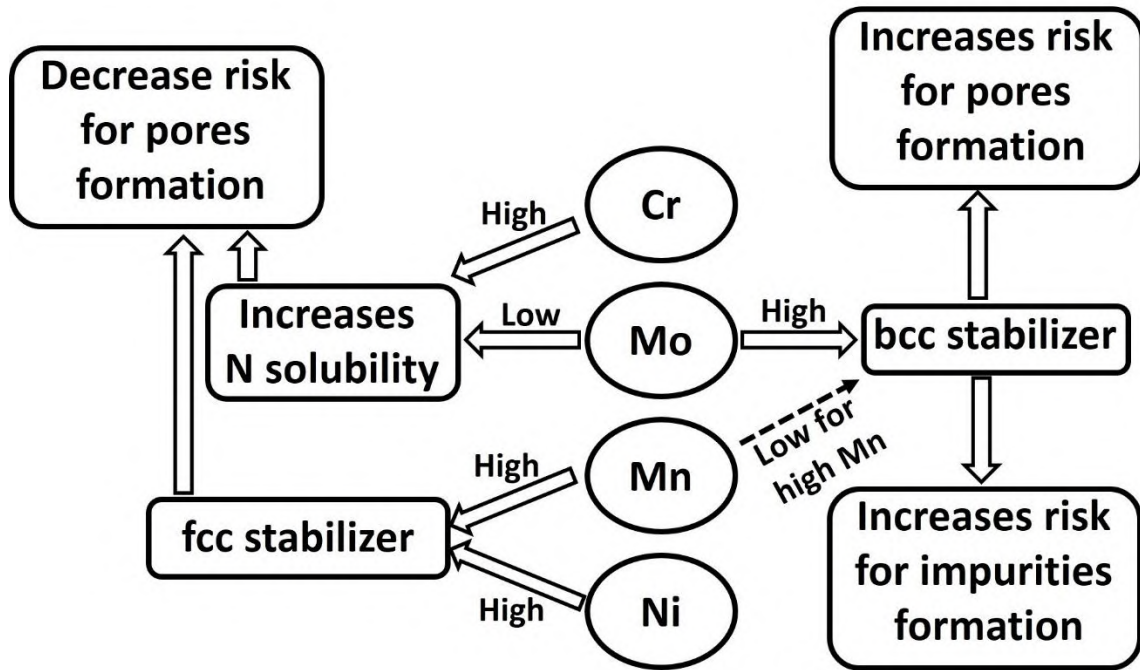


Figure 2.1: Schematic effect of main alloying elements used for high nitrogen austenitic stainless steels on austenite stability, pore formations and nitrogen solubility [23].

Nitrogen enhanced steel can be manufactured in open air (electric arc and induction furnace, electro slag remelting) by adding Nitride ferrochrome agent [24, 25]. The other route is by purging of nitrogen gas under pressure in pressurized induction furnace, pressure electroslag remelting (PSER) [5]. Apart from these powder metallurgy and surface treatment route are also possible [25]. IGCAR has chosen four variants of nitrogen enhanced steel with 0.07, 0.11, 0.14 and 0.22 wt. % of N, in order to understand the effect of nitrogen on various properties important for reactor application. The properties of these steels are still under investigation. It is reported that the tensile properties improved with addition of nitrogen [26]. The increase in nitrogen content increases the resistance against creep cavitation's and hence improves creep rupture life [27]. However, the maximum fatigue life was observed at 0.14wt. % of N [7]. It is also reported that increasing nitrogen promote strong slip localization [7]. Increased nitrogen content signifies increased passive film stability leading to better corrosion resistance [28]. Based on the studies carried out at IGCAR, 316LN SS with 0.11-0.14w% nitrogen

showed the optimum properties [3]. However, all these variant of steel before going into application has to undergo the various forming operations. The present works aims to fulfill the gap area by explaining the role of nitrogen contain in controlling the mechanisms responsible for defining properties of 316LN SS during thermo-mechanical processing.

2.2. Effect of nitrogen content on high temperature flow behavior and constitutive analysis

Flow behavior is one of the most captivating aspects of a material which is as unique as the material composition. The uniqueness of the behavior grabs the attention of researchers to explore the relationships between parameters that affect the behavior of the material. Though the flow behavior of an alloy depends on many factors such as thermo-mechanical history defects present, defects generated, and state of stress, on a larger scale the flow behavior depends on four major parameters; chemical composition, deformation level (i.e. strain), rate of deformation (strain rate) and the temperature at which the material is deformed. Several studies are available which shows constitutive analysis of 316LN with respect to varying temperature, strain and strain rate [13, 29, 30]. The work carried out by Guo et al. shows that nitrogen content has a strong influence on the flow behavior of 316LN in hot working domain [31]. However, very few reports are available which deals with constitutive modeling of flow behavior taking composition into account.

Constitutive analysis of materials has captured the fascination of material scientists. This fascination has yielded many constitutive models over the years [32]. A current review of literature indicates that even today, the subject is as captivating as it was in the 1980s [33-35]. This may be attributed to the inability of a single model to connote

the influence of all imposed parameters on material response, as well as the difficulty in depicting the flow behavior of different materials using a common model. In this scenario, researchers either modify the existing suitable models or propose new models to portray the behavior of new materials. In many cases, the new model is a modification or extension of an existing theory, as exemplified by Modified Zerilli-Armstrong (MZA) [36-39], Modified Johnson-Cook (MJC) [29, 40-43], Mechanical Threshold Stress (MTS) [44-46] etc. models. An alternate approach to predict flow behavior over a very large domain is to combine several models with the help of computer codes as described by Lindgren et al. [47]. This approach has been effective in modelling the flow response of 316L SS over a large range of temperatures and strain rates [47]. However, this complex process may not appeal to the alloy designer who simply wishes to make minor variations in composition and then study the change in flow behavior. Such necessities frequently arise during optimization of element content in an alloy during its development stage. In these situations, users may prefer mathematical or phenomenological models which are less complex and do not require a high level of programming skill. The most widely used phenomenological type constitutive equation is the Arrhenius type equation proposed by Sellars and McTegart [48], which describes the flow behavior by using the sine hyperbolic function. The equation has three basic forms; power law form used for low stress regime, exponential form used for high stress regime, and hyperbolic form for the entire regime [49, 50]. However, the equation in its original form can be used for flow prediction only at a constant strain condition. To predict the flow behavior with varying strain, the equation has been subsequently modified with strain compensation terms [31, 51-53]. This Strain Compensated Arrhenius (SCA) type equation has been successfully used for several materials to predict the flow behavior over a wide range of temperature and strain rate [30, 54-58]. One of the recent modifications to the original Johnson-Cook

(JC) model by Lin et al. [40, 42] is the Modified Johnson-Cook (MJC) which includes the effect of yield stress, strain hardening phenomenon, coupled effects of temperature and strain rate [29, 40-43]. The other model, which considers the effects of strain hardening, strain rate hardening and thermal softening along with the coupled effect of temperature and strain and of temperature and strain rate is the Modified Zerilli–Armstrong (MZA) [36-39]. This model has been developed for predicting the flow behavior of reactor grade austenitic stainless steels and has also been successfully employed for other materials [59]. This model has recently been improved and proposed as Model D8A [60] to predict the flow behavior of steels in the regime where the materials show flow saturation followed by strain hardening. Amongst these, the MJC and D8A models were specifically developed to depict the flow behavior of special grade steels [40, 60]. However, this composition-dependent facet of constitutive modelling is less explored and often gets neglected in popular discourse. The other type, namely the computational model, takes experimental data as input and uses algorithms of varying sophistication to identify trends and patterns between data points. These trends are used to predict flow behavior at the same or at different conditions, as is often done using ANN techniques [61, 62]. Hitherto, ANN has often been recommended for such uses as it readily accommodates the composition in its input parameters [63-65]. A review of literature over the past 5 years reveals that both types of model continue to be in active use. Nearly 500 studies on SCA based flow prediction alone have been published in the past 5 years, as collated by scientific databases such as Web of Science and Science Direct. The equivalent number for ANN-based flow prediction is approximately 160, with a rapid increase in the past 2 years.

It is also a fact that every constitutive model reported in the literature, is suitable for one or the other material. Therefore, from the perspective of alloy development, the

most suitable model can be chosen only by a critical comparison of different models using the same data base and common selection criteria.

2.3. Effect of nitrogen content on microstructural evolution

In hot working domain, DRV and DRX are the two major phenomena that control microstructure evolution during thermo-mechanical processing of the alloy. Consequently, DRV and DRX have constantly engaged the attention of material scientists and engineers. DRV involves annihilation of dislocation, whereas the DRX is the formation of new strain free grain. Both the phenomena are strongly influenced by chemical composition of the alloy.

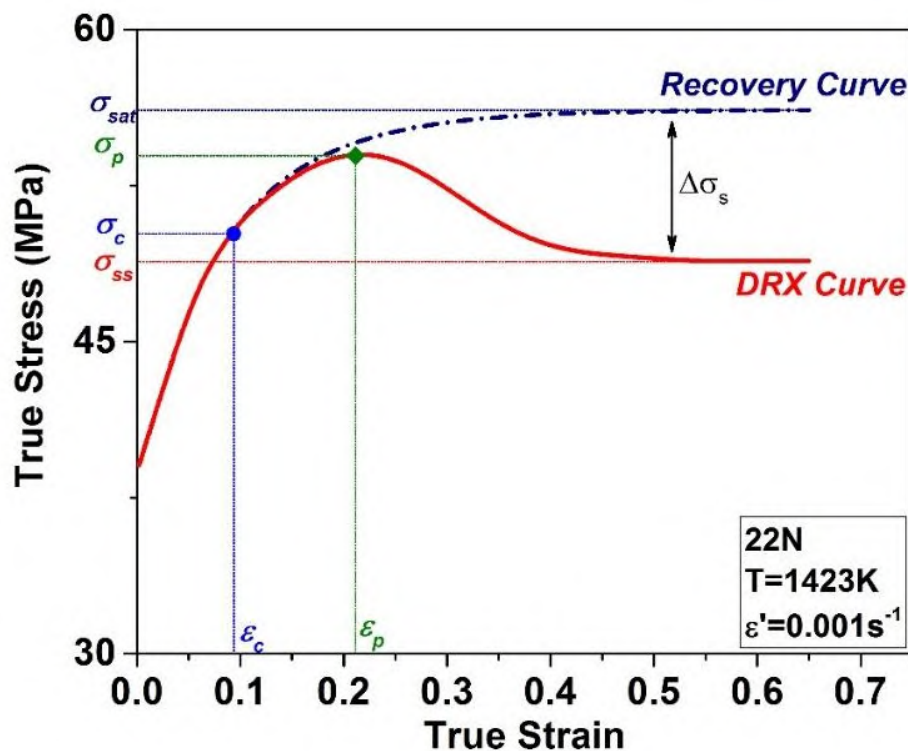


Figure 2.2: A typical flow curves showing the DRV curve and DRX curve with respect to stress and strain.

Avrami analysis of flow curves is a standard method to illustrate the kinetics of DRX [66-69] and is widely used for studying nucleation and growth of static recrystallization. Jonas et al. [68] extended the method to analyze dynamic recrystallization process. In this

method, it is assumed that the experimental flow curve can be hypothetically divided into DRV and DRX curves, at a given strain rate and temperature as illustrated in Fig. 2.2.

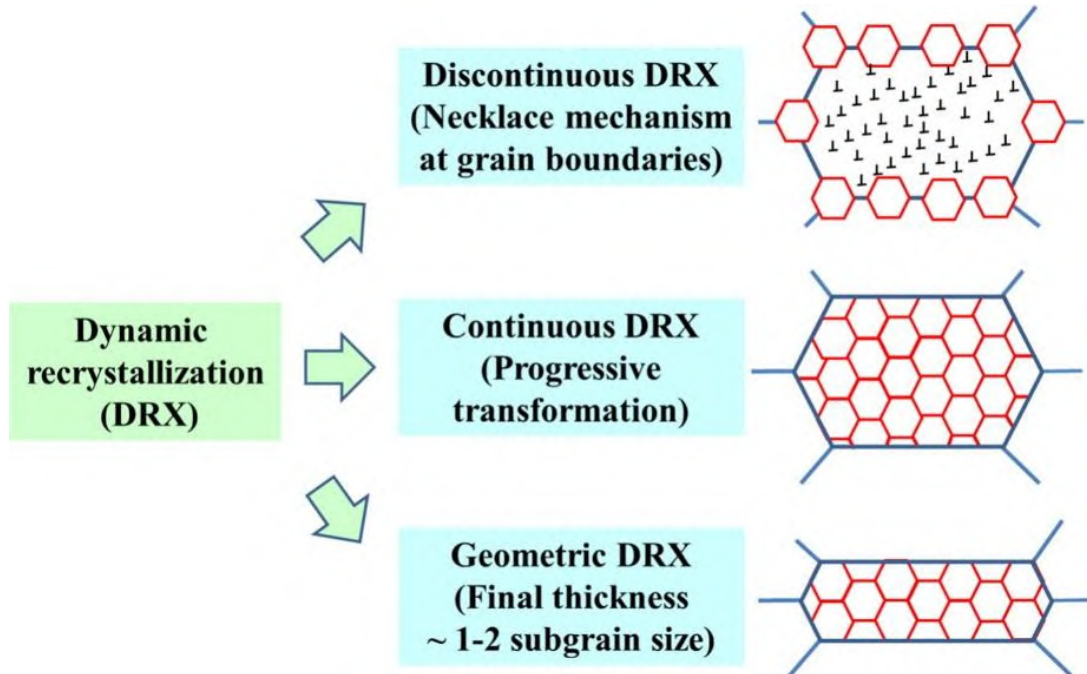


Figure 2.3: Flow chart showing various types of DRX [71].

The point corresponding to critical stress (σ_c) and critical strain (ϵ_c) is the point where the DRX initiates and is also the point from where the deviation between DRX curve and DRV curve begins [68]. Beyond the critical point, further straining causes increase in flow stress in both DRX and DRV curves. The stress corresponding to the peak point of the DRX curve is called peak stress (σ_p). In case of DRV curve, however, no distinct peak point is achieved; on deformation the stress gradually reaches a saturation values (σ_{sat}), where the rates of dislocation annihilation and generation are balanced. In DRX curve, beyond the peak point, the flow softening dominates and reaches a steady state stress (σ_{ss}). Defining a clear domain for DRV and DRX without overlapping of domains has remained always challenging, especially in steels. DRV is often followed by DRX; the transition depends on external parameters viz. deformation temperature, deformation rate

and strain as well as on the intrinsic parameters such as stacking fault energy (SFE) and dislocation density. Fig.2.3. shows the various type of DRX. In Continuous DRX (CDRX), homogenous microstructure develops throughout material, without recognizable nucleation and growth [70]. Discontinuous DRX (DDRX) is a heterogeneous nucleation of DRX mainly at grain boundaries, forming necklace type structures. High SFE materials are known to undergo CDRX, while materials with low SFE show discontinuous DRX (DDRX). The other type of DRX is Geometric DRX (GDRX) which occurred due to change in grain geometry during deformation [71]. Since addition of alloying elements results in change in SFE, it is expected that, DRX behavior will also change with variation in alloying element.

Effect of Cr and Mo addition on DRX behavior of C-Mn-V steel was investigated by Martins et al. [72]. Their study shows Cr and Mo suppress the DRX in steel and which is manifested as higher DRV-DRX transition temperature. To know the effect of addition of C on DRX behavior several studies have been carried out. The investigation carried out by Wei et al. [73] shows that C reduces the critical strain needed for the DRX initiation and also accelerates rate of DRX in steel. A study by Beladi and Hodgson [74] shows that influence of C on softening behavior of steel may vary depending upon the deformation temperature chosen. Effect of boron addition has been studied by Mejia et al. [75] and L'opez-Chipres [76]. These studies indicate that the addition of boron favors dynamic recrystallization by decreasing the critical strain. In contrast, the study by Kim et al. [77] reports that boron strongly retards dynamic recrystallization while phosphorous does not have any influence on DRX behavior of steel.

From the above studies, it can be summarized that every element can have a unique effect on DRX behavior of steel and the effect may vary with deformation condition. Nitrogen, which is an important element in many steels specially developed for

strategic application, can be expected to have a significant effect on DRX behavior of these steels. The effect of N on flow behavior of steel has been studied by many researchers [30, 78, 79]. It has also been seen that addition of N has significant impact on high temperature flow behavior, and dynamic recrystallization (DRX) of steels [80]. The SFE is often cited as a key parameter in influencing DRX characteristics [71, 81]. Thus, an explicit correlation is expected to exist between the addition of N, variation in SFE and evolution of DRX. In many metals, effects of interstitial elements on SFE and effect of interstitial elements on DRX have been separately investigated [82].

Though these studies outline the gross influence of N on hardening and softening behavior, however, do not exclusively deal with the influence of Nitrogen on SFE- DRX linkage behavior. To understand the influence of nitrogen content on microstructural evolution, it is utmost important to understand the influence of nitrogen on DRX behavior.

2.4. Influence of nitrogen content on workability of material

Since, the mechanical response of an alloy and DRX behavior is affected by the varying chemical composition, the intrinsic workability of the alloy is also expected to change with the change in constituent fraction. Besides the chemical composition, thermomechanical treatments, grain size, and the processing parameters like strain, strain rate and temperature affects the intrinsic workability of material.

There are several thermo-mechanical processes such as forging, rolling and extrusion etc. which are employed for shaping the material. Using many alternative thermo-mechanical methods, a product can be obtained. However, the operating parameters for all the thermo-mechanical processes need not be same as the equipment employed for these methods operate on different working principle and have different

working speeds. The typical strain rate range of various manufacturing processes are shown in Table.2.1. The knowledge of workability of an alloy over a wider domain of strain and strain is important, not only to choose suitable process to shape the material but also to identify optimal processing parameters for the chosen process.

Table.2.1: Typical ranges of strain rates of various manufacturing process [83, 84].

Process	Strain rate (s⁻¹)
Superplastic Forming	$10^{-5} - 10^{-2}$
Forging	$10^{-1} - 10$
Rolling	$10^{-1} - 10$
Extrusion	$10^{-1} - 1$
Sheet metal forming	$10^{-1} - 10$
Explosive forming	$10^2 - 10^6$

Dynamic Materials Model (DMM) is the most used technique to characterize workability of the material. The workability map developed on the basis of DMM technique is known as processing map. The map is developed by superimposing the efficiency map and the instability map. The processing map indicates safe and unsafe domains for thermo-mechanical processing in strain rate -temperature space. The safe or stable domains usually show homogenous deformation and desirable microstructure, whereas the unsafe or unstable domains are characterized by undesirable flow behavior such as negative strain rate sensitivity, thermal insensitivity and microstructural defects such as micro-cracks, shear bands and wedge cracking etc., in materials.

A review of literature shows that the 316 SS has an optimum working domain at 1323-1373K at $0.02-2s^{-1}$ [85]. On lowering of carbon in austenitic stainless steel, the processing domain was found to be increased and recommended domain is 1373-1523K at $0.001-10s^{-1}$ [86]. In case of 316LN, few literatures have reported the optimum

processing domain with varying alloying element and nitrogen content. Guo et al. reported that 1423K at 0.001s^{-1} is optimum domain for steels, however it was reported for range of nitrogen (0.12-0.22 wt. % N) content not a specific grade nitrogen steel [31]. For 316LN with 0.14wt. % N the optimum domain is reported to be 1423K at 0.01s^{-1} [13] and with 0.16 wt.% N it is found to be 1373K at 0.001s^{-1} [85] in literatures. Based on the above literatures, various processing domains are recommended for specific composition of 316LN. It also shows that addition of interstitial element like nitrogen can affects in shifting of the safe processing domain.

The actual effect of nitrogen addition in 316LN on processing domain are not yet fully explored and understood. Therefore there is a need for identifying the processing domain for various variant of nitrogen grade steel and recommend the best processing parameters for bulk production.

2.5. Metallurgical instabilities during processing at high strain rates

The unsafe domain of the processing map is most frequently characterized with microstructural defects such as deformation bands and adiabatic shear bands (ASB). Adiabatic shear bands can be defined as a region of flow localization where the material flow intensity is higher than that of its surroundings. In hot isothermal forging, it is a region in form of band that separates the dead metal zone and the deformed zone [87]. ASBs can occur due to many factors such as difference between the work piece and die temperature, due to complex geometry, material properties, lubrication and speed during forming operations [88, 89]. These bands are generally observed at high strain rate loading conditions, especially at strain rate above 10s^{-1} . Once the shear band is commenced, it may become locally self-propagating with the aid of thermal accumulation [90], resulting in the reduction of flow stress. Problems arising from this have been

reported in both hot working and cold working of steels [90-92], titanium alloys [89, 93-96], aluminum alloys [97] and tantalum [98].

To understand the formation ASB, several testing techniques have been employed in laboratories [99]. Hopkinson testing [92] and explosive forming [98] are techniques which are mostly used to impart very high strain rate (greater than 1000s^{-1}) during deformation. The formation of shear bands are dependent on material properties such as strain hardening, strain rate sensitivity, thermal conductivity, specific heat and phase transformation kinetics [90, 98]. ASB can be divided into two types, namely deformation bands and transformation bands [100]. In deformation bands, the microstructure observed is highly deformed which leads to localized signature of recovery and recrystallization [101]. Where as in transformation bands, the heavy deformation leads to phase transformation such as martensitic transformation, formation of nano-sized grains [102], amorphisation [103] and glassy phase formation [104]. Venugopal et al. have reported at temperature $< 1123\text{K}$ and strain rates $>10\text{s}^{-1}$, the 316L SS is prone to flow localization and that leads to formation of ASB. 316LN SS is also prone to such instabilities [85, 105] at high strain rates. However, very few studies are available which deals with the effect of nitrogen content on the probability of formation, strain that is required for initiation and intensity of the adiabatic shear bands.

2.6. Scope of the present study

Based on the above literature review, it noted that there is requirement of deformation studies on effect of nitrogen on 316LN austenitic stainless steel at elevated temperature. However, till now not enough work has been carried out on the effect of varying nitrogen in 316LN. Therefore the following loopholes are identified as scope of the present thesis work.

- To develop a composition-dependent facet of constitutive modelling to predict the flow behavior of nitrogen enhanced 316LN SS.
- To explicate the influence of N on DRX nucleation, grain growth, SFE and the linkage between them.
- By employing DMM, to construct the processing maps which can be used to determine the safe processing zone for different nitrogen grade steel.
- To understand the underlying mechanism for evolution of adiabatic shear banding at high strain rates.

Chapter 3

Experimental Details

3.0. Preamble

In this chapter, the details of material used, experimental procedure and characterization techniques adopted to carry out the current project work are discussed in detail.

3.1. Material

The base material used in the present study is the 316LN austenitic stainless steel. Four variants of 316LN SS with varying nitrogen content have been chosen for this study. The chemical composition of the variants is given in Table 3.1. In the thesis, the variants with 0.07 wt. %, 0.11wt. %, 0.14 wt. % and 0.22 wt. % nitrogen are referred to as 7N, 11N, 14N and 22N, respectively. For the thesis work, extensive experiments are carried out using 7N, 11N and 22N variants. However, only few experiments are carried out using specimens of 14N variant at selected conditions.

Table 3.1: Chemical composition of 316LN (wt. %).

Heat No.	Designation	Cr	Mo	Ni	Mn	Si	C	N	S	P	Fe
H8344	7N	17.53	2.49	12.2	1.7	0.22	0.027	0.07	0.005	0.013	Bal
H8335	11N	17.62	2.51	12.27	1.78	0.21	0.033	0.11	0.005	0.015	Bal
H8334	14N	17.57	2.53	12.15	1.74	0.20	0.025	0.14	0.004	0.017	Bal
H8345	22N	17.57	2.54	12.36	1.70	0.20	0.028	0.22	0.005	0.018	Bal

These alloy steels were produced by double melting process. Nitride ferrochrome agent was added to attain the required amount of nitrogen in different steels. These steel

were received in rolled plates in mill annealed conditions. In order to ensure similar grain size in 7N, 11N and 22N steels, cylindrical bars machined from the plates were subjected to a common solution annealing treatment at 1373K for 30 min followed by water quenching. However, neither the bars machined from the 14N plate nor the specimens fabricated thereof were subjected to any heat treatment. This was done consciously to study the effect of grain size on the prediction capability of constitutive models discussed in Chapter 4, which is considered relevant as some degree of grain size variation across different heats is unavoidable during practical alloy development.

3.2. Hot Isothermal Compression Test

Cylindrical specimens of 15 mm height and 10 mm diameter were machined from the solution annealed bars for compression testing. Concentric grooves of 0.5 mm depth were made on the top and bottom faces of these cylindrical specimens to facilitate the retention of lubricant during testing. Chamfer of 1 mm - 45° was provided on the edges of the top and bottom faces to avoid fold over of the material in the initial stages of compression. To measure the core temperature of specimen, a small hole of 0.8 mm diameter and 5 mm depth was drilled at mid height of specimen to insert the thermocouple. To study the effect of deformation geometry (Chapter 7), specimens with square cross-section at base (9 mm side length) and rectangular cross-section at base (10 mm x 8 mm) were fabricated. The height (15 mm) and specimen volume have been maintained constant for all three geometries. A servo-hydraulic, constant true strain rate compression testing machine of 100 kN capacity with special quenching facility was used for the hot isothermal compression testing of the 7N, 11N and 22N specimens as shown in Fig. 3.1.

Uni-axial compression tests were performed in the temperature range of 1123K to 1473K (at 50K interval) and at constant true strain rates of 0.001, 0.01, 0.1, 1 and 10 s⁻¹. Each specimen was deformed to a nominal strain of 50%. However, the 14N grade was tested using a Gleeble thermo-mechanical simulator in temperature domain 1123-1423K at a strain rate of 0.1s⁻¹. All the tests were carried out in accordance with the ASTM E209 standard.

The test matrix used for the compression test are listed in Table 3.2. Before imparting the deformation, each specimen was heated at a rate of 5Ks⁻¹ to the desired deformation temperature, and soaked at that temperature for 2min to achieve homogeneous temperature distribution throughout the specimen. The temperature during soaking and the adiabatic temperature rise during deformation were measured with the help of a K-type thermocouple inserted into the center of each specimen. To minimize the friction during deformation, graphite foils and Ni paste were used between specimens and the platens. As a result, no significant barreling of the specimen was observed after deformation. The typical appearance of the samples before and after testing are shown in Fig. 3.2. Each specimen was water-quenched at the end of deformation. The load-stroke data recorded during the deformation process were used to generate true stress-true plastic strain curves following the customary procedure [106].

Table 3.2: Test conditions used for hot compression test in the present study.

Alloy	Temperature (K)	Strain Rate (s ⁻¹)	Additional tests	
7N	1123, 1173, 1223, 1273, 1323, 1373, 1423, 1473	0.001, 0.01, 0.1, 1, 10	873K, 10s ⁻¹	1123K, 10s ⁻¹
				<ul style="list-style-type: none"> • Square Base Specimen • Rectangular Base Specimen
11N				-
22N		-		
14N		0.1		-

The flow curves were corrected using the method suggested by Goetz et al. [107], incorporating the adiabatic temperature rise measured during high strain rates, mostly at $1s^{-1}$ and $10s^{-1}$. A schematic illustration of the experimental procedure is shown in Fig.3.2. The deformed specimens were subsequently used for microstructural investigation.

3.3. Microstructural Characterization

To examine the deformed microstructure, the specimens were cut parallel to loading axis using Struers Secotom 10 table top precision cut off machine. The cut specimens were metallographically polished upto 0.25 micron using standard procedure.

3.3.1. Optical and Confocal Microscopy

The polished sample were electrochemically etched by using oxalic acid and demineralized water in ratio of 1:9 for 5 minutes at 0.2 V potential voltage difference. The microstructures of these samples were examined optically in maximum deformed zone by using Olympus GX51 microscope. Linear intercept method were used to measure the grain size of the specimen. Some of these specimens were inspected in Olympus LEXT OLS4000 Laser Scanning Confocal Microscope for better analysis of the deformed zone.

3.3.2. Electron Backscattered Diffraction

The other half of the deformed sample were used for Electron Back Scatter Diffraction (EBSD) investigation. The samples were electro-polished by using Struers Lectropol 5 at 20 volts with 10% perchloric acid and 90% methanol as etchant. EBSD scans were conducted in the central part of the specimen over an area of $400\ \mu\text{m} \times 400\ \mu\text{m}$ by using an automated EBSD facility (Oxford Instruments).

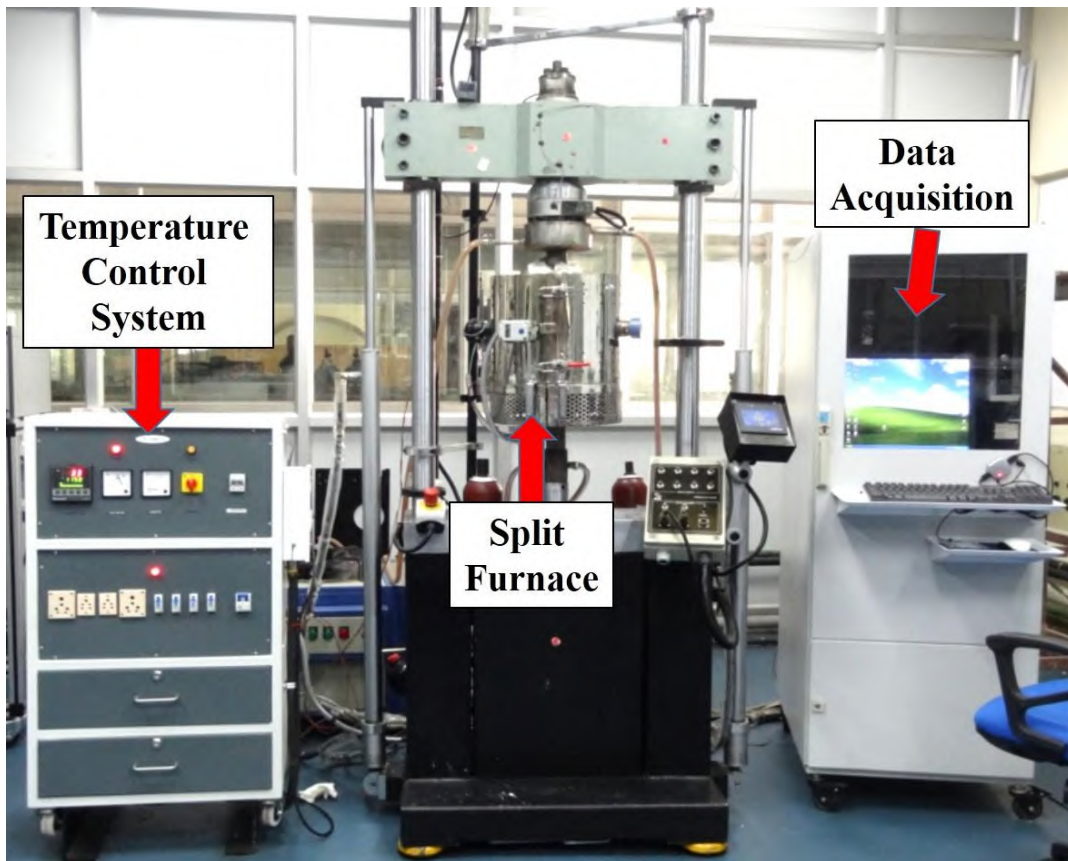


Figure 3.1: High temperature constant true strain rate compression testing machine.

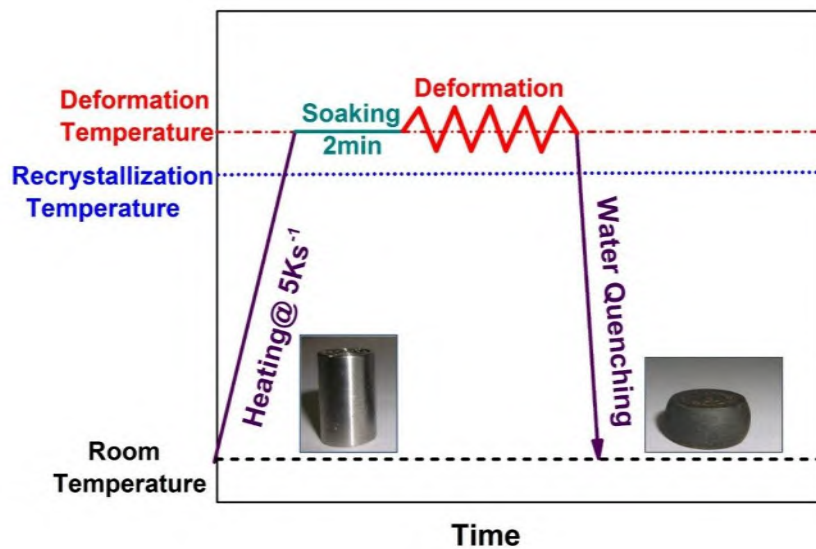


Figure 3.2: Schematic illustration of the experimental procedure. Typical appearance of sample before and after deformation.

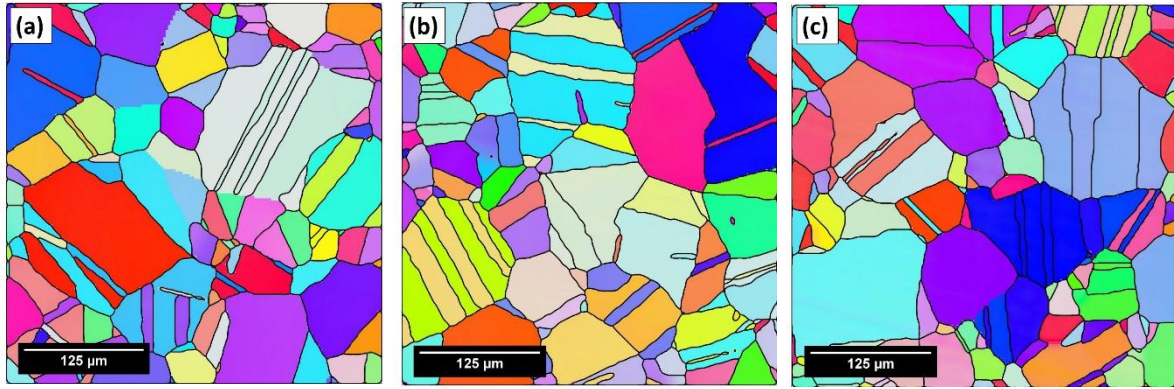
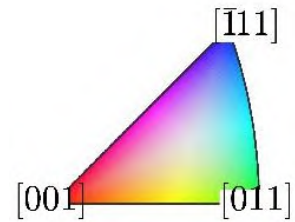


Figure 3.3: Inverse pole figure (IPF) maps of (a) 7N, (b) 11N and (c) 22N variants in solution-annealed condition.



EBSD maps were acquired with step size of $0.5\ \mu\text{m}$ - $1.5\ \mu\text{m}$ depending on the specific requirement using square grid. The processing of the EBSD data were carried out using the open source software MTEX 4.5 developed by Bachmann, Hielscher and Schaeben [108]. The Grain Orientation Spread (GOS) and intragranular misorientation are calculated with the aid of MTEX. The GOS is the average deviation in orientation between each point in a grain and the average orientation of the grain [108]. The intragranular misorientation is misorientation of each pixel with grain average orientation [108]. The inverse pole figure (IPF) maps of 7N, 11N and 22N variants in solution annealed condition are shown in Fig.3.3. These figures indicate that the solution annealed materials consists of equiaxed grains with large fraction of twin boundaries. The average grain sizes after solution treatment are found to be $57\ \mu\text{m}$, $61\ \mu\text{m}$ and $58\ \mu\text{m}$ for 7N, 11N and 22N, respectively.

3.3.3. Transmission electron Microscopy

Transmission Electron Microscopy (TEM) was carried out for selected specimens to observe the dislocation structures and stacking fault. The specimens were mechanically ground and polished to achieve 100 μm thickness using standard metallographic procedure. Thin foil of 3 mm diameter discs were punched out from the polished specimens. Perforation were carried out by Struers Tenupol 5 double jet thinning in 10% perchloric acid and 90% methanol solution. The TEM examination were carried out with Libra 200FE (Carl Zeiss) high resolution TEM operated at 200KV. Bright field imaging were carried out.

3.3.4. X-Ray diffraction

X-Ray Diffraction (XRD) technique was used to estimate the lattice parameter, dislocation density and stacking fault probability at selected conditions using Scintag X ray diffractometer. For this purpose, Rietveld refinement [109] was implemented through the program MAUD [110]. Instrumental broadening was subtracted prior to refinement. Size-strain anisotropy and planar defects were accounted for using models given by Popa[111] and Warren [112], respectively.

Chapter 4

Flow behavior analysis of 316LN stainless steel at elevated temperature

4.0. Preamble

This chapter presents the constitutive analysis of 7N, 11N and 22N variants of 316LN SS. The first part deals with the effect of nitrogen content on work hardening, strain rate sensitivity and temperature sensitivity, while the second part deals with the development of thermo-viscoplastic constitutive equation that takes variation of nitrogen content, temperature, strain and strain rate into account.

4.1. Deformation behavior of different variants of 316LN SS

The flow curves of 7N, 11N and 22N variants of 316LN SS are shown in Figs. 4.1, 4.2 and 4.3, respectively. Each curve shown in these figures is unique. Despite the uniqueness, there are some common features observed in flow curves of all three variants. These common features are response to increasing strain, deformation temperature, and deformation strain rate.

With increase in strain, the flow stress of each variant increases up to a certain strain level, this is known as work hardening. After reaching a peak, the stress either remains constant or reduces on further straining; it depends on the temperature of deformation. Work hardening is attributed to hindrances to dislocations motion by the activation of multiple slip systems, formation of forest dislocations, increase in defect density [5, 113]. With increase in deformation temperature, the flow stress of each variant decreases, when deformed to a specific strain with a fixed strain rate. This characteristic is known as thermal softening of the material. Besides, the temperature has a significant

effect on the work hardening which varies with strain level. Such behavior signifies the coupled effect of temperature and strain on the resistance of the material to deformation.

With increase in strain rate, the variation of flow stress at a constant deformation temperature and at a specific strain level, is known as strain rate sensitivity. It is positive at deformation temperature above 1323K, 1323K and 1373K for 7N, 11N and 22N variants, respectively. At deformation temperatures below 1323K, the strain rate sensitivity is positive for all variants when deformed with $0.001-1s^{-1}$ upto 0.65 strain. However, the materials tend to show negative strain rate sensitivity when deformed in the domain $1-10 s^{-1}$ at higher strain level i.e. greater than 0.45, 0.45 and 0.25 for 7N, 11N and 22N variants, respectively. During deformation at high strain rates, the heat is entrapped in the material leading to adiabatic temperature rise. This rise in temperature is the potential cause for the negative strain rate sensitivity and flow instability behavior. An extensive study on the effect of adiabatic temperature rise is discussed in section 7.1. This analysis indicates an indisputable coupled effect of temperature - strain rate on flow behavior of all the variants of the steel studied here. The combined influence of strain rate and temperature on flow stress is demonstrated in Fig. 4.4 at 0.6 strain.

Even with the afore-mentioned global similarities, the uniqueness of flow curve obtained at a fixed deformation condition arises from the compositional variation i.e. the difference in nitrogen content. The nitrogen content decides the magnitude of the response of the material to strain, strain rate and temperature. The effect of nitrogen on the flow curves can be noticed in Fig. 4.5. This figure shows that nitrogen enrichment enhances the resistance to deformation. The effect of nitrogen on work hardening of the material, is in good agreement with the observations by other researchers [5, 26, 79, 114], who, however, used different deformation modes and conditions. While nitrogen content

enhances the strain hardening in the steel till the peak stress, no prominent effect on strain softening could be discerned beyond this point in the present study.

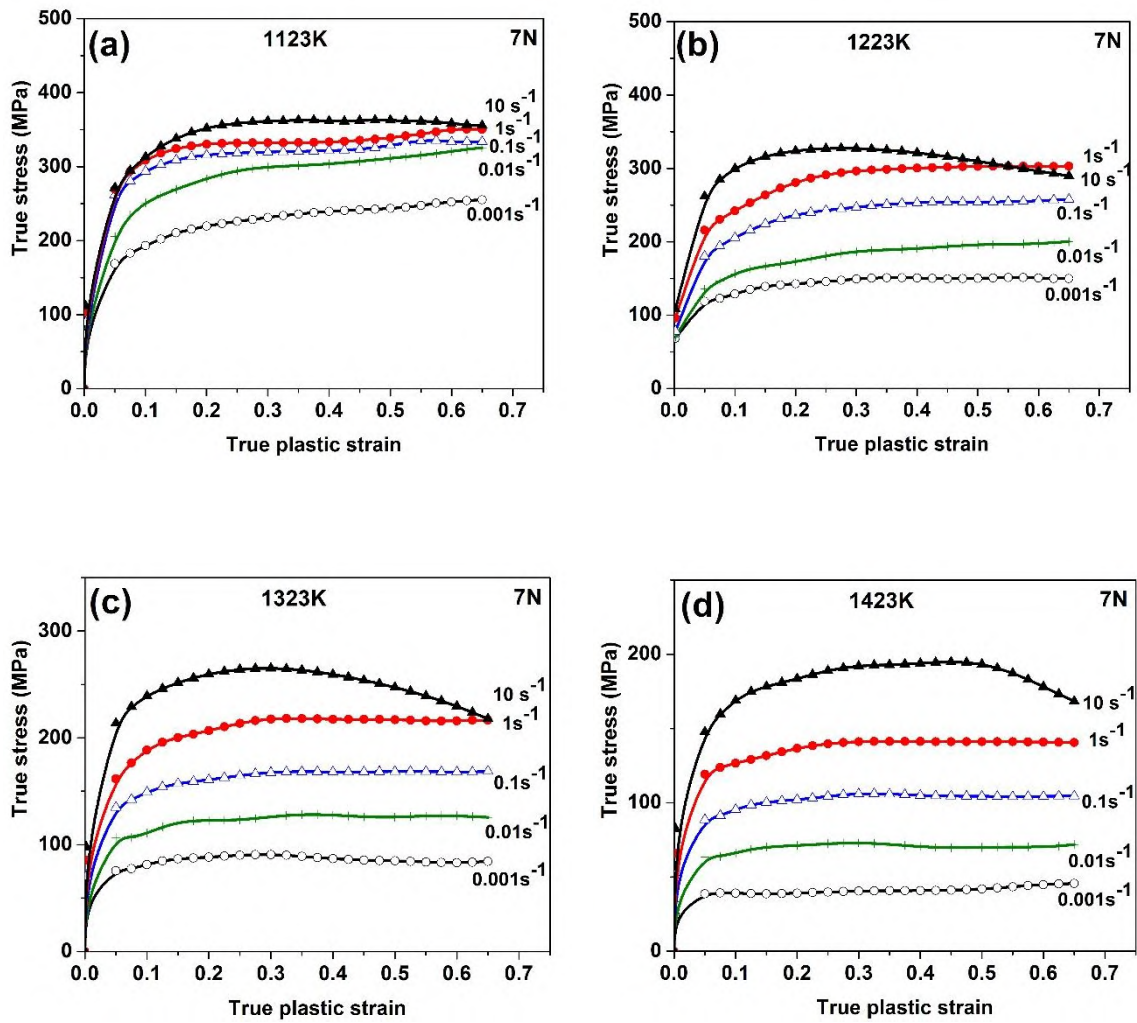


Figure 4.1: True stress – strain curves of 7N at (a) 1123K, (b) 1223K, (c) 1323K and (d) 1423K at different strain rates.

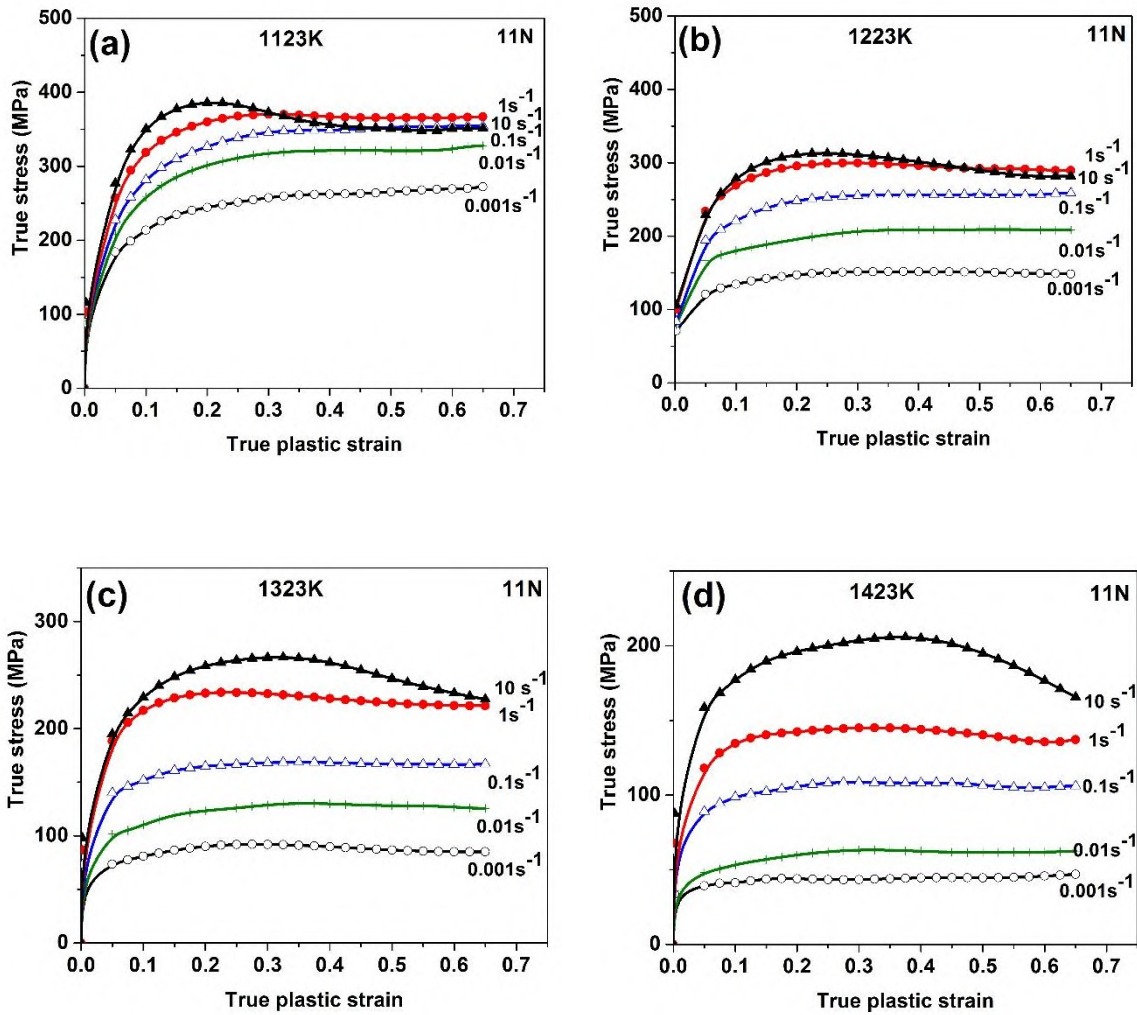


Figure 4.2: True stress – strain curves of 11N at (a) 1123K, (b) 1223K, (c) 1323K and (d) 1423K at different strain rates.

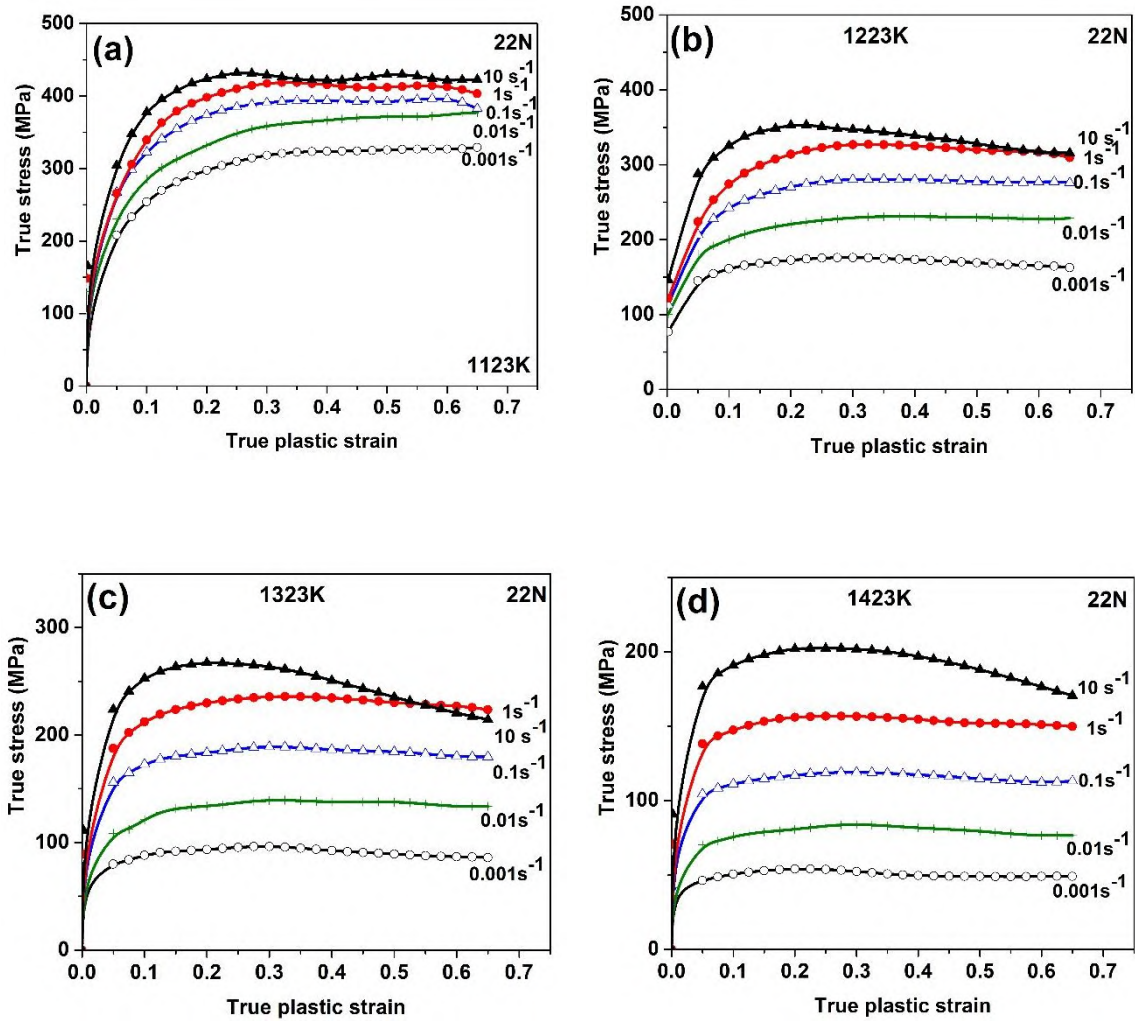


Figure 4.3: True stress – strain curves of 22N at (a) 1123K, (b) 1223K, (c) 1323K and (d) 1423K at different strain rates.

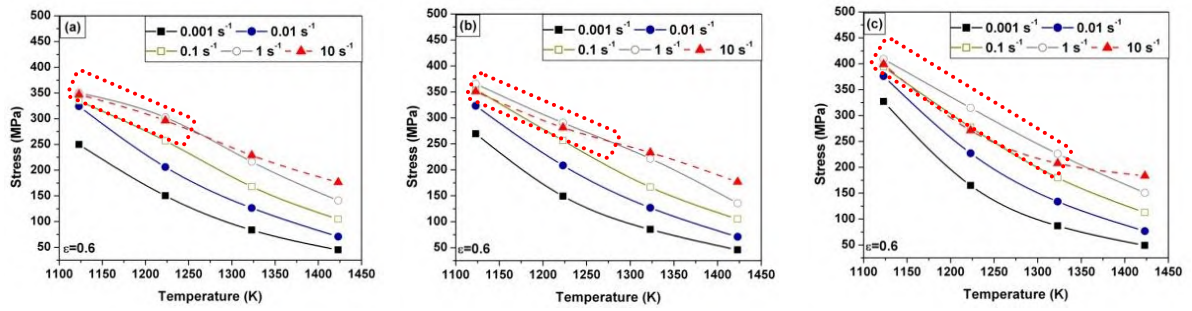


Figure 4.4: Variation of flow stress with temperature at a)7N, b)11N, c)22N at 0.6 strain. Marked regions represent the instability zone.

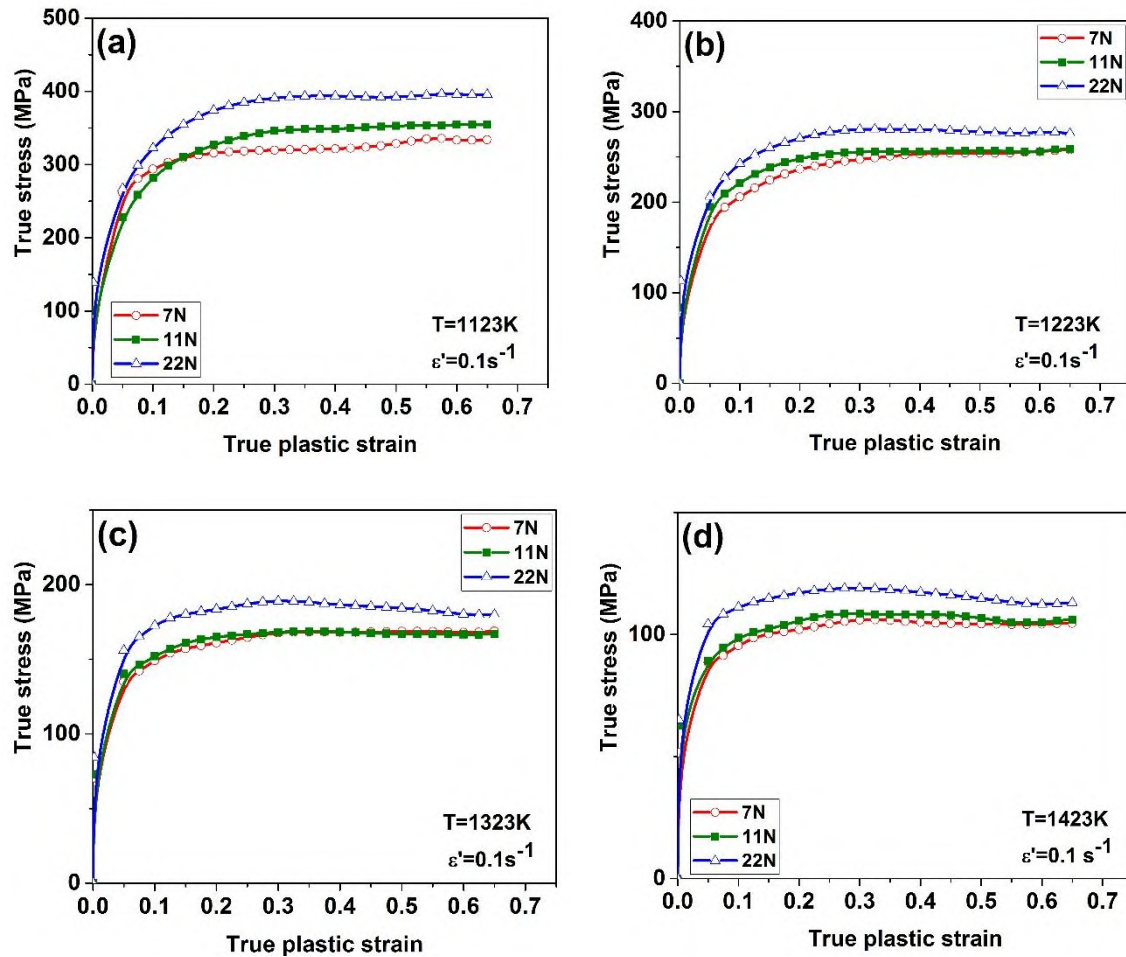


Figure 4.5: True stress – strain curves of 0.1s^{-1} at (a) 1123K, (b) 1223K, (c) 1323K and (d) 1423K .

The effect of temperature on strain rate sensitivity has already been discussed in the previous paragraphs. Besides the temperature, strain has also effect on strain rate sensitivity. It can be seen from the Fig.4.1-4.3, that at deformation temperature below 1323K and at strain rate $1s^{-1}$ to $10s^{-1}$, the strain rate sensitivity remains grossly positive at low strain levels. However, this behavior begins to reverse at higher strain levels, for example at true strain of 0.65. The strain and temperature where the transition from positive to negative strain rate sensitivity occurs depends on composition. The ‘negative strain rate sensitivity’ is often cited as a signature of flow instability. Evidence of flow instability of 316LN SS has been reported numerous times in the literature [115-117]. It is believed that the addition of nitrogen leads to increase in pinning of dislocation and multiplication of dislocation[113]. These clusters of dislocations lead to flow localization. Adiabatic temperature rise causes these localized regions combine to form shear bands and contribute to negative strain rate sensitivity [118].

4.2. Constitutive modeling

The flow behavior of the tested materials, as shown in Figs. 4.1-4.5, shows common characteristics such as thermal softening, strain hardening/softening, strain rate hardening/softening and compositional strengthening. This similarity provides a scope to describe the flow behavior of all the variants through a single model. If integrated with the chemical composition, the model can be helpful to produce the flow behavior of other variants of 316LN SS (having different nitrogen content) different from the variants reported here and thereby reducing number of experiments. In order to predict or reproduce a stress-strain curve, a constitutive model therefore needs to represent the individual effects of all these phenomena, as well as the second-order interactions between them. In this study, three phenomenological models (SCA, MJC, D8A) and a

computational model (ANN) have been chosen to represent the common characteristics of the flow behavior discussed in the section 4.1.

4.2.1. Strain Compensated Arrhenius Model (SCA)

The original form of the Arrhenius-type equation which is used for the flow stress prediction is as follows [48]:

$$\sigma = \frac{1}{\alpha} \left[\sinh^{-1} \left(\frac{\dot{\varepsilon}' \exp(Q/R'T)}{A} \right)^{1/n'} \right] \quad (4.1)$$

The equation represents the combined effects of temperature (T) and strain rate ($\dot{\varepsilon}'$) on the flow stress (σ) at a constant strain. R' is universal gas constant (8.314 J/mol.K). A, α , n' and Q (kJ/mol) are the material constants represented by polynomial functions of strain (ε). The constants n' , α , Q and A, for 7N and 22N grades of the steel, are calculated at strain intervals of 0.05 following the iterative procedure described in [53, 117]. It has been found that the n' and α constants can be reasonably fitted with a 4th order polynomial fit for 7N and 5th order polynomial fit for 22N, whereas the constants Q and $\ln A$ are satisfactorily fitted with a 3rd order polynomial. These functions are listed in Eq.4.2.

$$\begin{aligned} \alpha &= f_1(\varepsilon) = \alpha_0 + \alpha_1\varepsilon + \alpha_2\varepsilon^2 + \alpha_3\varepsilon^3 + \alpha_4\varepsilon^4 + \alpha_5\varepsilon^5 \\ n' &= f_4(\varepsilon) = n_0 + n_1\varepsilon + n_2\varepsilon^2 + n_3\varepsilon^3 + n_4\varepsilon^4 + n_5\varepsilon^5 \\ Q &= f_2(\varepsilon) = Q_0 + Q_1\varepsilon + Q_2\varepsilon^2 + Q_3\varepsilon^3 \\ \ln A &= f_3(\varepsilon) = A_0 + A_1\varepsilon + A_2\varepsilon^2 + A_3\varepsilon^3 \end{aligned} \quad (4.2)$$

The coefficients of these polynomial functions are given in Table 4.1. The flow curves predicted using these coefficients are shown in Fig. 4.6, along with the corresponding experimental flow curves for comparative purposes.

Table 4.1: Coefficient of the polynomial functions shown in Eq.1 for the grades 7N and 22N.

Alloy	α Coefficient	n' Coefficient	Q Coefficient	$\ln A$ Coefficient
7N	$\alpha_0= 0.01134$	$n_0= 6.5758$	$Q_0= 479.594$	$A_0= 34.725$
	$\alpha_1= 0.00774$	$n_1= -24.992$	$Q_1= -88.260$	$A_1= 10.281$
	$\alpha_2= -0.1585$	$n_2= 157.190$	$Q_2=-543.368$	$A_2= -81.412$
	$\alpha_3= 0.4153$	$n_3= -334.524$	$Q_3= 1482.473$	$A_3= 149.679$
	$\alpha_4= -0.3107$	$n_4= 238.891$		
22N	$\alpha_0= -0.000435$	$n_0= 10.018$	$Q_0= 488.767$	$A_0= 33.676$
	$\alpha_1= 0.334$	$n_1= -125.875$	$Q_1= 817.789$	$A_1= 82.177$
	$\alpha_2= -2.391$	$n_2= 865.083$	$Q_2= -878.191$	$A_2= -100.596$
	$\alpha_3= 7.0974$	$n_3= -2497.50$	$Q_3= 836.548$	$A_3= 84.952$
	$\alpha_4= -9.3391$	$n_4= 3232.51$		
	$\alpha_5=4.54502$	$n_5= -1553.185$		

4.2.2. Modified Johnson-Cook Model (MJC)

One of the recent modifications to the original Johnson-Cook (JC) model [33] by Lin et al. [40, 42] yield Eq. 4.3:

$$\sigma = (A_1 + A_2\varepsilon + A_3\varepsilon^2)(1 + A_4 \ln \varepsilon^{i*}) \exp\left[(\lambda_1 + \lambda_2 \ln \varepsilon^{i*})(T - T_r)\right] \quad (4.3)$$

where $A_1, A_2, A_3, A_4, \lambda_1, \lambda_2$ are material constants, $\varepsilon^{i*} = \varepsilon'/\varepsilon'_0$ is a dimensionless parameter with ε'_0 as the reference strain rate, ε' as the current strain rate, and T_r is the reference temperature. The constants A_1, A_2 and A_3 are obtained by fitting a second order polynomial to the experimental stress-strain data at reference temperature (1123K) and reference strain rate ($1s^{-1}$) [40]. All the calculated material constants of MJC model for the grades of 7N and 22N are given in Table 4.2. The flow curves predicted using these constants are compared with the experimentally obtained flow curves for the grades of 7N and 22N in Fig. 4.7.

Table 4.2: Material constants of MJC model for the grades 7N and 22N.

<i>Alloy</i>	A_1	A_2	A_3	A_4	λ_1	$\lambda_2 (*10^{-4})$
7N	312.08	56.67	9.45	0.03419	-0.00297	3.9086
22N	335.97	402.73	-480.18	0.03264	-0.00331	3.7783

4.2.3. Model D8A

Model D8A is thermo-viscoplastic constitutive equation developed to represent the flow behavior of IFAC-1 SS by Samantaray et al. [60]. Model D8A mathematically expresses the flow stress as:

$$\sigma = (D_1 + D_2(\varepsilon_r(1 - \exp(-\varepsilon/\varepsilon_r)))^n) \exp\{-(D_3 + D_4\varepsilon)(T - T_r) + (D_5 + D_6(T - T_r)) \ln \varepsilon^*\} \quad (4.4)$$

where D_1 represents the yield stress, D_2 is the strain hardening coefficient, D_3 represents the absolute effect of temperature, D_4 represents the coupled effect of temperature and strain, D_5 signifies the absolute effect of strain rate, D_6 represents the coupled effect of temperature and strain rate, n is the strain hardening exponent, $\varepsilon^* = \varepsilon/\varepsilon'_0$ and ε_r signifies the average critical strain for recovery. The eight material constants D_1 , D_2 , D_3 , D_4 , D_5 , D_6 , n and ε_r for three grades of 316LN have been obtained following the procedure described in [117]. The calculated constants are listed in Table 4.3. The flow curves predicted using these constants are compared with the experimentally determined flow curves in Fig. 4.8.

Table 4.3: Material constants of Model D8A for the grades 7N and 22N.

<i>Alloy</i>	D_1	D_2	D_3	$D_4 (*10^{-4})$	D_5	$D_6 (*10^{-4})$	n	ε_r
7N	99	292	0.0028	6.34	0.038	3.67	0.077	0.3
22N	175	288	0.0029	6.90	0.040	3.86	0.137	0.3

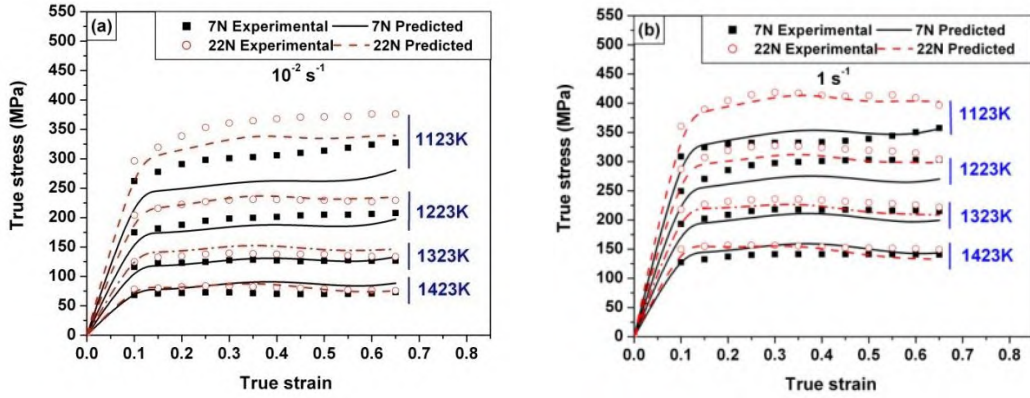


Figure 4.6. Experimentally obtained and SCA-predicted flow curves for 7N and 22N grades of 316LN in the temperature domain of 1123-1423K at strain rate (a) 0.01 s^{-1} and (b) 1 s^{-1} .

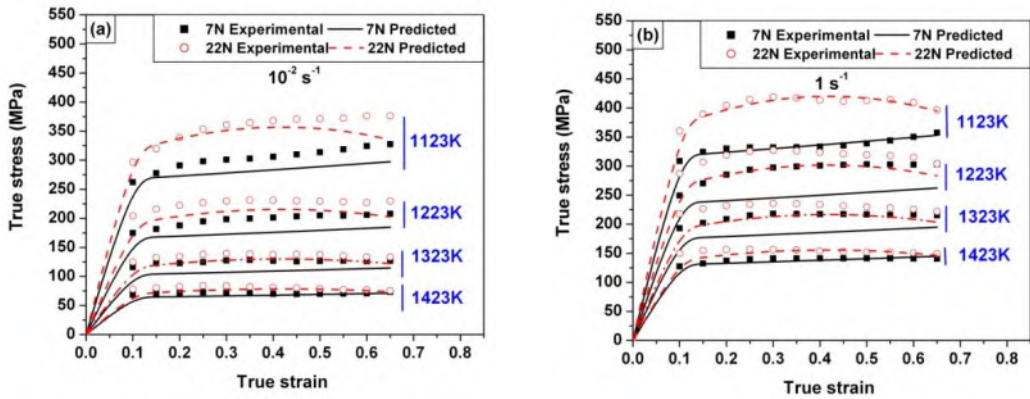


Fig. 4.7: Experimentally obtained and MJC-predicted flow curves for 7N and 22N grades of 316LN in the temperature domain of 1123-1423K at strain rate (a) 0.01 s^{-1} and (b) 1 s^{-1} .

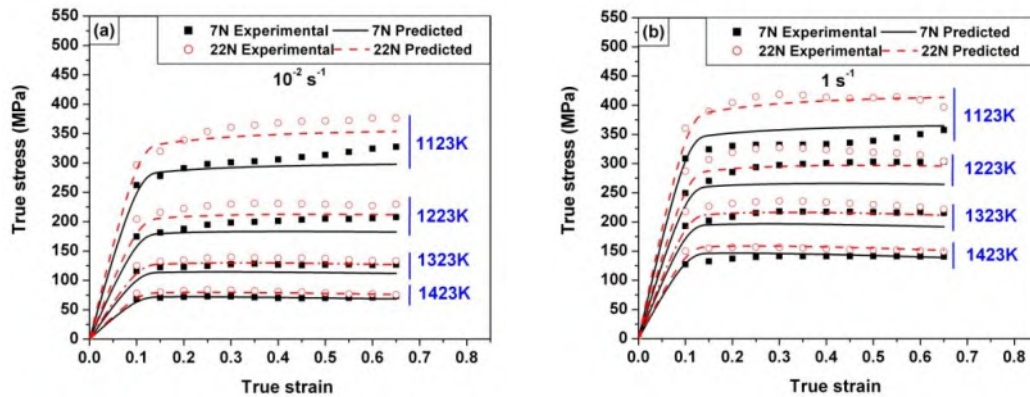


Figure 4.8: Experimentally obtained and model D8A-predicted flow curves for 7N and 22N grades of 316LN in the temperature range of 1123-1423K at strain rate (a) 0.01 and (b) 1 s^{-1} .

4.2.4. Artificial Neural Network (ANN)

ANN model uses multilayer perceptron (MLP) based feed-forward network with back-propagation (BP) learning algorithm [119] for prediction of data sets, where the relationship between data elements varies frequently. This algorithm has been used to predict complex flow behavior of materials on several occasions [63, 120, 121]. Fig. 4.9 illustrates the schematic of the model where process variables such as strain, strain rate, temperature and chemical composition are given as the inputs to the model, and flow stress is predicted as the output.

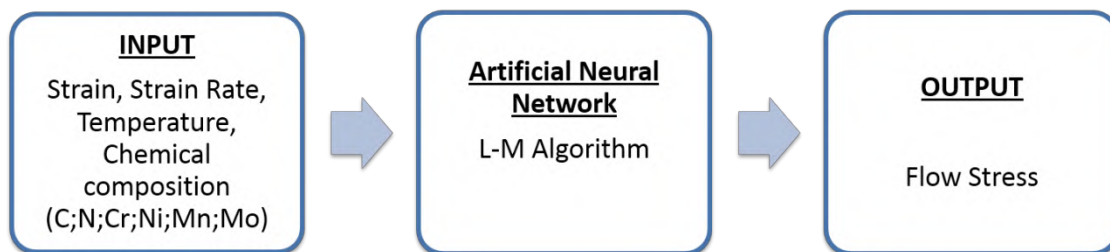


Figure 4.9: Artificial Neural network architecture used in the present study.

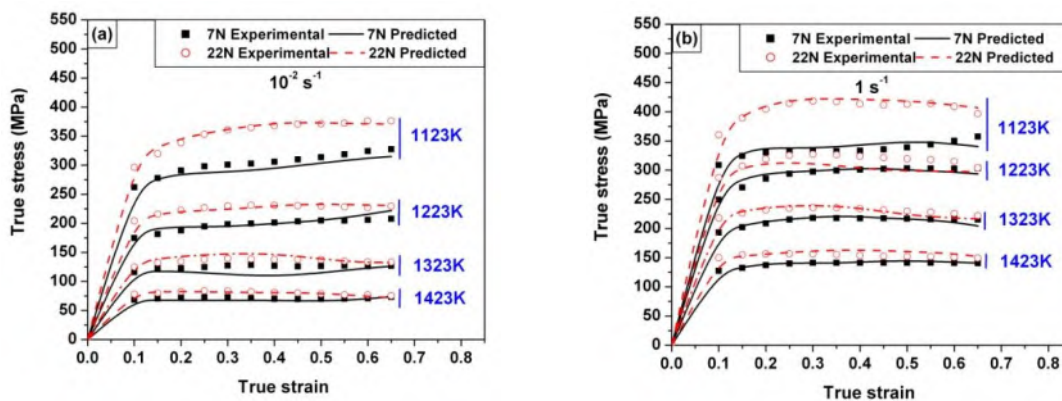


Figure 4.10: Experimentally obtained and ANN-predicted flow curves for 7N and 22N grades of 316LN in the temperature range of 1123-1423K at strain rate (a) 0.01 and (b) 1 s^{-1} .

For the present problem, one hidden layer with 10 neurons was chosen. The training process was optimized using Levenberg – Marquardt (L-M) algorithm as a back-propagation algorithm and sigmoidal function as an activation function [61, 122, 123]. Data points comprising 60% of the experimentally generated dataset were randomly selected. These data points were used to train the neural network. To evaluate the quality of the training, 10% of the dataset was used. This 10% data was not included in the 60% previously used for training. Success of the training was verified by comparing the predicted data against the afore-mentioned 70% of the experimental data. Correlation coefficient of 0.99 was chosen as the criterion to ensure good quality of training. Upon successful completion of the training, the developed neural network was used to predict the flow curves in the entire tested regime for 7N and 22N grades. Fig. 4.10 compares the predicted flow curves with the experimental data obtained for representative test conditions.

4.3. Various aspects of thermo-viscoplastic constitutive models

It is evident from the available literature that the efficiency of a constitutive model is usually decided on the basis of statistical parameters associated with the error in prediction [53]. However, this statistical analysis, while necessary, is not necessarily sufficient when a constitutive model is evaluated from the perspective of alloy development. Therefore, five additional factors along with the usual statistical error analysis have been taken into account while assessing the efficiency of the models. These six factors are

4.3.1. Statistical Evaluation

This criterion appraises the error in the prediction of data as well as the ability to correctly reproduce observed trends. A qualitative comparison of the predicted flow stress

by different models with the experimental flow stress has already been showcased in Fig.4.6, Fig.4.7, Fig.4.8 and Fig.4.10. Though these figures provide a qualitative idea about the capability of a model to track the flow behavior with progress of deformation to certain strain level; from this pictorial presentation, it is difficult to zero-in on the optimal model. This difficulty invokes the necessity for quantifying the predictability of different models. In the field of statistical analysis, there exist many mathematical parameters which can quantify the proximity or difference between two sets of data. These parameters are described below.

For an ideal constitutive equation the difference between the predicted values and the experimentally obtained values is expected to be zero. However, this cannot be achieved in practice as no model can represent the physical behavior completely. Therefore, a constitutive model is considered a good model when the difference between experimentally obtained flow stress and predicted flow stress is close to zero. This difference is frequently quantified by the ‘Average Absolute Relative Error (AARE)’, which is mathematically defined as [117]:

$$AARE = \frac{1}{N'} \sum_{i=1}^{i=N} \left| \frac{\sigma_{\text{exp}}^i - \sigma_{\text{pre}}^i}{\sigma_{\text{exp}}^i} \right| \times 100 \quad (4.5)$$

where σ_{pre} is the predicted flow stress, σ_{exp} is the experimental flow stress and N' is the total number of experimental data points. In addition to minimizing AARE, the predicted stress-strain curve should bear geometrical similitude to the experimental stress-strain curve without scaling. This congruence can be verified by visual inspection and quantified by the ‘correlation coefficient (R)’, which is defined as:

$$R = \frac{\sum_{i=1}^{i=N} (\sigma_{\text{exp}}^i - \overline{\sigma_{\text{exp}}})(\sigma_{\text{pre}}^i - \overline{\sigma_{\text{pre}}})}{\sqrt{\sum_{i=1}^{i=N} (\sigma_{\text{exp}}^i - \overline{\sigma_{\text{exp}}})^2 \sum_{i=1}^{i=N} (\sigma_{\text{pre}}^i - \overline{\sigma_{\text{pre}}})^2}} \quad (4.6)$$

where $\overline{\sigma}_{pre}$ and $\overline{\sigma}_{exp}$ are the mean predicted stress and mean experimental stress values.

A value of R equal to 1 implies that there exists a perfect linear relationship between the experimental and predicted data, while a value of 0 implies that there is no linear correlation between the two sets of data. Therefore, a higher value of R often connotes better predictability of the model, yet is not the absolute parameter to measure it. The linear correlation between the experimental stress and predicted stress, if one exists, can be mathematically represented as

$$\sigma_{pre} = I + S\sigma_{exp} \quad (4.7)$$

where I is the intercept and S is the slope of the correlation line. Ideally, the value of I should be 0 and the value of S should be 1. Either over-prediction or under-prediction is indicated by $I \neq 0$ and $S \neq 1$. In addition, standard deviation (SD) must also be considered as this quantifies the deviation of data points from the correlation line. A lower SD always connotes better predictability of a model compared to others. Considering these facts all the above described parameters have been monitored for different models and compared to identify the most suitable one among them. The values of the parameters are enlisted in Table 4.4. On the basis of the number of parameters for a model closer to their ideal values, a model can be recommended for the use. In order to represent this recommendation graphically, the four models have been assigned scores based on the parameters of Table 4.4. The plot shown in Fig. 4.11 represents these parameters in three-dimensions; the standard deviation of the model, average of ARRE and intercept (I), and average of R and slope (S) of correlation line.

The scores of each model are assigned by normalizing each axis variable (for eg. standard deviation) with the maximum value of the variable (example highest standard deviation). Subsequently, these normalized values have been used to find the magnitude

of the vector joining the ideal model and the concerned model; a higher magnitude indicating greater deviation from an ideal model. The significance of vector magnitude is described as follows. For an ideal model, correlation coefficient (R) associated with the prediction and slope (S) of the correlation line should be ≈ 1 . AARE, intercept (I) and standard deviation should be ≈ 0 . Considering the similar magnitude of the values, while R and S are represented by one axis, AARE and intercept (I) are represented by another axis of the three dimensional space (Cube) represented in Fig.11. For both the cases 50% weightage has been assigned to each value by taking average. The point with coordinate $(R+S)/2=1$, $(AARE+I)/2=0$ and $SD=0$ has been marked 'ideal condition' in Fig. 11. With increasing deviations from ideality, the coordinate changes. The position vector beginning from the ideal point and ending at the co-ordinates of a specified model would be longer. Therefore, shorter is the vector, more accurate is the model. The scores indicated in Fig. 4.11 show that ANN is closer to the ideal model compared to all other models, hence ANN is scored highest on statistical evaluation.

4.3.2. Ability to correctly represent flow instabilities in the tested domain

Instability of various forms can occur during hot deformation under certain conditions. In these cases, local variations in material flow are not representative of the bulk material flow characteristic. The manifestations of such instability could be strain rate softening rather than strain rate hardening, anomalous thermal softening etc.

In the tested grades of the material, flow instability is manifested by negative strain rate sensitivity and is confined to the domain of high strain rate and low temperatures, while in rest of the domain, the flow behavior shows positive strain rate sensitivity.

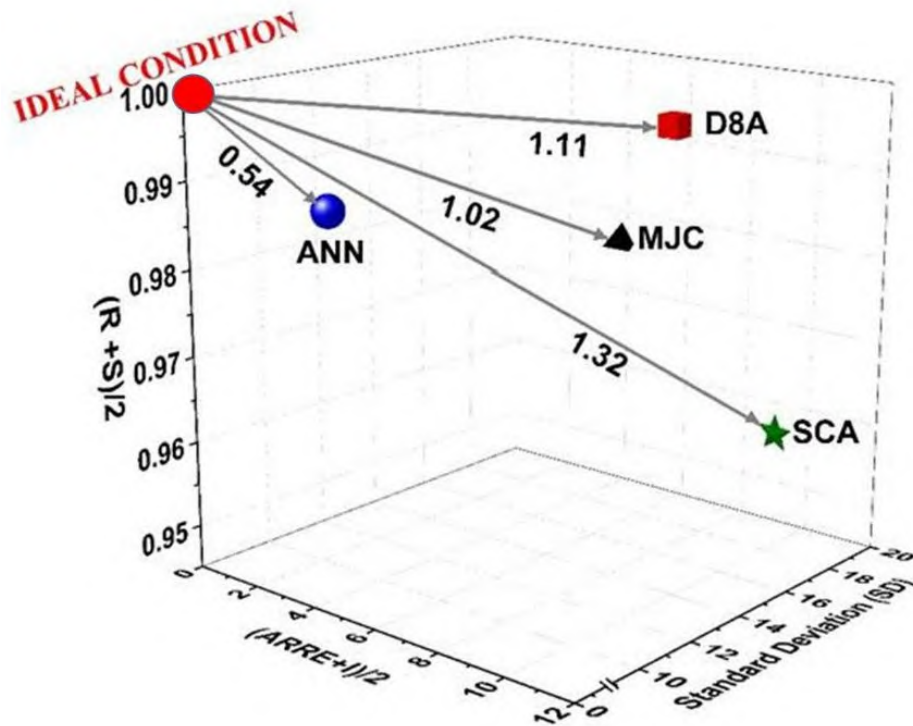


Figure 4.11: Statistical evaluation of different models using the same dataset. Numbers on arrows indicate deviation from ideal model.

Table 4.4: Statistical parameters obtained for predictions by various models.

Model	Parameters	SCA	MJC	D8A	ANN
7N	AARE	9.22	8.25	7.63	4.61
	R	0.978	0.9788	0.977	0.995
	I	12.27	-1.86	-1.24	1.58
	S	0.93	0.96	1.032	0.98
	SD	18.11	18.64	20.65	9.14
22N	AARE	6.84	6.85	6.88	3.36
	R	0.985	0.983	0.981	0.996
	I	12.48	-0.014	6.41	3.704
	S	0.945	0.986	0.973	0.98
	SD	18.0	20.192	20.973	9.111

The addition of alloying components can change material behavior and lead to flow instabilities through mechanisms like segregation, boundary decohesion, local strain

variations etc. [118]. An optimal constitutive model should correctly represent the flow characteristic during the flow instability, besides during stable flow conditions. From the Table 4.4, it can be noticed that the prediction capability of ANN model is better than SCA, MJC and D8A. The prediction by ANN shows SD and AARE almost half of the SD and ARRE associated with the predictions by other models. From the analysis of the data obtained by prediction, it is observed that predictions by SCA, MJC and D8A largely fail in the domain of instability, which is shown in Fig.4.12.

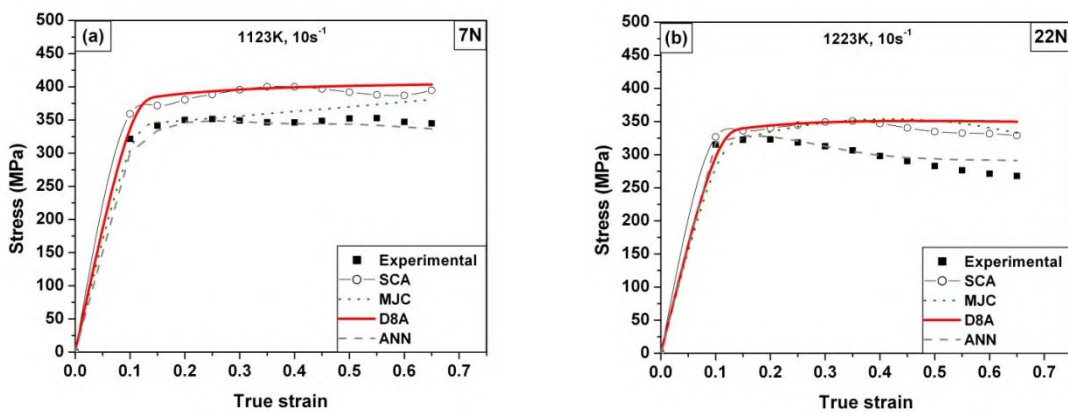


Figure 4.12: Comparison of experimentally obtained and predicted flow curves by various models in unstable domain for (a) 7N and (b) 22N grades of 316LN.

In constitutive models such as D8A, MJC and SCA, the absolute strain rate sensitivity is usually characterized by a material constant. This constant either carries a positive or negative numerical value, which mostly depends on the flow behavior of the material manifested over a larger part of the experimental domain. As example, in the present case, the material shows positive strain rate sensitivity over strain rate domain 0.001 - 1s⁻¹ at all temperatures. The data corresponding to this domain accounts for approximately 80% of the entire data population. Therefore, during optimization of the constant which represents strain rate sensitivity, the local characteristic of negative strain rate sensitivity gets suppressed. Consequently, when this constant is used for prediction,

local behavior the material is not perfectly depicted (which can be seen from Fig.4.12), though the model predicts the global behavior satisfactorily.

In cases of ANN, 60% of the experimentally generated dataset are chosen randomly for training, comprising data from both stable and unstable domains. Again, this algorithm does not use a logical constant or a specific equation to predict the flow behavior. As a result, the prediction in both stable and unstable domains remains equal, which is not possible with the models having constrained mathematical forms.

4.3.3. Provision for easy integration of additional variables: integration of chemical composition

Hot deformation is a complex process which depends on several, often inter-related variables. With continuous improvements in alloying and processing methods, it is increasingly necessary to incorporate more variables and factors into the prediction of flow stress. It is desirable that these additional variables can be incorporated in a modular fashion, i.e. without changing the entire equation. Formulation of SCA model is a classic example of such a case. The effect of strain on flow behavior was not considered in the original form of Arrhenius-type equation. The equation was later modified to incorporate the effect of strain without compromising the original form of the equation. The modified model (SCA) is quite useful for flow prediction though the number of constants increases significantly. This provision in a model can greatly facilitate alloy development and related studies, if the number of constants can be kept limited. In the present case, the nitrogen content of the steel has been taken as a new variable as the addition of nitrogen significantly modifies the flow behavior.

It has been seen from the Fig.4.5 that the nitrogen significantly affects the yield stress and strain hardening behavior of the material, therefore, the effect of the nitrogen

content can be expected on the parameters which represent these properties. A close examination of the constants given in Table 4.1, Table 4.2 and Table 4.3 reveals that the material parameters which represent the effect of strain on deformation vary with change in nitrogen content.

In case of SCA model, all the coefficients of the polynomials, used to represent n' , α , Q and $\ln A$ as functions of strain change with variation of nitrogen content. To incorporate the effect of nitrogen, all the coefficients have to be expressed as functions of nitrogen. While the coefficients of Q and $\ln A$ readily give scope for the incorporation of nitrogen content due to presence of similar number of coefficients for variants 7N and 22N (i.e. four coefficients), coefficients of n' and α do not give any scope for it. This is because there are five coefficients each for Q and $\ln A$ for 7N variant and six coefficients each for Q and $\ln A$ for 22N variant. Therefore, it can be concluded SCA is not a suitable model for further amendment. This observation implies that any model which includes a polynomial (of no fixed order) form is not suitable for further amendment. However, in cases where the coefficients are similar in number, there always is a chance of increase in the number of material constants after the amendment, which may not be always acceptable due to added complexity.

In D8A, the parameters D_1 and n found to vary with nitrogen content in the steel. Therefore, to incorporate the effect of nitrogen on flow stress these parameters are presented as linear functions of nitrogen.

$$\begin{aligned} D_1 &= E_1 + NE_2 \\ n &= m_1 + Nm_2 \end{aligned} \tag{4.8}$$

where N is the nitrogen content of the steel in wt. %. With the above modification the Eq.4.4 can be rewritten as

$$\sigma = (E_1 + NE_2 + (E_3(\varepsilon_r(1 - \exp(-\varepsilon / \varepsilon_r)))^{(m_1+m_2N)}) \exp \{-(E_4+E_5\varepsilon)T^* + (E_6 + E_7T^*) \ln \varepsilon^{i*} \} \quad (4.9)$$

where E_3, E_4, E_5, E_6, E_7 are average values of D_2, D_3, D_4, D_5 and D_6 respectively, calculated at various nitrogen contents.

Similarly, in model MJC, the material constants A_1, A_2, A_3 and λ_1 show strong dependency on nitrogen content. Therefore, these constants have been modified as

$$\begin{aligned} A_1 &= B_1 + NB_2 \\ A_2 &= B_3 + NB_4 \\ A_3 &= B_5 + NB_6 \\ \lambda_1 &= \mu_1 + N\mu_2 \end{aligned} \quad (4.10)$$

with the use of Eq.4.8, Eq.4.3 can be rewritten as ‘N-amended MJC’ as follows

$$\sigma = ((B_1 + NB_2) + (B_3 + NB_4)\varepsilon + (B_5 + NB_6)\varepsilon^2)(1 + B_7 \ln \varepsilon^{i*}) \exp \left[\left((\mu_1 + N\mu_2) + \mu_3 \ln \varepsilon^{i*} \right) (T - T_r) \right] \quad (4.11)$$

where B_7, μ_3 are the average values of A_4 and λ_2 respectively, calculated at various nitrogen contents. After modification, both the equations have equal number of material constants. The material constants of N-amended MJC and N-amended D8A are shown in Table 4.5 and Table 4.6, respectively. There is no necessity for further modification to ANN model as material parameters are given as input at the beginning.

Table 4.5: Material constants for N-amended D8A.

E_1	E_2	E_3	E_4	$E_5(*10^{-4})$	E_6	$E_7(*10^{-4})$	m_1	m_2	ε_r
63.53	506.67	290	0.029	6.62	0.039	3.76	0.049	0.4	0.3

Table 4.6: Material constants for N- amended MJC model.

B_1	B_2	B_3	B_4	B_5	B_6	B_7	μ_1	μ_2	μ_3 (* 10^{-4})
300.9	159.26	-104	2307	237.94	-3264	0.0033	-0.0028	-0.0023	3.843

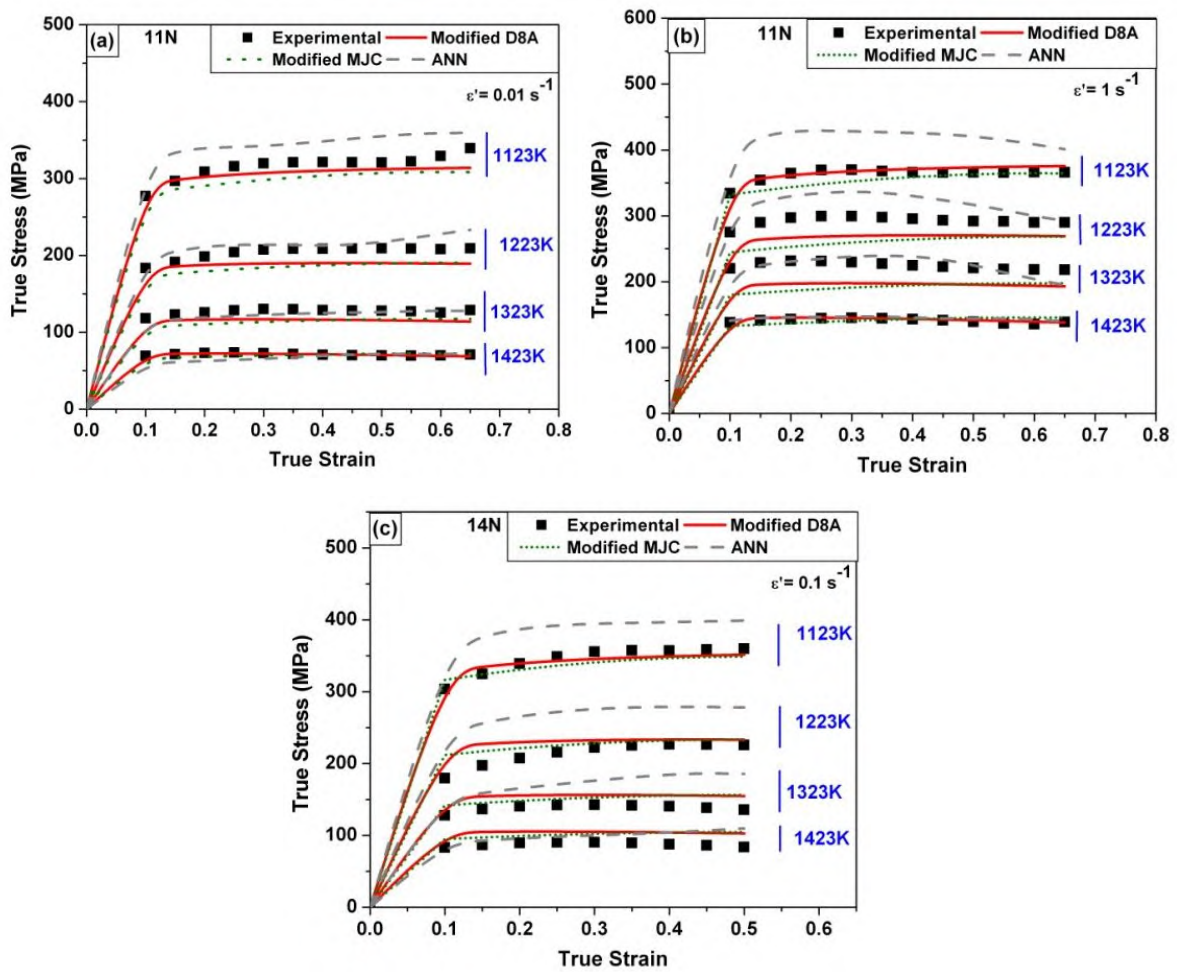


Figure.4.13: Comparison of experimentally obtained and predicted flow curves by N-amended MJC, N-amended D8A and ANN model for (a) 11N at 0.001s^{-1} and (b) 11N at 1s^{-1} and (c) 14N at 0.1s^{-1} .

4.3.4. Possibility of usage of the model for extrapolation

The need to modify an existing model frequently arises from the inability of the original model to predict the flow behavior in a domain much larger than the experimentally tested domain. The process of prediction of flow behavior at finer intervals in a domain where the applicability of model has been validated by experiments is called interpolation. The process of prediction of flow stress beyond the validated domain is called extrapolation. When minor changes in alloy composition are made, it may not be convenient to test each alloy variant at each deformation condition. The ability to extrapolate a model can greatly reduce time, material requirement and expenditure, which are crucial for industry. In the present study, this factor has been used to predict the flow stress behavior of two variants, i.e. 11N and 14N having different chemical composition.

Table 4.7: Statistical parameters obtained for predictions by various models.

Model		MJC	D8A	ANN	Remarks
11N	AARE	7.22	6.82	9.64	D8A is the best Followed by MJC
	R	0.98	0.98	0.99	
	I	2.20	-1.39	-16.41	
	S	0.95	0.99	1.17	
	SD	17.04	17.91	15.99	
14N	AARE	8.5	10.4	19.62	MJC is the best Followed by D8A
	R	0.99	0.99	0.99	
	I	25.32	28.58	16.20	
	S	0.91	0.91	1.10	
	SD	6.82	8.57	14.37	

The extrapolation of any trend beyond the experimental conditions is inherently risky since the actual material behavior may vary significantly outside the tested

conditions. However, within allowable limits, the material behavior may be assumed to follow broadly similar trends. In such cases, a constitutive model should be able to extrapolate/interpolate the flow stress behavior with reasonable accuracy. This ability can be a factor to distinguish between different constitutive models. To verify the abilities of the constitutive models which have been developed using the experimental data of 7N and 22N steels, flow curves for 11N and 14N grades have been predicted. The prediction is validated against the experimental data generated for 11N and 14N. Comparison of the experimentally generated flow curves at some selected conditions and predicted flow curves by N-amended MJC, N-amended D8A and ANN is shown in Fig. 4.13. The statistical data for the prediction is given in Table. 4.7. It can be noticed that both N-amended MJC and N-amended D8A are able to interpolate the flow behavior of 316LN SS successfully for the other grades of steel. However, the error associated with the prediction by ANN model is significantly higher than the error associated with the other two models. This finding contradicts the general belief in interpolation capability of ANN model. The large deviation can be attributed to the lack of training of the model at such conditions. This finding demonstrates that when the required ratio of data needed for training to the data needed for prediction (which is usually 7: 3) reduces, the prediction capability of the model declines. Therefore, ANN model is not reliable when a large data set has to be predicted by using a smaller available data set.

4.3.5. Ease of usage

The advent of high performance computing has enabled the development of highly accurate and complex models in various fields. However, this complexity may often become a burden for production engineers in an industrial environment. For the constitutive model to be industrially relevant, the physical inputs should be few, there

should be minimum requirement of special modelling/computational skills, and most importantly, the model should be robust. The robustness of the model is not only determined by the range of processing conditions which it can represent, but also by high repeatability and high reproducibility of the predicted results. The ease of usage of a model determines its acceptability in an environment where time and productivity is of essence. A model which is easy to use can be rapidly deployed for different alloy compositions, whereas a computation-intensive and knowledge-intensive model may be cumbersome to use.

A model which is system-specific or which produces different results in different runs can potentially complicate operations by introducing variations, whereas standardization and consistency are the demands of industrial production. Both N-amended MJC and N-amended D8A fully satisfy these criteria as these two models are presented in simple mathematical form and the calculation of flow stress is not system or operator-dependent. On the contrary, ANN model demands some computational skill and the results are highly system- and operator-dependent.

4.3.6. Ability to connote the metallurgical properties

During alloy development, it is often desired to interpret mechanical/metallurgical response in terms of properties such as strain rate sensitivity, strain hardening, yield stress etc., while studying the deformation behavior of the alloy. From the flow behavior analysis, it is observed that addition of nitrogen content significantly affects the yield point of the material and strain hardening behavior. This behavior should also be reflected in the constitutive model, in order to make the model useful if it is required to identify effect of elements on yield point, strain hardening, thermal softening etc. On account of this, the effect of nitrogen addition is clearly visible on these constants D_1 and n of D8A

which signify yield point and strain hardening of the material, respectively. Therefore, if required, N-amended D8A can directly be used to identify the influence of nitrogen on yield point and strain hardening at different temperatures and strain rates. However, in MJC and SCA, though the effect of nitrogen is visible on all the coefficients of strain, it is difficult to logically distinguish the influence of nitrogen on any specific material property. Therefore, N-amended MJC may not be as useful as N-amended D8A to study the influence of nitrogen on yield point and strain hardening at different temperatures and strain rates. In such cases ANN too will not be very useful, as additional training is the pre-requisite for any new prediction. However, additional calculations on predicted flow stress can give the required results.

A model whose constants can connote the physical properties is thus preferable to a ‘black-box’ model where the sum of parts is known but the individual parts are hidden. Even if the individual parts are known, it may not always be possible to interpret them in terms of physical properties. Such a model is limited to flow stress prediction, and cannot be readily used for material comparison or analysis of different responses at different deformation conditions. In such cases, the ANN model performs excellently, considering all the local variation. However, performance of ANN deteriorates as the fraction of data to be predicted slowly increases. In addition, the prediction is highly dependent on system and computational skill of the user. The model needs fresh training for every additional output. In light of the above, ANN is not recommended for interpolation and extrapolation, especially during alloy development. On such occasions modified mathematical models such as N-amended model D8A and N-amended MJC perform satisfactorily. These models give scope for addition of new parameters which account for the effect of element addition on the flow behavior, while also performing consistently during interpolation. Though these models cannot depict divergent behavior at specific

deformation conditions, they effectively represent the aggregate, global behavior of the material, which is necessary knowledge for an alloy designer.

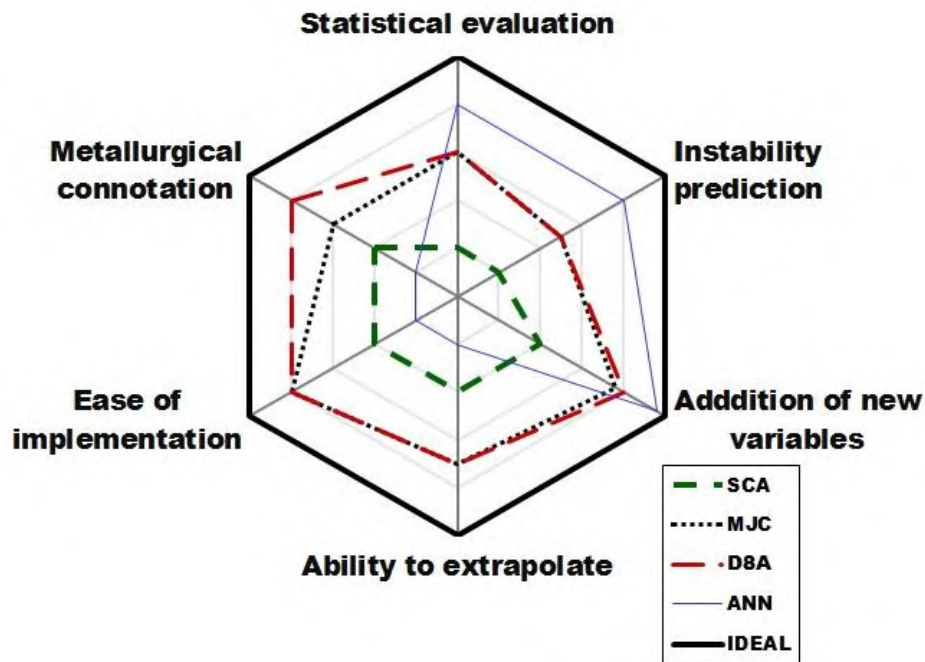


Figure 4.14: Radar chart comparing performance of different models on the basis of six factors.

The above discussed points are schematically represented by the radar chart shown in Fig. 4.14. A similar approach has earlier been used by Holota et al. [124] for selection of material. The six ‘spokes’ of the chart each represent the six factors discussed a priori, on the basis of which relative performance of models can be assessed. Each model is represented by a closed loop. The six radii of this loop represent how well the model performs, with a higher radius indicating better performance and thus a better model. For instance, in Fig. 4.12, it is seen that ANN model performs well in instability prediction, but poorly in ease of implementation. On the contrary, MJC model performs well in ease of implementation but not as well in predicting instabilities. In view of the above discussed points and Fig. 4.14, it is clear that ANN model is a good choice when large fraction of data (70% of entire data set) is available for training and a comparatively small fraction of the data (30% of entire data set) has to be predicted. However, when all

six criteria are considered, Model D8A is closest to the ideal model, and hence, is an optimal choice from the perspective of alloy development.

4.4. Conclusions

The flow behavior of 316LN was investigated in the temperature domain of 1123-1473K at strain rates $0.001 - 10s^{-1}$. The key outcomes of this study are summarized below:

- Hot deformation of 316LN SS is found to depend on processing parameters, such as strain level, strain rate, deformation temperature and enhancement of nitrogen content in steel. Increase in nitrogen content in 316LN intensifies the work hardening in the material.
- The utility of constitutive equations for prediction of flow behavior during alloy development stage has been analyzed using experimental results obtained from four grades of 316LN. For this study four commonly used models such as SCA, MJC, Model D8A and ANN model have been critically compared on the basis of six criteria.
- Both MJC and Model D8A are found suitable for their ease of use and scope for addition of new variables for alloy development. The modified versions of these two models, namely N-amended MJC and N-amended D8A, developed using experimental data of 7 N and 22 N grades satisfactorily predict the flow behavior of 11 N and 14 N grades of 316LN. N-amended D8A is preferred to N-amended MJC as constants of the former model can be directly used to represent the effect of nitrogen on yield stress and work hardening.

Role of nitrogen on dynamic recrystallization in 316LN during hot working

5.0. Preamble

This chapter elucidates the effect of nitrogen content on the dynamic recrystallization (DRX) behavior of a 316LN SS. The strain rate-dependency of DRX nucleation is explained on the basis of interstitial content, which changes the SFE. The last part of chapter presents the rate- dependent grain growth for 316LN SS.

5.1. DRX characteristics

The flow curves obtained from the hot compression tests discussed in Chapter.4 also contains valuable information about the DRX process. Poliak and Jonas [68] developed an analytical technique combining plasticity, irreversible thermodynamics and geometry to deduce the strain level at which DRX initiates. This strain level, termed ‘critical strain’, is a macroscopically averaged parameter representing the measurable initiation of DRX, and has been successfully applied to several materials [66, 67, 74, 125-127]. In the present study, critical strain was used to analyze the macroscopic changes in DRX resulting from change in nitrogen content. In practice, critical strain corresponds to the inflection point in the work hardening ($\theta=d\sigma/d\varepsilon$) – stress (σ) curve. This is graphically shown in Fig. 5.1. The local minima of $(-\partial\theta/\partial\sigma)$ vs. σ plot is considered to be point of critical stress (σ_c) and the corresponding strain is called critical strain (ε_c) for DRX. The above methodology has been followed to obtain critical strains for all the flow curves. The θ vs σ plot (shown in Fig.5.1) can be broadly divided into three domains; hardening, hardening + DRX and DRX. The domain where a positive θ ($\theta >0$) holds

linear relationship with σ represents dominant hardening behavior of the steel. Beyond the critical stress, there exists an intermediate state, where θ is positive, but no longer has a linear relationship with σ . In this domain work hardening and DRX are simultaneously operative. The third domain is the domain of DRX where θ assumes negative value. Analysis of these domains can give a better insight into the DRX behavior of 316LN with variation in temperature, strain rate or nitrogen content.

5.2. Temperature sensitivity of DRX in 316LN

To understand the effect of temperature on various DRX domains, the θ vs σ plots for 7N, 11N and 22N steels at various temperatures for strain rate 0.001s^{-1} have been plotted in Fig 5.2a. The variation of critical strain with temperature has been plotted in Fig.5.2b. Influence of nitrogen on different domains can also be noticed from the Fig.5.2a. At 1223K, magnitude of work hardening for 7N variant is lower than that is noticed for 22N variant. This difference is maintained for all the conditions shown in Fig.5.2a, such behavior can be attributed to the strengthening effect provided by nitrogen to steel through pinning of dislocations [113] and obstructing the dislocation motion by elastic interactions [5]. As the consequences of these interactions, stored energy of the material is increased [128]. When the stored energy at some local area reaches the critical value, DRX nucleation takes place. Since 22N nitrogen shows higher stress for similar amount to deformation imparted or a higher work hardening value for a particular stress level, early nucleation of DRX expected in this variant. This can be noticed from the Fig. 5.2b. This indicates that increase in nitrogen content promotes early nucleation in 316LN SS. The critical strain for DRX nucleation is reduced with increase in temperature as shown in Fig. 5.2b. From the Fig. 5.2b, it can also be seen that with increase in

deformation temperature, the critical strain required for DRX nucleation consistently decreases for all the variants.

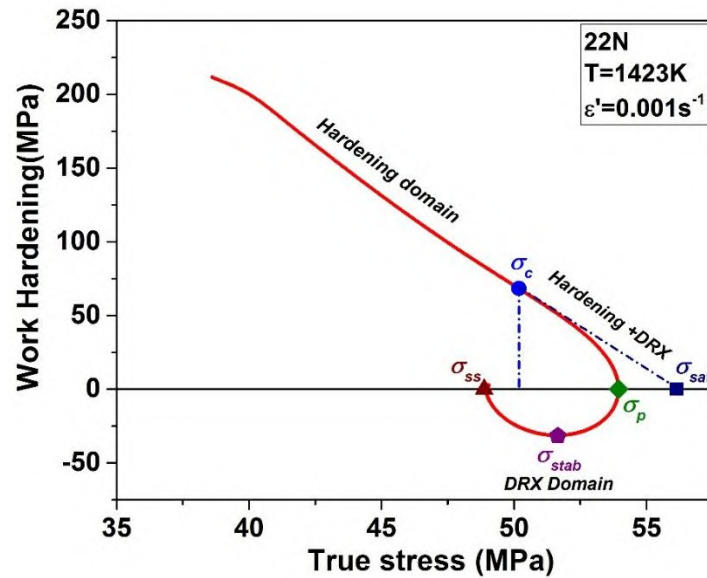


Figure 5.1: Typical θ - σ plot obtained from flow curves to determine the various stress parameters.

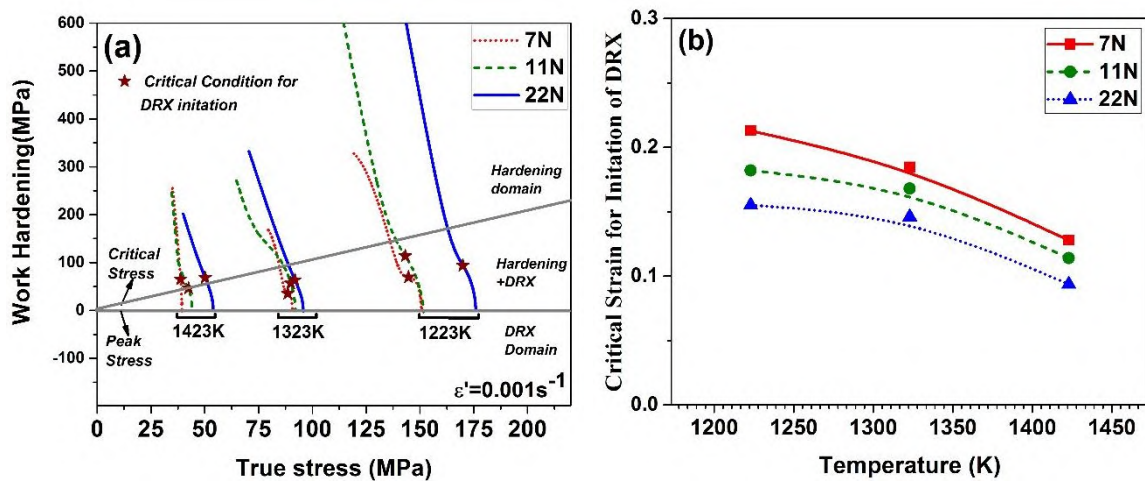


Fig. 5.2 (a) θ - σ plot at different temperatures and (b) critical strain vs temp obtained at $0.001s^{-1}$ strain rates for 7N, 11N and 22N variants of 316LN SS.

Besides the magnitude of work hardening reduces as the deformation temperature increases and so does the second domain which represents work hardening - DRX domain shrink (It can be seen from Fig. 5.2a). This indicates that at the higher temperature, the

thermal energy favors the DRX nucleation at lower level of strain. The availability higher thermal energy accelerates the process which is the reason behind the shrinking work hardening- DRX domain. The effect of deformation temperature on DRX can also be seen in Fig. 5.3. This Figure shows the Grain Orientation Spread (GOS) maps at 1123K and 1423K for 22N at 0.001s^{-1} , where the colored region indicates the DRX grains. GOS for each grain, determined through EBSD studies. Grains with $\text{GOS} < 1^\circ$ are considered to be recrystallized grains, based on conditions previously determined [129, 130].

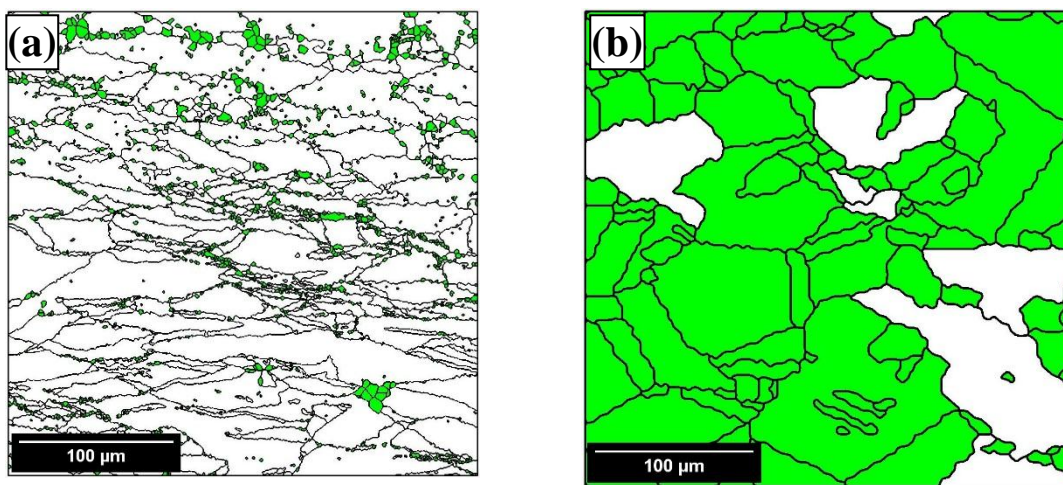


Figure 5.3: Grain Orientation Spread maps of partitioned DRX grains for 22N variant deformed at strain rate 0.001 s^{-1} at, (a) 1123K and (b) 1423K where the colored region represents DRX grains.

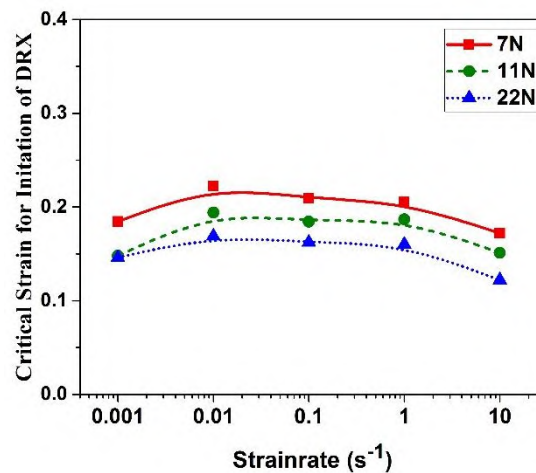


Figure 5.4: Variation of critical strain with strain rate for different variation of nitrogen content at 1323K.

At deformation temperature of 1123K and strain rate of 0.001s^{-1} , the material undergoes DRX, which results in the structure as shown in Fig. 5.3a. This microstructure depicts the initial stage of the discontinuous DRX seen in steels. This necklace DRX structure comprises of the elongated parent grains with freshly nucleated fine DRX grains at grain boundaries, triple junctions and twin boundaries. As the deformation temperature is increased to 1423K, the DRX process accelerates due to availability of higher thermal energy, resulting in a fully DRX structure as seen in Fig.5.3b. As the temperature is increased, the prior grain boundary starts migrating into its surrounding grain in order to lower its energy and nucleates a new grain, which is known as the ‘bulging mechanism’ [131]. Additional input of thermal energy through rise in deformation temperature at 1423K, promotes grain growth. The growth occurs to reduce boundary energy by straightening and hence shortening the grain boundaries[132]. This pattern is common to all the three variants of 316LN SS under investigation.

5.3. Strain rate sensitivity of DRX in 316LN

The DRX behavior is also known to change with deformation strain rate. Fig. 5.4 shows variation of critical strain with strain rate for different variation of nitrogen content at 1323K. At a given strain rate, critical strain increases with decrease in nitrogen content. This again confirms that increase in nitrogen content promotes early nucleation. The critical strain for all three variants is found to initially increase with increase in strain rate (upto 0.01 s^{-1}), and remains nearly constant upto 1 s^{-1} and followed by a decrease at 10 s^{-1} .

The microstructural maps shown in Figs. 5.5-5.7 show the changes in GOS at different deformation conditions for 7N, 11N and 22N variants, respectively.

Statistical treatment of this microstructural data was used to find the number fraction of GOS < 1° grains ('DRX fraction'). DRX fraction is plotted against strain rate in Fig. 5.6 for different variants used in this study. In agreement with the previously reported rate-sensitive DRX behavior in other alloys [129, 130, 133-136], the 7N variant shows lower DRX fraction at intermediate strain rates, when compared to that at lowest (0.001 s⁻¹) and highest (10 s⁻¹) strain rate. Similar decrease in DRX fraction to a minimum value followed by a rise with increase in strain rate was also noticed for the 11N variant.

In contrast, the DRX fraction in the 22N variant is nearly insensitive to change in strain rate. Comparison of these plots, as shown in Fig. 5.8, indicates that the DRX behavior of the alloy at intermediate strain rates is highly sensitive to the interstitial (here N and C) content.

The presence of interstitial elements in an alloy not only modifies the DRX behavior [137, 138] but also has significant influence on microstructural defects [113], such as stacking faults [82]. A stacking fault is a planar defect in an FCC crystal, wherein one HCP layer (with ABAB-type stacking) is embedded in the FCC matrix (having ABCABC-type stacking) [139]. The energy associated with this fault (the SFE) affects the ease of dislocation motion in an alloy, and hence, is deeply interlinked with work-hardening, rate-sensitivity and grain nucleation characteristics. The relationship between SFE and DRX behavior is well discussed in literature. The role of SFE in modifying the DRX behavior of different variants, if any, needs to be investigated. Thus, it is important to obtain the SFE of 316LN SS by varying interstitial content. Experimentally obtained SFE for 316LN SS are mostly reported at room temperature. However, the current study needs evaluation of SFE at DRX temperature. In absence of experimental data in hot working data, a thermodynamic model has been used to predict SFE.

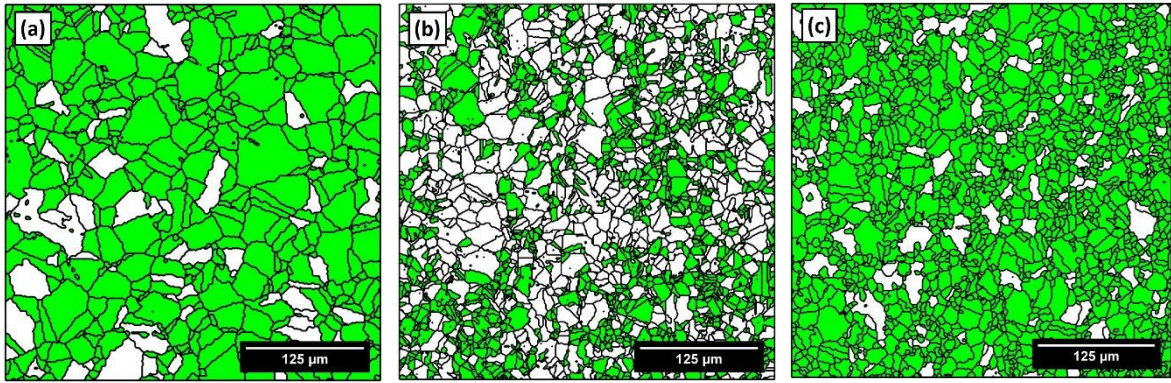


Figure 5.5: GOS maps of partitioned DRX grains for 7N variant deformed at 1323 K, (a) 0.001 s^{-1} , (b) 1 s^{-1} and (c) 10 s^{-1} where the colored region represents DRX grains.

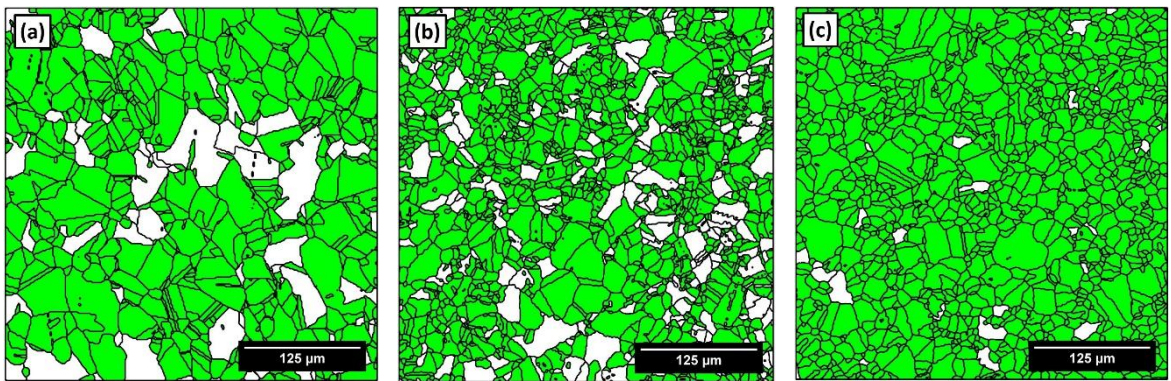


Figure 5.6: GOS maps of partitioned DRX grains for 11N variant deformed at 1323 K, (a) 0.001 s^{-1} , (b) 1 s^{-1} and (c) 10 s^{-1} where the colored region represents DRX grains.

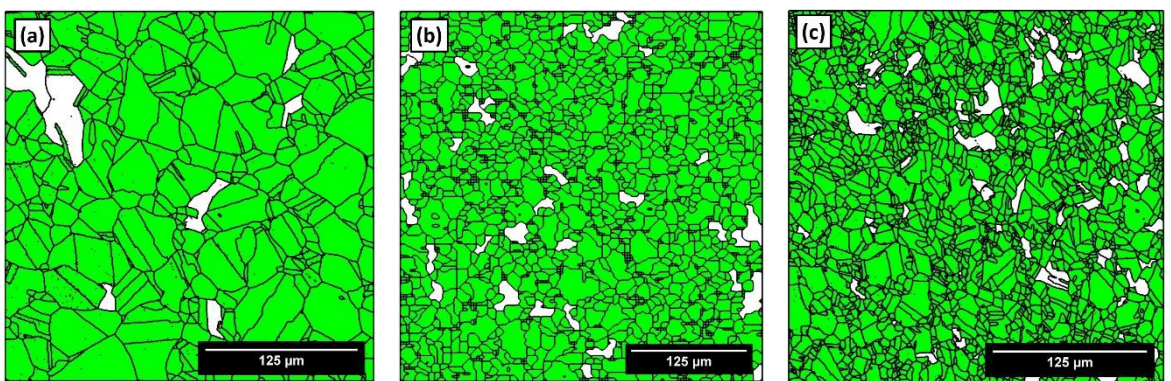


Figure 5.7: GOS maps of partitioned DRX grains for 22N variant deformed at 1323 K, (a) 0.001 s^{-1} , (b) 1 s^{-1} and (c) 10 s^{-1} where the colored region represents DRX grains.

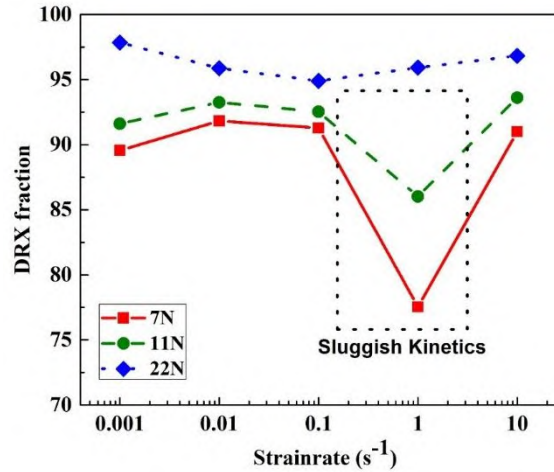


Figure 5.8: Variation of DRX fraction with strain rate for 7N, 11N, 22N variants at 1323K.

5.3.1. Prediction of SFE in hot working domain by varying interstitial content

For each variant, the SFE is predicted by using chemical composition and elemental thermodynamic parameters as inputs to a thermodynamic model. The model used here, is based on the treatment proposed by Curtze et al. [140, 141] for high Mn steels. However, the model has been upgraded for the present work with the following three important modifications:

1. The incorporation of the BCC stabilizer molybdenum (Mo) for the first time as Mo is a crucial element in austenitic steels used at high temperatures.
2. Treatment of carbon (C) and nitrogen (N) as independent interstitial elements, which can have different effects on the SFE.
3. Extending this treatment to high working temperatures, allowing the estimation of SFE at hot working conditions.

Keeping the brevity in view, thermodynamic model has been described in *Appendix A* in detail, only an outline is given here. The SFE is related to change in free energy (ΔG) due

to the transition from FCC (γ) to HCP (ζ) phase in the faulted layer. On this basis, the SFE is represented as [141]:

$$\gamma_{SFE} = 2\sigma_{IE} + 2\psi(\Delta G_{bulk}^{\gamma \rightarrow \zeta} + \Delta G_{Mag}^{\gamma \rightarrow \zeta} + \Delta G_{Seg}^{\gamma \rightarrow \zeta}) \quad (5.1)$$

where σ_{IE} is the interfacial energy in the faulted region, ψ is the molar surface density, $\Delta G_{bulk}^{\gamma \rightarrow \zeta}$, $\Delta G_{Mag}^{\gamma \rightarrow \zeta}$ and $\Delta G_{Seg}^{\gamma \rightarrow \zeta}$ are the changes in bulk free energy, magnetic free energy and free energy due to segregation, respectively.

The bulk free energy term is comprised of contribution from substitutional elements and contribution from interstitial elements, the former being described by:

$$\Delta G_{b(sub)}^{\gamma \rightarrow \zeta} = \sum_i \chi_i \Delta G_{(sub)i}^{\gamma \rightarrow \zeta} + \sum_{ij} \chi_i \chi_j \Omega_{ij}^{\gamma \rightarrow \zeta} \quad (5.2)$$

where $\Delta G_{(sub)i}^{\gamma \rightarrow \zeta}$ represents the contribution from 'ith' substitutional element and $\Omega_{ij}^{\gamma \rightarrow \zeta}$ is the excess free energy due to formation of stable compound by 'ith' and 'jth' elements. χ_i represents the mole fraction of 'ith' element. The bulk energy contribution term given by Curtze et al. [141] is expanded to include $\Delta G_{(sub)Mo}^{\gamma \rightarrow \zeta}$ and $\chi_{Mo} \chi_j \Omega_{Mo j}^{\gamma \rightarrow \zeta}$ terms. Values of these terms were calculated using values from CALPHAD [142]. Similarly, interstitial contribution to free energy given in [143] is expanded to include carbon and nitrogen separately:

$$\Delta G_{b(int)}^{\gamma \rightarrow \zeta} = \chi_C \Delta G_{(int)C}^{\gamma \rightarrow \zeta} + \chi_N \Delta G_{(int)N}^{\gamma \rightarrow \zeta} \quad (5.3)$$

The last two terms of Eq. 5.1, i.e. the magnetic and segregation contributions to free energy are treated using equations (Eq. 3-21) from Curtze et al. [141].

A computer code was specially written to collate and integrate the above equations. To ensure the applicability of the model, it is necessary to validate the model against the experimental results. X-ray diffraction line profile analysis was used to determine the SFE of 7N, 11N and 22N variants at room temperature, using the formalism of Schramm and Reed [144]:

$$SFE \propto \frac{\text{Lattice parameter} * \text{Microstrain}^2}{\text{Stacking fault probability}} \quad (5.4)$$

The proportionality constant comprises shear modulus and anisotropy terms, details of which are described elsewhere [144]. For austenitic steels, we obtain the value 4959.59mJ/m² which is in agreement with [145].

The remaining terms, i.e. lattice parameter, microstrain and stacking fault probability were determined using Rietveld refinement [109] implemented through the program MAUD [110]. The equations related to calculation of microstrain and stacking fault probability are given in *Appendix B*. In order to account for the size-strain anisotropy present in the XRD pattern, the anisotropic model of Popa [111] was used to determine microstrain on the faulting plane. Similarly, the stacking fault probability (probability of finding a stacking fault on (111) plane) was determined using Warren's [146] analysis of peak shifting due to planar defects. The program MAUD allows simultaneous implementation of Popa [111] and Warren [146] models, thereby treating any overlap between effects due to dislocations and due to stacking faults. Further, since the entire XRD pattern is used to obtain a best fit, all information contained in the pattern, i.e. peak position, area under peak, peak shape, tail of peaks, peak asymmetry are used to determine the values needed for Eq.5.4. A recent analysis successfully used this simultaneous refinement approach to study microstructural evolution during tensile testing [145].

A comparison of SFE values obtained through modeling and experiment at room temperature is provided in Table 5.1. It is seen that the model satisfactorily predicts the SFE for all three variants of the 316LN used in this study. Further, SFE decreases with increasing nitrogen content in the range 0.07 wt. % to 0.22wt. %.

In order to extend our thermodynamic model beyond room temperature, we use thermodynamic values of free energy change obtained from [142] to estimate values

of temperature-dependent terms (bulk free energy, magnetic free energy, chemical effects of interstitial segregation) at high temperatures. The values of SFE rise upto 205 mJ/m² to 200 mJ/m² at 1323K with varying the interstitial content (C+N) from 0.1 to 0.25 wt. %. The prediction of SFE with variation of interstitial content and temperature is shown in Fig.5.9.

Table 5.1: Experimental and predicted values of stacking fault energy of 7N, 11N and 22N at room temperature.

Stacking Fault Energy (mJ m⁻²)	7N	11N	22N
Predicted (Thermodynamic Model)	27	26	17
Experimental (XRD Method)	32	25	15

5.3.2. Correlation between SFE and DRX

While DRX is often treated as the *de facto* softening mechanism during hot working of various materials [147], it is important to remember that the DRX process is predicated on a number of favorable conditions. Primary among these prerequisite conditions are: sufficiently high temperature and the accumulation of a critical degree of strain in the matrix [131]. These conditions depend upon factors such as the energy storing/dissipating property of the microstructure [85], the inherent tendency for dislocation annihilation [113], adiabatic temperature rise during deformation [134], and the time available for these processes to occur [131].

The balance between energy storage and energy dissipation in austenitic steel is determined by the lattice distortion (ϑ) which is represented by micro strain [134]. The lattice distortion depends upon the substructure evolved during deformation. The nature of dislocation substructure is derived from the ability of dislocations to cross-slip and annihilate; which is determined by the SFE of the material [71]. For a low SFE material,

cross-slip is hindered and the density of dislocation forests increases during deformation, leading to high energy storage [113, 148]. Upon reaching a critical value of stored energy, the material dissipates energy through the nucleation and growth of new strain-free grains [128, 149]. While storage of energy is necessary, this alone is not sufficient for the initiation of DRX. The second necessary factor is adequate supply of thermal energy to the matrix through isothermal heating (imposed temperature) and/or adiabatic heating (temperature rise due to deformation at high strain rates) [88, 107]. Like any other thermally activated process, DRX is time-dependent as it consists of a grain growth component (in addition to nucleation). The thermal activation for grain growth comes from a conjugate of temperature and time; while temperature provides the driving force for growth, the availability of sufficient time is essential for grain growth to proceed to completion. On the other hand, nucleation is more dependent on stored energy and temperature than on time, with which it shares a complex but weak correlation. Therefore, the overall DRX fraction is expected to have a functional relationship with the above three contributory factors:

$$DRXfraction = f(X_{\vartheta}^i, X_T^i, X_t^i) \quad (5.5)$$

where X_{ϑ}^i , X_T^i , X_t^i are weights assigned to lattice distortion characterized by microstrain (ϑ), temperature (T) and time (t), respectively for a variant 'i' of the 316LN SS. During the deformation of a variant 'i', any change in ϑ , T or t modifies the corresponding values of the weights assigned to these, in such a way that the following conditions are satisfied:

$$X_{\vartheta}^i > 0, X_T^i > 0, X_t^i > 0 \quad (5.6)$$

and

$$X_{\vartheta}^i + X_T^i + X_t^i = 1 \quad (5.7)$$

As example, during deformation of a variant 'i', any increase in strain (ε) at a specified

temperature (T) and strain rate (ϵ'), in absence of any adiabatic temperature rise, increases the weight assigned to lattice distortion, i.e. X_g^i , provided that the Eqs. 5.6-5.7 are satisfied. Similar rise in X_g^i is expected from any source that causes formation of dislocation forests, as opposed to dislocation annihilation processes that decrease the value of X_g^i .

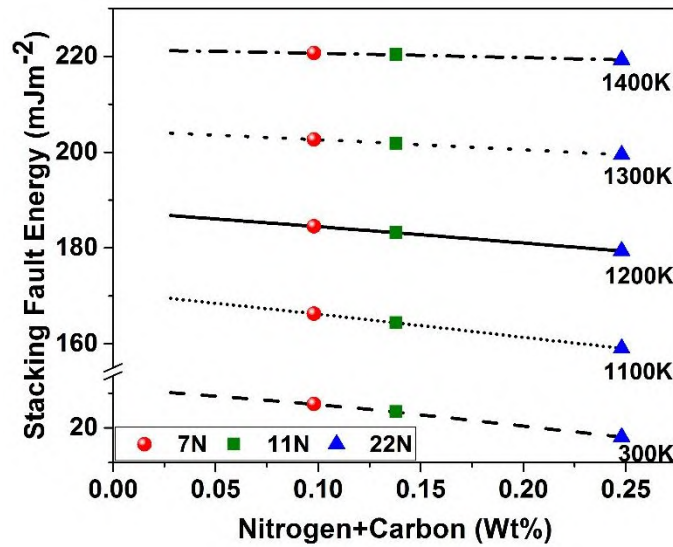


Figure 5.9: Stacking fault energy with varying interstitial content at various temperature

It has already been reported that the probability of dislocation annihilation is lower and the probability of dislocation forest formation is higher in a material with relatively lower SFE [78]. While formation of stacking faults during deformation at low temperatures is well known [140, 150, 151], the existence of these faults at very high temperature is sparsely discussed in literature. Amongst these few reports, an investigation by Taylor et al. [81] has demonstrated that stacking faults can form during the deformation at temperature of 973 K in 304 SS.

The faulting model proposed by Warren [112] enables a quantitative comparison between the extent of faulting for different materials at similar deformation conditions. The extent of faulting is denoted by a ‘stacking fault probability’, which measures the probability of finding a stacking fault on a (111) plane. This can be determined by

Rietveld refinement of the complete diffraction pattern, as earlier demonstrated in [152]. The stacking fault probability so obtained is plotted for different variants in Fig. 5.10. The plot is overlaid with the corresponding micro-strain (ϑ) values on (111) plane to show the simultaneous increase in both parameters with increasing interstitial content.

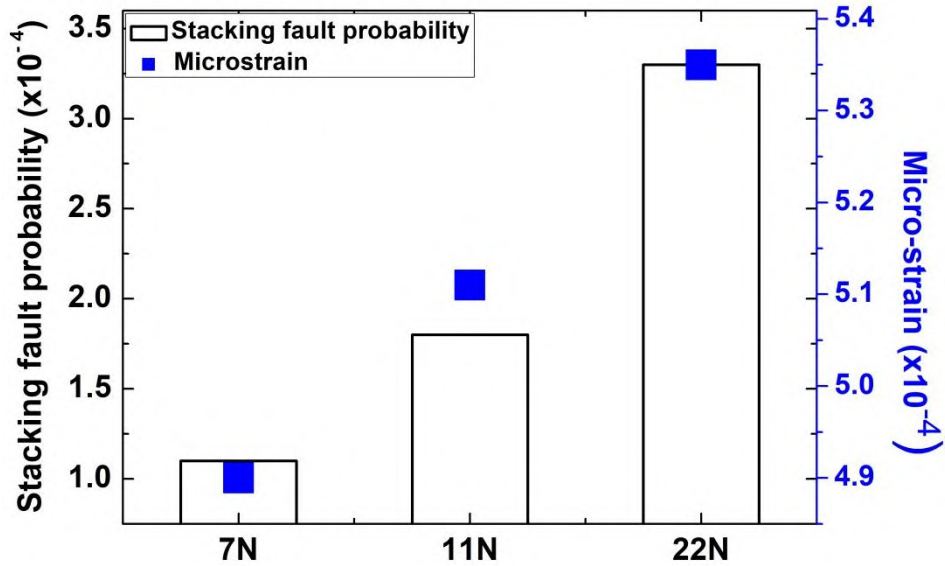


Figure 5.10: Change in stacking fault probability and micro-strain (ϑ) values on (111) plane for 7N, 11N and 22N variants deformed at 1323K.

The fault probability for 7N variant is 1.1×10^{-4} , compared to 1.8×10^{-4} for 11N variant and 3.3×10^{-4} for 22N variant. It is evident that fault probability is strongly dependent on the interstitial content. The corresponding change in micro-strain value is lesser in magnitude, but follows the same trend as fault probability. It has been suggested by researchers that the formation of stacking fault needs a critical condition to be satisfied [81], which is related to the forest formation and dislocation clustering [153]. This is also the condition closely associated with DRX nucleation mechanism. Based on this, and the results of Fig. 5.10, it is inferred that faulting and DRX nucleation could be competing mechanisms. In this case, the nucleation of strain-free grains could hinder the formation of faults in the recrystallization domain. This explains why stacking faults have scarcely

been reported in the DRX domain despite the commonly stated association between SFE of a material and its tendency to undergo DRX.

The above factors demonstrate that a material with low SFE (and with higher probability of stacking fault formation) has a higher chance of dislocation clustering compared to a material with high SFE (and with relatively lesser probability of stacking fault formation). This can be mathematically stated as:

$$X_g^{22} > X_g^{11} > X_g^7 \quad (5.8)$$

Consequently, the following condition is valid at equal levels of deformation (temperature, strain, strain rate):

$$X_T^7 + X_t^7 > X_T^{11} + X_t^{11} > X_T^{22} + X_t^{22} \quad (5.9)$$

The higher value of X_g^i at a given temperature signifies that the critical condition can be achieved with a lower value of X_t^i . Consequently, at fixed strain rate, the DRX nucleation occurs at lower strain levels for 22N variant, followed by 11N and 7N, respectively as shown in Fig. 5.4. This equation also indicates that, at a given temperature, the DRX fraction for 22N is more dependent on stored energy which causes nucleation, rather than the time, which favors grain growth. On the other hand, the reverse is true for 7N variant of the alloy.

The sequence of DRX nucleation with variation in interstitial content is in good agreement with the trend of corresponding DRX fraction at a fixed strain rate. However, the variation of critical strain with strain rate is inconsistent with the variation of corresponding DRX fraction for all variants. This clearly demonstrates that the DRX fraction depends on other factors, in addition to how early the nucleation occurs.

These factors include – initial grain size, density of nucleation sites, time available for grain growth and hindrance of this growth due to grain impingement. Since all the variants of steels used here have approximately similar initial grain size, effect of initial

grain size can be neglected for the comparative analysis of DRX. Under strain-controlled deformation, as in this study, the total deformation time is fixed. Therefore, early nucleation, as implied by a low critical strain, allows more time for the propagation of DRX. Early nucleation could be promoted by the availability of favorable nucleating sites, such as dislocation forests near grain boundaries. The probable density of these sites would increase with increase in interstitial content of the alloy due to high dislocation-interstitial interactions. Such an increase in dislocation-interstitial interaction energy as a function of interstitial content has been shown by Yakubtsov et al. [143, 154]. It therefore appears that the number of nucleation sites, like the stacking fault probability, is influenced by interstitial content of the 316LN SS. Therefore, it is reasonable to state that the DRX characteristics, particularly nucleation, largely depend on the SFE of the alloy. From the results, it is seen that, besides the existence of more nucleation sites, nucleation in 22N variant also initiates at the lowest strain levels (Fig.5.4). In view of these observations, it is concluded that nucleation plays the dominant role in DRX of the 22N variant.

The dominance of nucleation decreases with decreasing interstitial content due to reduction in favorable nucleation sites and delayed nucleation. These differences are manifested in the variation of DRX fraction at different strain rates (shown in Fig.5.8). This figure also shows varying sensitivity of DRX fraction to strain rate in the domain $0.1-10 \text{ s}^{-1}$. In this domain, the DRX fraction is practically insensitive to strain rate in 22N variant. On the contrary, in other variants the DRX fraction shows a decrease to a minimum value at 0.1 s^{-1} , followed by a rise with increase in $\dot{\epsilon}$.

The variation of DRX fraction with strain rate has already been discussed by various research groups [129, 130, 135, 155]. Conventionally, the DRX behavior has been separately discussed in low $\dot{\epsilon}$ domain and high $\dot{\epsilon}$ domain. In the low $\dot{\epsilon}$ domain, the

high DRX fraction is attributed to low ε_c and availability of more time (due to low ε'). On the other hand, the high DRX fraction at high ε' is attributed to the adiabatic temperature rise and higher lattice distortion at these conditions. It is apparent that the deformation time has little impact on the DRX process at high ε' . In the framework of Eq. 5.5, the weight assigned to time, i.e. X_t^i , becomes significant only at low strain rates. This can be mathematically expressed using a ‘time threshold’ t_c , below which X_t^i is negligible:

$$X_t^i \approx \begin{cases} 0 & \text{if } t < t_c \\ 0 < c < 1 & \text{if } t > t_c \end{cases} \quad (5.10)$$

In other words, there exists a time threshold, below which nucleation requires assistance from temperature (X_T^i) and stored energy (X_g^i) contributions. These contributions are provided by adiabatic temperature rise and increased dislocation density at high ε' . Therefore, the nucleation process is highly rate sensitive below the time threshold. When $t > t_c$, nucleation is found to be practically rate-insensitive. In the present study, the t_c corresponds to strain rate of 0.1 s^{-1} . Below t_c , i.e. at strain rates 1 s^{-1} and 10 s^{-1} , the role of adiabatic temperature rise becomes more important. Experimental measurements show that adiabatic temperature rise is 10K at 1 s^{-1} and 29K at 10 s^{-1} , respectively. Therefore, the retardation of nucleation due to insufficient time is compensated by adiabatic temperature rise at 10 s^{-1} but not at 1 s^{-1} , resulting in the trend shown in Fig.5.8. This time-dependency dwindles at strain rates $< 0.1 \text{ s}^{-1}$, where adequate time for nucleation eliminates the need for additional thermal energy. As per Eq.5.9, at a given temperature, the time-dependency is also suppressed by higher interstitial content (or lower SFE and higher probability of fault), as more nucleation events can occur simultaneously due to availability of more nucleation sites. This explains the insensitivity of DRX fraction to strain rate in 22N variant in the domain $0.1\text{-}10 \text{ s}^{-1}$.

5.4. Effect of nitrogen content on grain size evolution

DRX being a grain refinement mechanism [131], its complete characterization requires data regarding the grain size variation. In order to analyze the grain size evolution of the latter, the GOS criterion has once again been used to partition DRX grains from deformed grains. Fig.5.11 shows the variation of DRX grain size with nitrogen content. In Fig.5.11a the variation of average DRX grain size is shown at various temperatures at fixed strain rate. From this figure it is clear that the influence of nitrogen content on DRX grain size depends on the temperature. At temperature, 1123K where the DRX nucleation initiates in all the three variants, DRX grains does not show any variation in size with respect to nitrogen content. As the deformation temperature is increased to 1323K the average size of the DRX grains in each variant increased due to initiation of growth. The plot shows that growth process continued with further increase in deformation temperature to 1423K. However, the growth with respect to temperature is found to differ with nitrogen content.

While the grain growth with variation in temperature is found to be minimum in 22N variant, it is found to be maximum in 7N variant. The temperature sensitive grain growth for 11N variant remains between that of 7N and 22N variants. This implies that increase in nitrogen content makes 316LN SS less prone to grain growth after DRX. The reason could be attributed to the more number of DRX nucleation with increase in nitrogen content in the steel. Presence of number grains per unit area increases the chance of impingement of each growing grain with its growing neighbors. As a result, the grain growth is restricted in 316LN containing high amount of nitrogen. Hence grain refinement with increase in nitrogen content is seen when deformed under suitable conditions. Fig. 5.11b shows the variation in average size of DRX grains (with a confidence interval (CI) of 95%) with strain rates at constant temperature in all three

variants of the 316LN SS. [The 95% CI is generally expressed as DRX grain size ± 1.96 SD/ \sqrt{N}]. The In this figure, significant grain refinement with increase in strain rate in the domain $0.001-1 \text{ s}^{-1}$ while grain growth is seen in the strain rate domain $1-10\text{s}^{-1}$.The figure 5.12 shows the grain size evolution with varying nitrogen content at different strain rates at 1323K. The data shown here indicate that with increase in deformation strain rate, average DRX grain size in each variant becomes smaller. However, this phenomenon remains apparent upto a particular strain rate, beyond which the DRX grains again start to grow as shown in Fig. 5.12. The growth at higher strain rates occur due to adiabatic temperature rise. The strain rate upto which the grain refinement occurs with increase in strain rate, and the grain growth that occurs at higher strain rate are found to be random and do not hold any relationship with nitrogen content. It completely depends on the adiabatic temperature rise, which is unique to each test.

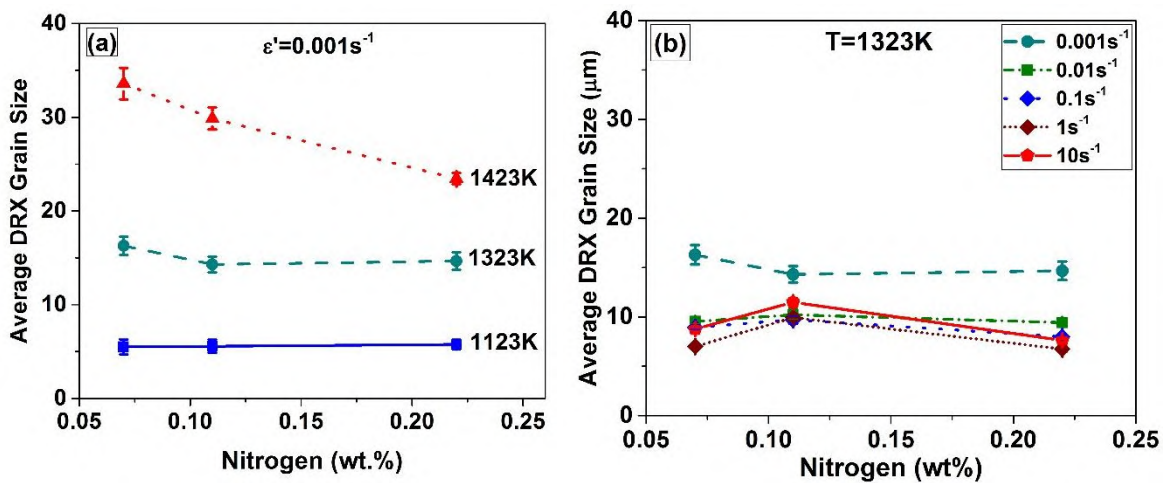


Figure 5.11: Variation of average DRX grain size with nitrogen (a) at various temperatures at 0.001s^{-1} (b) at various strain rate at 1323K with a confidence interval of 95%.

5.5. Influence of nitrogen on special boundaries

Another important feature of microstructural evolution during hot deformation of austenitic stainless steel is twin boundaries. Fig.5.13 shows that the deformation

temperature and nitrogen content of the steel affect occurrence of twins. In literature on the subject, $\Sigma 3$ boundaries have been considered as primary twins [156].

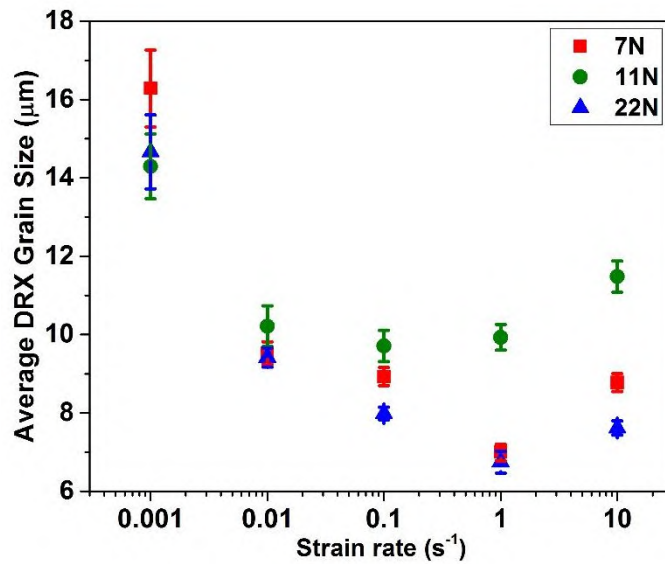


Figure 5.12: Variation of average DRX grain size with strain rate at 1323K (with a confidence interval of 95%).

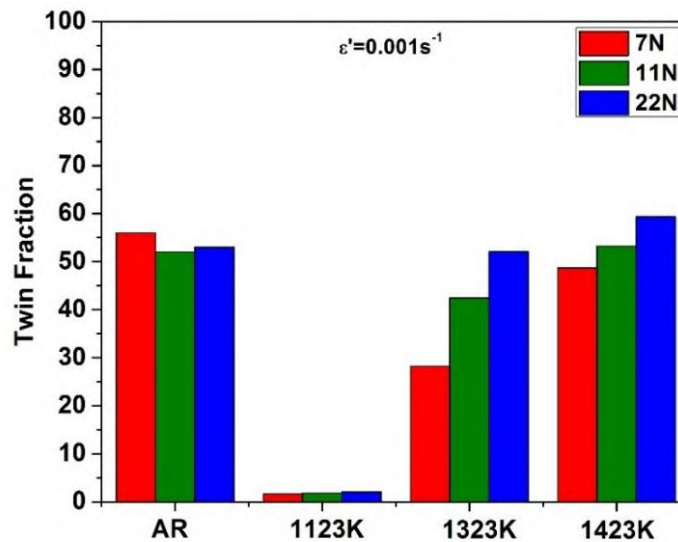


Figure 5.13: Twin Boundary frequency of 7N, 11N and 22N steels at 0.001s^{-1} .

In the as-received microstructure, the fraction of $\Sigma 3$ boundaries were 56%, 52%, 53% for 7N, 11N and 22N variants, respectively. However, frequency of these boundaries

reduced significantly when the material was deformed at 1123K. In the microstructure obtained after deformation at 1123K, the fraction of $\Sigma 3$ boundaries were 1.6%, 1.8%, 2.1% for 7N, 11N and 22N variants, respectively. This indicates that the original $\Sigma 3$ boundaries present in the as received microstructure were destroyed. This happens due to migration of boundaries during deformation. From the Fig. 5.13, it is seen that, with increase in deformation temperature from 1123K to 1223K, frequency of these twins increases. This is an evidence of formation of new twins with progress of DRX.

During, recrystallization, twinning can occur in a material, through interaction of $\Sigma 3$ boundaries that leads to formation of higher order CSL boundaries such as $\Sigma 9$ and $\Sigma 27$ [157] and/or through accidents during grain boundary migration [158]. At 1423K, the thermal energy supplied to the material is primarily utilized for grain growth. However, the growth is also restricted by the similar growth of the neighboring grains. As a result, the energy supplied to the material is stored in the grains. This energy is minimized through the formation of the twins; the mechanism is referred to as “twin formation through growth accident [159]. In the present case, since the frequency of $\Sigma 9$ and $\Sigma 27$ is negligible, the formation of twins can be attributed to the growth accidents. The influence of nitrogen on formation the twin boundaries have already been reported by Guo et al. [31]. The current study agrees well with Guo et al. [31] that enhancement in nitrogen increases the frequency of twin boundaries. It has been reported that stacking fault energy (γ_{SFE}) has a strong correlation with the formation of twins in the material [160]. It is well known that being an interstitial element, nitrogen strongly influences the stacking fault energy of the material [143]. This signifies the propensity for twin boundary formation in the material.

5.6. Conclusions

The findings from this chapter can be summarized as:

- Enhancement of nitrogen in 316LN SS intensifies work hardening in the material. Critical strain for the DRX nucleation is achieved early with enhancement in nitrogen in the steel.
- With increasing total interstitial (here N+C) content, SFE reduces and the probability of forming stacking faults increases in the Fe-Cr-Ni-Mo system. Since the stacking fault probability increases, the sites for dislocation forest formation increase during deformation. This is manifested as higher micro-strain in the variants having higher interstitial content. As a result, in these variants, DRX initiation occurs at lower strain levels.
- The variation of critical strain with strain rate does not correspond to the overall DRX fraction in any variant. This indicates the importance of time and temperature, in addition to the accumulation of stored energy in controlling the DRX fraction in the alloy. Because of this dependency, some variants show sluggish DRX behavior at strain rate around 1s^{-1} .
- The degree of dependency of DRX fraction on time, however, varies with interstitial content, and is highest in the alloy with lowest interstitial content. As the interstitial content increases in the alloy, the DRX fraction practically becomes rate-independent.
- More number of nitrogen atoms in the material enhances the probability of formation of more dislocation cells which serve as active sites for nucleation. As a result, number of DRX grains accordingly increases with enhancement in nitrogen in the steels.

- The increase in nitrogen content makes 316LN SS less prone to grain growth after DRX. The reason could be attributed to the more number of DRX nucleation with increase in nitrogen content in the steel.
- Higher Nitrogen increases the propensity for twin boundary formation in the 316LN SS.

Effect of nitrogen content on workability of 316LN SS

6.0. Preamble

In this chapter, workability of 316LN SS with respect to temperature and strain rate are studied with the aid of Dynamic Materials Model (DMM). To understand the influence of nitrogen content and strain on workability of 316LN SS deformation maps are developed by presenting the efficiency parameter and instability parameter in two dimensional temperature-nitrogen content and strain-nitrogen content spaces. These deformation maps are discussed in the context of suitability of different variants for different hot deformation processes.

6.1. Processing Maps

Intrinsic workability of materials are often studied by using dynamic material model (DMM) [85, 161-163]. The dynamic material modelling is the combination of Ziegler's [164] concept of the continuum mechanics for large plastic flow, Wellstead's [165] principles for physical systems modelling and Prigogine's [166] concept of the irreversible thermodynamics. According to Wellstead's [165] principles, the power dissipated (P) by the work piece could be partitioned into two complementary parts called power content (G) and power co-content (J) [167].

$$P = \sigma \cdot \dot{\varepsilon} = G + J = \int_0^{\dot{\varepsilon}'} \sigma d\dot{\varepsilon}' + \int_0^{\sigma} \dot{\varepsilon}' d\sigma \quad (6.1)$$

where σ flow is stress and $\dot{\varepsilon}'$ is strain rate. G describes the power dissipated which is converted to heat during plastic deformation and J is the fraction of power dissipated by

metallurgical phenomena [168]. For DMM, the flow stress (σ), at constant temperature and strain is described by the following constitutive equation

$$\sigma = K' \varepsilon'^m \quad (6.2)$$

where K' is a constant and m is the strain rate sensitivity of the material. The 'm' can be determined as follows

$$m = \frac{\partial(\ln \sigma)}{\partial(\ln \varepsilon')} \approx \frac{\varepsilon' \sigma d(\ln \sigma)}{\sigma \varepsilon' d(\ln \varepsilon')} = \frac{\varepsilon' d\sigma}{\sigma d\varepsilon'} = \frac{dJ}{dG} \quad (6.3)$$

From Eq. 6.1, the J content is given as

$$J = \int_0^{\sigma} \varepsilon' d\sigma = \frac{\sigma \varepsilon' m}{m+1} \quad (6.4)$$

From the above equation, the J is a dependent factor on m at constant input power ($\sigma \varepsilon'$). The maximum value of J can be obtained when m is unity and is given by

$$J_{\max} = \frac{\sigma \varepsilon'}{2} \quad (6.5)$$

Then the power dissipation efficiency (η) can be defined as

$$\eta = J/J_{\max} = 2m/(m+1) \quad (6.6)$$

where η is a dimensionless parameter is used indicated the power dissipation at a particular condition.

As per DMM, the flow instability in the material is identified on the basis of another parameter called as the flow instability parameter and it is expressed as

$$\xi(\varepsilon') = \frac{\partial \ln[m/(m+1)]}{\partial \ln \varepsilon'} + m \quad (6.7)$$

The instability parameter $\xi(\dot{\epsilon})$ is plotted as a function of temperature and strain rate which results in map called as instability map. When $\xi(\dot{\epsilon})$ assumes a negative value, the flow becomes unstable. This negative value of $\xi(\dot{\epsilon})$ indicates that system is not able to generate entropy at a rate that is equivalent with the imposed rate. The $\xi(\dot{\epsilon})=0$ delineates the boundary between stable and unstable flow behavior. Both η and $\xi(\dot{\epsilon})$ are calculated using the experimental data obtained from the compression testing. The flow stress at finer intervals of temperature and strain rate is obtained by using a shape preserving polynomial called Piecewise Cubic Hermite Interpolating Polynomial (PCHIP) [115, 169]. Efficiency contours are usually plotted in strain rate and temperature space to generate efficiency map for a material. Similarly, $\xi(\dot{\epsilon})$ is plotted in the strain rate and temperature frame to generate instability map. The instability map is super imposed on the efficiency map to obtain a map called processing map. This map is used to study the workability of a material. The domains of the processing maps are validated using the microstructure obtained from the specimens tested in the concerned domain. Fig.6.1, Fig. 6.2 and Fig. 6.3 shows the microstructurally validated processing maps for the variants 7N, 11N and 22N, respectively. The colored region indicates the stable domain whereas the white region indicates the domain of flow instability in the material. From these figures it can be seen that 316LN shows two unstable domains; one occurs at high strain rate domain and the other occurs at low strain rate domains at 1123-1273K. In the instability domain that occurs at high strain rate domain ($1-10s^{-1}$), 316LN SS shows negative strain rate sensitivity and micro structurally the domain is characterized by intense shear bands. On the other hand, in the instability domain that formed at low strain rate domain ($0.1-0.01s^{-1}$ at 1123-1273K), 316LN SS mostly showed positive strain rate sensitivity, however, the microstructure shows the signature of flow localization amidst the heavily deformed grains which is indicated by the arrows in the Figs. 6.1-6.3.

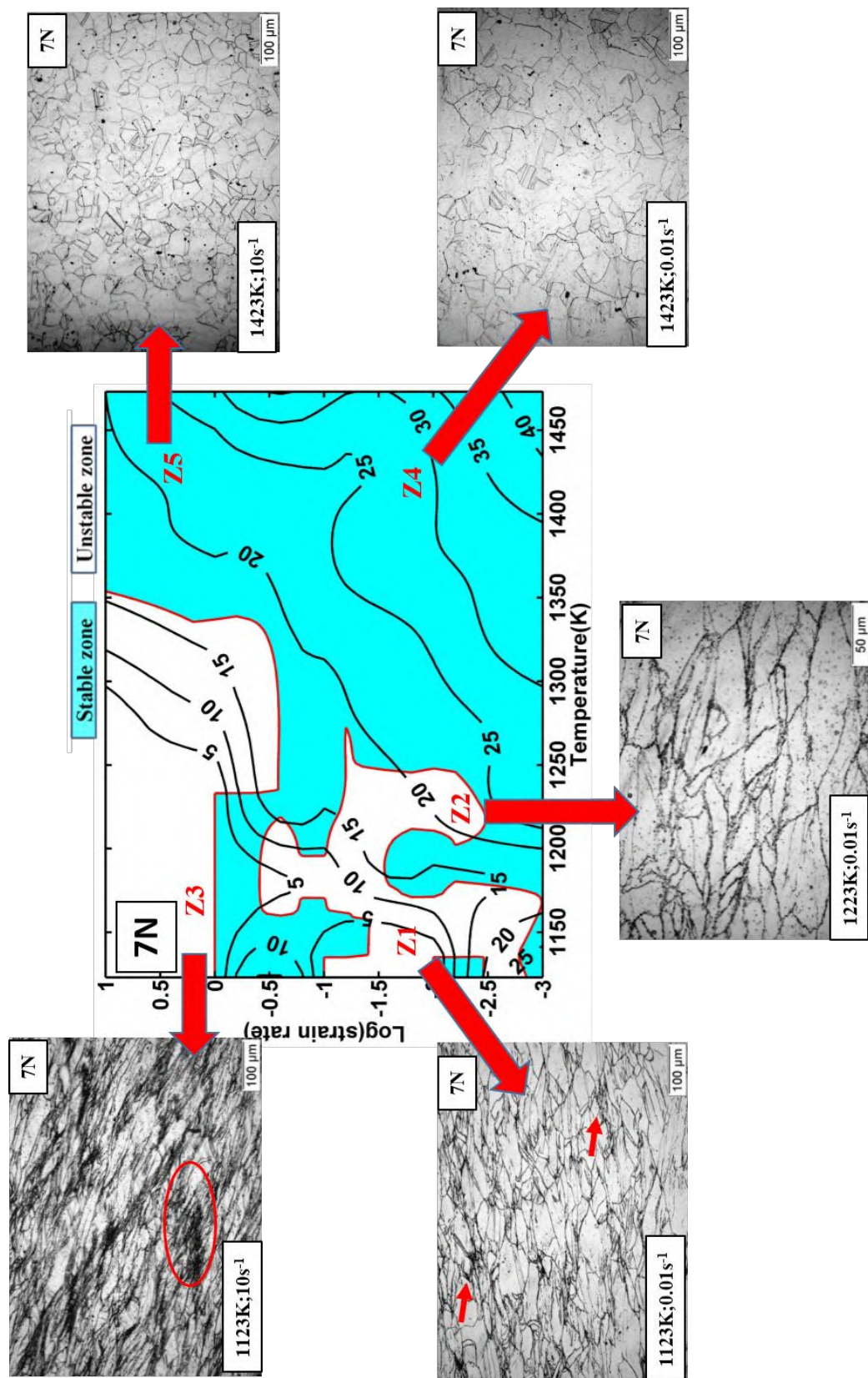


Figure 6.1: Processing maps of 7N at various temperature and strain rates at a true strain of 0.65. The marked region indicates the region of flow localization and shear bands.

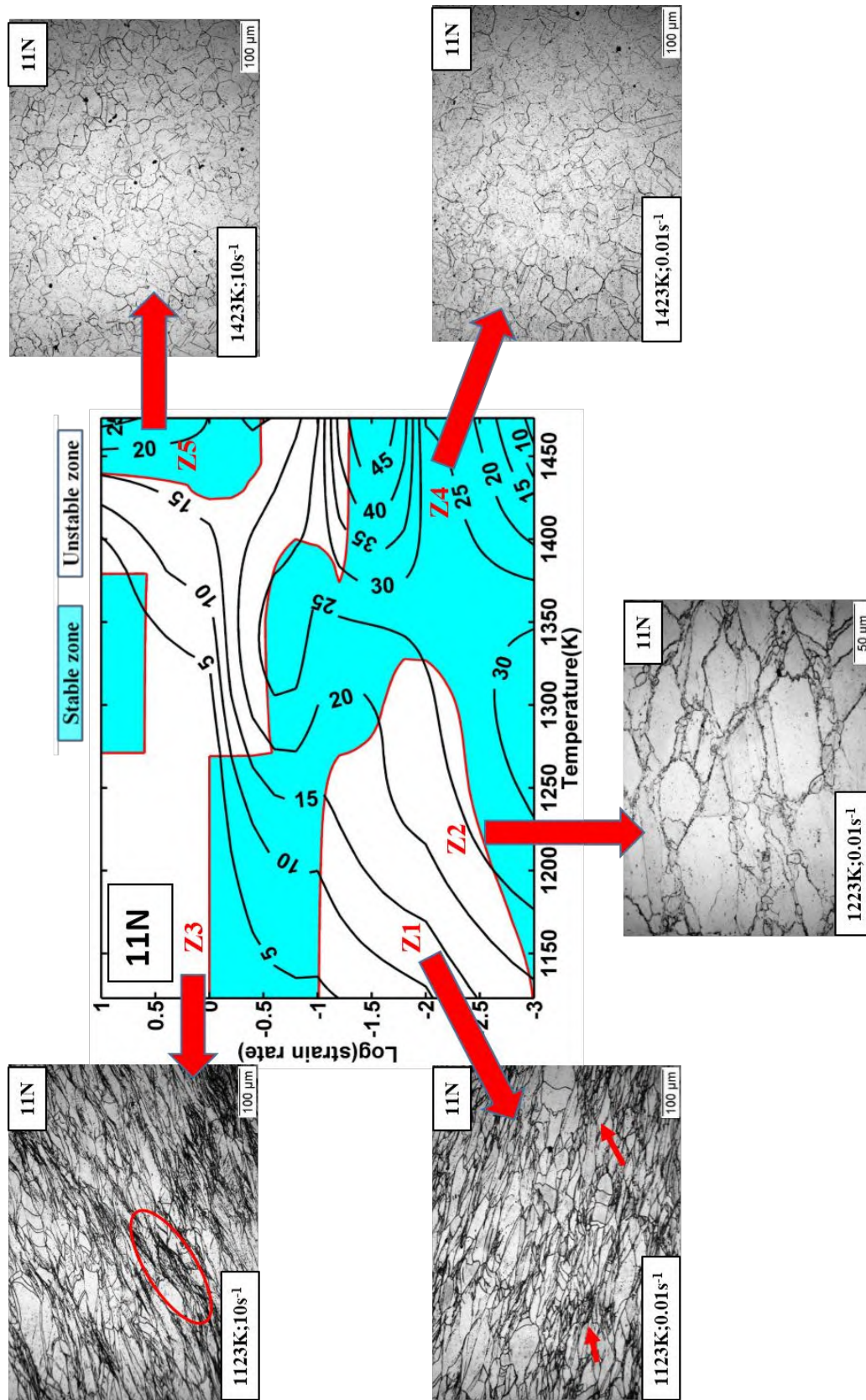


Figure 6.2: Processing maps of 11N at various temperature and strain rates at a true strain of 0.65. The marked region indicates the region of flow localization and shear bands.

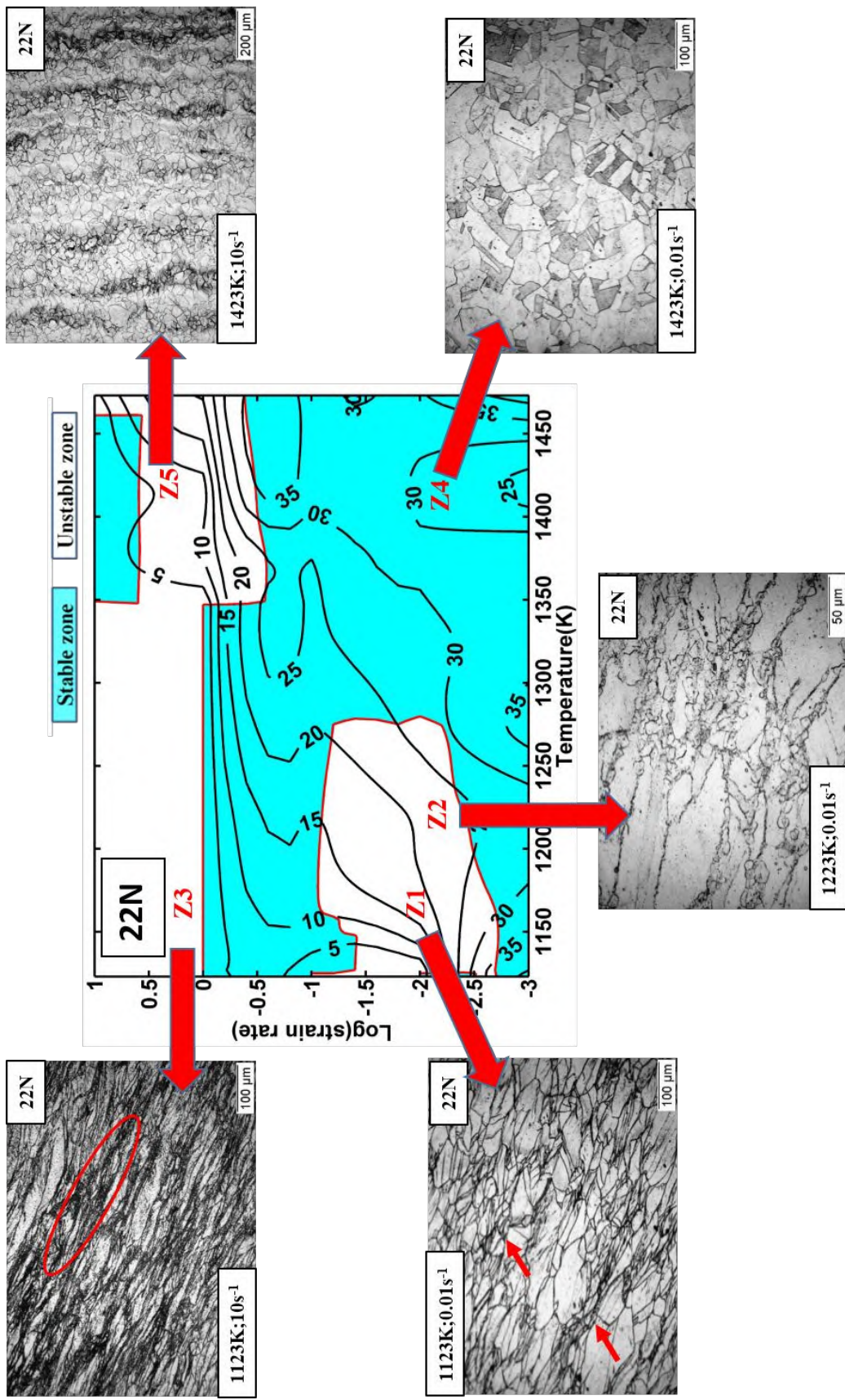


Figure 6.3: Processing maps of 22N at various temperature and strain rates at a true strain of 0.65. The marked region indicates the region of flow localization and shear bands.

The stable domain in all variants is characterized by the recrystallized equiaxed grains without any microstructural defects. The maximum efficiency of power dissipation remained around 30-45% among the variants and does not show any clear trend with the variation of nitrogen content. However, expansion of unstable domains and shift in stable domain of high efficiency were observed with variation in nitrogen content in 316LN SS.

6.2. Nitrogen content and workability domain

It is well known that the reduction ratio is an important aspect in industrial metal forming. The characterization of workability remains incomplete without understanding the effect of strain on workability. Typical processing map does not give the complete view of workability as it does not consider the effect of strain directly. Besides, it is seen from the Figs. 6.1-6.3 that nitrogen affects the workability domain.

To analyze the effect of nitrogen content on the workability with respect to strain and temperature, the efficiency and instability parameters were plotted using different two-dimensional spaces such as temperature-nitrogen content and strain-nitrogen content. These maps are not the typical processing maps and therefore, hereafter called workability maps. Fig. 6.4 shows the workability maps that shows variation of workability of 316LN SS when nitrogen content and deformation temperatures are changed at a specified strain level at different strain rates. From this figure, it can be interpreted that at 0.001s^{-1} , 316LN SS shows stable flow behavior irrespective of its nitrogen content. However, with increase in nitrogen content the value of efficiency parameter increased especially upto deformation temperature of 1323K. The reason of this high efficiency could be attributed to the tendency of high nitrogen containing variants to undergo early DRX nucleation and the propensity to form more nucleation

sites during high temperature deformation. Above 1323K, which is mostly grain growth domain, the efficiency parameter does not vary with the nitrogen content.

As the strain rate is increased to 0.01 s^{-1} , an unstable domain is appeared in the temperature range 1173-1323K. With further increase in deformation rate, this unstable domain gradually expands and stable domain simultaneously shifts to higher temperature range. Besides, it is observed that the at higher strain rates, the efficiency of the stable domain gradually decreases with increases in nitrogen content.

From these observations it can be concluded that the 7N variant of 316LN SS is suitable for high speed metal forming process such as forging rolling and extrusion, particularly at temperature above 1373K. Whereas 22N variants is not suitable for such processes, when particularly deformed upto 0.65 true strain in single deformation step. This clarifies the effect of temperature, strain rate and nitrogen content on the workability. As discussed earlier, the strain is also an important factor on deciding the workability on the material and the effect of strain has to be understood to characterize the workability of the material completely.

To understand the effect of strain, in this study high strain rates particularly 1 s^{-1} and 10 s^{-1} have been selected as it can be seen from Table.2.1 of Chapter 2 that majority of the deformation processes employ high strain rate and the current analysis shows 316LN SS shows a gradual transition from stable to unstable domain with increase in nitrogen content at high strain rates. Since this transition occurs at high temperatures (Fig. 6.4 (c-d)), 1423K is chosen as the deformation temperature for such analysis. The deformation maps given in Fig.6.5 show the variation of efficiency parameter and demarcation between stable and unstable processing domain in two dimensional strain- nitrogen content spaces. Fig. 6.5a indicates that at 1 s^{-1} , both 7N and 11N variants remain stable upto true strain level of 0.65. 22N remains stable only upto true strain level of 0.5.

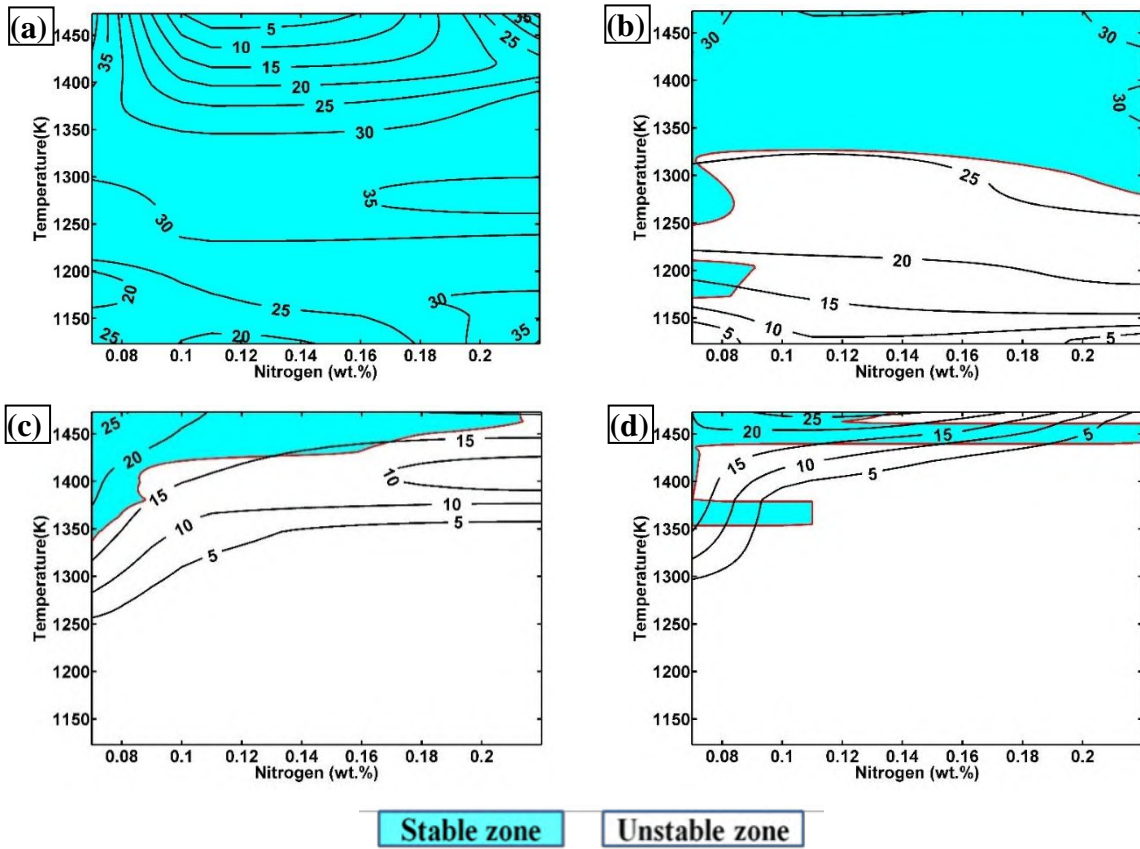


Figure 6.4: Processing maps of 316LN SS at various temperature and nitrogen content at (a) $0.001s^{-1}$, (a) $0.01s^{-1}$, (c) $1s^{-1}$ and (d) $10s^{-1}$ at a true strain of 0.65.

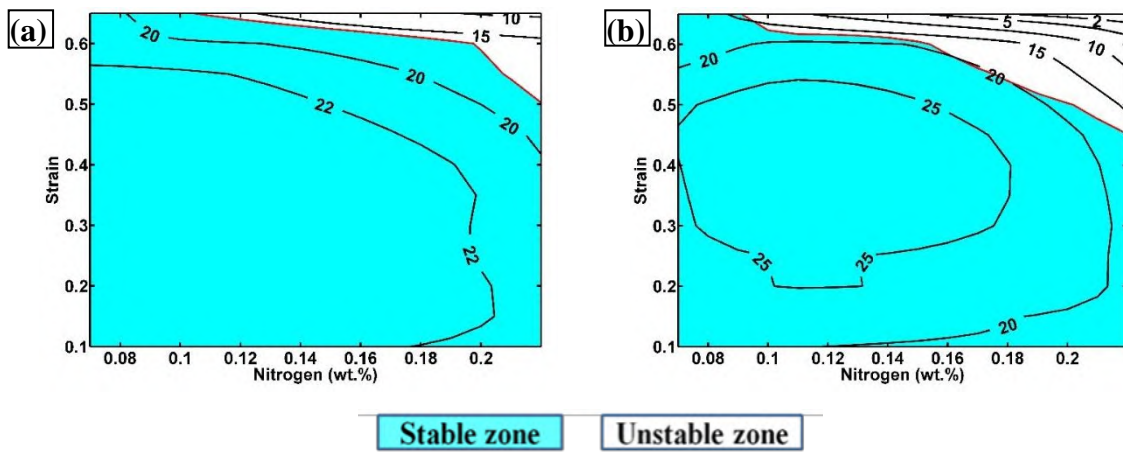


Figure 6.5: Processing maps of 316LN SS at various strain and nitrogen content at (a) $1s^{-1}$ and (b) $10s^{-1}$ at temperature 1423K.

As the strain rate increases from 1s^{-1} to 10s^{-1} , the maximum true strain level upto which the 11N and 22N variants can be deformed decreases from 0.65 to 0.5 and 0.5 to 0.45, respectively. The current results indicate that both 11N and 22N variants in their present condition may not be suitable for high speed extrusion process where material undergo high strain levels during deformation. However, these variants of 316LN SS such as 11N and 22N can be safely used for forgings where low reduction ratio is achieved in one step.

6.3. Conclusions

On the basis of the results and discussion presented in the chapter the following conclusions are made.

- 316LN shows two unstable domains; one occurs at high strain rate ($1-10\text{s}^{-1}$) domain and the other occurs at low strain rate domains ($0.01-0.1\text{s}^{-1}$ at 1123-1273K).
- In the instability domain that occurs at high strain rate 316LN SS shows negative strain rate sensitivity and micro structurally the domain is characterized by intense shear bands. The instability domain that formed at $0.01-0.1\text{s}^{-1}$ at 1123-1273K, 316LN SS mostly showed positive strain rate sensitivity, however, the microstructure shows the signature of flow localization amidst the heavily deformed grains.
- At 0.001s^{-1} , 316LN SS shows stable flow behavior irrespective of its nitrogen content. With increase in nitrogen content the efficiency of power dissipation increased especially upto deformation temperature of 1323K. This behavior is attributed to the tendency of high nitrogen containing variants to undergo early

DRX nucleation and the propensity to form more nucleation sites during high temperature deformation.

- At higher strain rates, the efficiency of the stable domain gradually decreases with increases in nitrogen content in 316LN SS.
- 7N variant is suitable for majority of high temperature deformation processes such as rolling, forging and extrusion which are carried out at high speed.
- 11N and 22N variants in their present condition are not suitable for high speed extrusion process where material undergo high strain levels during deformation.

However, these variants of 316LN SS such as 11N and 22N can be safely used for forgings where low reduction ratio is achieved in one step.

Chapter 7

Flow instabilities in 316LN austenitic stainless steel at high strain rate

7.0. Preamble

This chapter presents the details about the flow instabilities of 316LN SS. It focuses on the formation of shear bands that occur during deformation at high strain rates ($1-10s^{-1}$). The mechanisms of initiation and propagation are discussed on the basis of results obtained from micro structural investigation.

7.1. Instability at high strain rates: Adiabatic Shear banding (ASB)

At high strain rates ($1-10s^{-1}$) adiabatic shear banding (ASB) is common form of instability observed in many materials. ASB can be distinguished from homogeneously deformed microstructures as this region shows intense localized deformation. The ASB separates dead metal zone from the deformed zone. In general, two bands are initiated simultaneously as shown in Fig. 7.1a, and these two combine to form an X-shaped structure. However, in certain cases, with increase in strain only one band becomes more intense compared to the other. This is indicative of shearing only in one direction. A representative confocal image of specimen with single band is shown in Fig. 7.1b. During the experiments carried out for the present work only single sided intense bands were observed in the specimens which were deformed in the unstable domain that occurred at higher strain rates (Chapter-3). The intensity of the bands found to vary with deformation temperature, strain rate and nitrogen content of 316LN SS.

7.1.1. Critical strain for formation of adiabatic shear bands

A criterion was developed by Jonas et al. [170] to study the tendency of a material to form flow localization during hot isothermal compression test. A theory was developed to predict the unstable flow behavior during bulging and it was further extended to occurrence of shear banding. As per the theories the condition for flow localization during compression testing is expressed as [171]:

$$\frac{1}{\varepsilon'} \frac{d\varepsilon'}{d\varepsilon} = -\frac{\gamma'}{m} = \alpha' \geq 5 \quad (7.1)$$

where γ' is the non-dimensional work hardening rate given by:

$$\gamma' = \left(\frac{1}{\sigma} \frac{d\sigma}{d\varepsilon} \right)_{\varepsilon'} \quad (7.2)$$

and m is the strain rate sensitivity parameter

$$m = \left(\frac{\partial \ln \sigma}{\partial \ln \varepsilon'} \right)_{T, \varepsilon} \quad (7.3)$$

It is to be noted that the flow localization parameter (α') is dependent on rate of work hardening (γ) and strain rate sensitivity parameter (m). The critical balance between higher work hardening and strain rate sensitivity is needed to avoid instabilities in the material. The material becomes more prone to flow localization when it exhibits higher work hardening and lower strain rate sensitivity. For the present study, the criterion given in Eq.7.1 is considered to identify the critical strain for shear band formation (ε_{ASB}). The strain at which the value of α exceeds 5 is termed as critical strain for shear band formation (ε_{ASB}). Since, shear bands are noticed mostly at high strain rate domains 1-10 s⁻¹. For further detailed analysis, the investigation mostly focuses only on the specimens

deformed at 10 s^{-1} . The ϵ_{ASB} contours at 10s^{-1} for various combinations of nitrogen content and temperature is shown in Fig. 7.2.

It has been found that ϵ_{ASB} increases with increasing temperatures. The trend remained consistent for all the variants. Besides it is found that with increase in nitrogen content, the critical strain required for formation of adiabatic shear band gradually decreases, especially at low temperature domain. The formation of shear bands at high strain rate is attributed to the adiabatic condition created due to lack of time for heat dissipation which generated during deformation. Besides the time, conductivity of the material influences the heat dissipation to a large extent as the heat has to be conducted from the core of the specimen to surface. To analyze the influence of thermal conductivity, the thermal conductivity are calculated using JMATPRO 7.0 for different variants. The variation of thermal conductivity with temperature is shown in Table.7.1.

Table 7.1: Thermal conductivity values (W/mK) for 7N, 11N and 22N at various temperatures calculated from JMATPRO 7.0.

Temperature(K)	7N	11N	22N
1123	24.72	24.71	24.67
1173	25.39	25.38	25.34
1223	26.06	26.05	26.01
1273	26.73	26.72	26.68
1323	27.39	27.38	27.35
1373	28.06	28.05	28.02
1423	28.73	28.72	28.69
1473	29.40	29.39	29.36

It can be seen from the table that with increase in temperature, thermal conductivity increases and with increase in nitrogen content it gradually decreases. These data indicates that heat dissipation becomes poor in a specimen of 316LN SS when deformation

temperature is decreased or nitrogen content in the steel is increased. This causes high adiabatic temperature rise at low deformation temperature leading to formation of shear bands. For further analysis adiabatic temperature rise measured for 7N variant and 22N variant at different deformation temperature is shown in Fig. 7.3. From this figure, it can be seen that with increase in temperature, adiabatic temperature rise gradually decreased for both the variants. The temperature (ΔT) rise calculated by using modeled given in Eq. 7.4 [107] also found to be in good agreement with the measured data.

$$\Delta T = \frac{\beta_{ASB}}{\rho_{steel} C_p} \int_{\epsilon_o}^{\epsilon_f} \sigma d\epsilon \quad (7.4)$$

where C_p is the specific heat, ρ_{steel} is the density of steel (7.99g/cm^3) and β_{ASB} is the fraction of plastic work converted to heat and it is generally taken as 0.9 at high strain rates.

On the basis of the above results, it can be concluded that the specimens deformed at low temperature, become more susceptible to band formation as adiabatic temperature rise is higher at lower deformation temperature and thermal conductivity of the material is relatively poor at lower temperature compared to that is seen at higher temperatures.

From, the experimental data, it is also observed that the probability of occurrence of adiabatic shear band increased only when the adiabatic temperature rise is above 30 K. For the deformation conditions, where temperature rise is well below 20 K, the material shows uniform deformation without any visible signature of localized deformation in the microstructure. When the adiabatic temperature rise is in between 20-30 K, the probability of band formation reduced. In this transition domain (Fig. 7.3), deformed specimens occasionally showed the presence of some discrete bands with equiaxed DRX grains. In low temperature domain, the trapped heat is partly utilized for DRX phenomena in the band. On the other hand, little or no DRX occurs in the surrounding regions,

leading to deformed grains outside the band. Most of the heat generated is accumulated inside the band than its surrounding. This causes lower ΔT value at higher deformation temperatures, which is favorable for the formation of DRX process on both inside and outside the bands region.

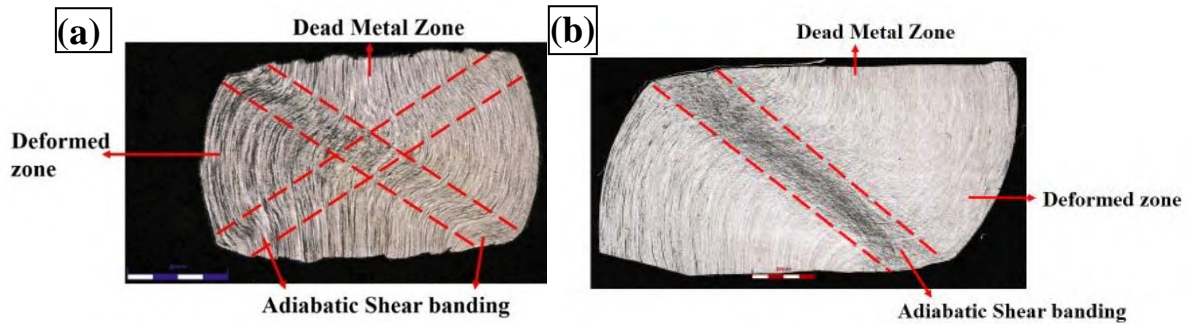


Figure 7.1: Confocal micrograph of cross section view of compressed sample (a) X shaped banding (b) heavily densified banding in one direction.

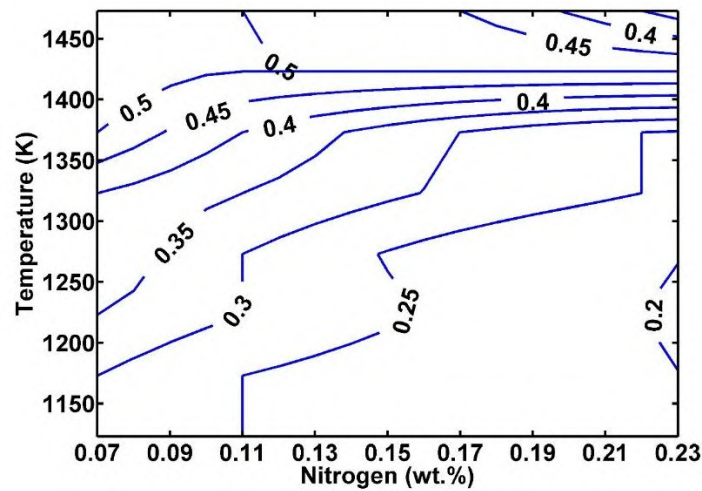


Figure 7.2: Variation of ϵ_{ASB} at different temperature with increasing nitrogen content.

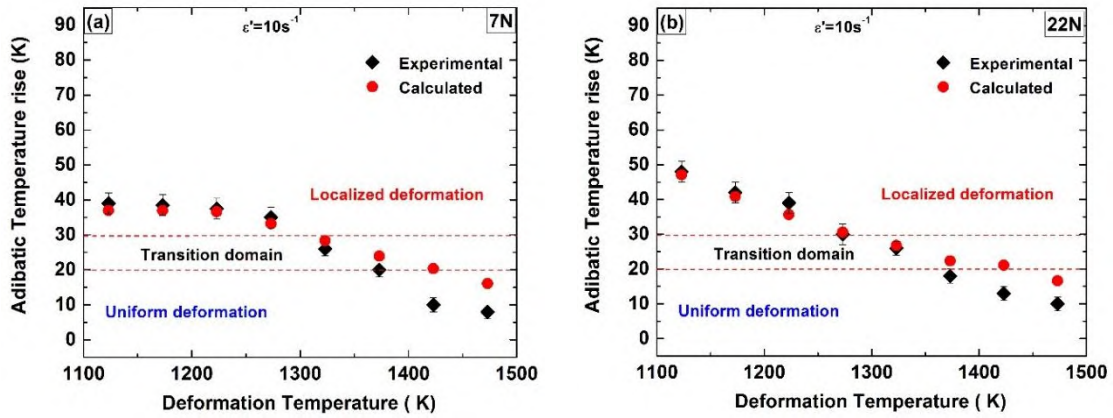


Figure. 7.3: Experimentally measured and calculated values of adiabatic temperature rise during deformation at different temperature for (a) 7N and (b) 22N at $10s^{-1}$.

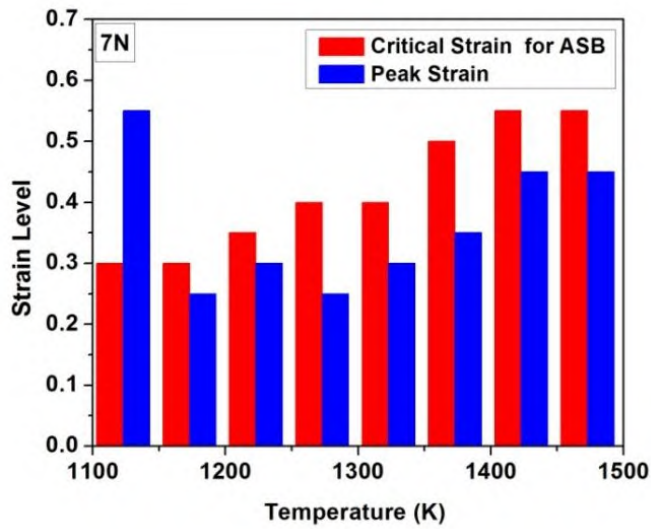


Fig. 7.4. Relationship between peak strain(ϵ_p) and ϵ_{ASB} in 7N grade at various temperature.

To analyze the correlation between ASB formation and DRX in 316LN, peak strain ϵ_p (the strain at which peak stress is achieved) and ϵ_{ASB} are compared at $10s^{-1}$ for 7N variant in the Fig. 7.4. At all temperatures except 1123K, it is found that $\epsilon_p > \epsilon_{ASB}$. This implies that the ASB forms after peak stress is reached. It is well known that the critical strain for DRX is well below the peak stress [68]. This indicates that the dynamic

recrystallization initiates before the ASB formation [172]. It has been reported that shear bands formed during hot working of austenitic steels can be classified as two types: deformed bands and DRX bands [104]. At 1123K, $\epsilon_{ASB} < \epsilon_p$, the ASB formed before peak strain is reached and may be termed as deformation band and at high temperatures where DRX was prominent can be termed as DRX bands.

7.2. Intensity of the adiabatic shear band

It has been seen from the previous sections that at high strain rates and high temperatures materials become more prone to formation of shear bands. However, when at certain conditions the band remains intense; at other conditions its presence is not distinguishable. The intensity therefore becomes a criterion to reject the product or to consider it for further corrective thermo-mechanical processing. The intensity discussed here may be defined as the contrast between the microstructure observed inside the band and outside the band.

Microstructures in ASBs are found to vary with deformation parameters such as temperature, strain rate, deformation geometry and composition (i.e. variation in nitrogen content). The following sections discuss the effect of the aforementioned factors on microstructure in ASBs.

7.2.1. Microstructural changes as a function of temperature in ASB

Deformation temperature has a strong significant influence on band formation and propagation. In interest of clarity, the results presented in this section are restricted to 7N grade steel at different temperatures with the common strain rate of $10s^{-1}$. Fig. 7.5 shows the microstructural variation in the shear band zone at $10s^{-1}$. It can be observed that the adiabatic shear banding is more prominent at lower temperature. Fig. 7.5a shows the ASB

formation at 1123K. This zone is found to heavily deformed and highly localized as indicated by boxes in Fig. 7.5a. At 1223K, formation of new recrystallized grains is observed. They are a few elongated parent grain found, but the majority of grains are fine and equiaxed. As temperature is further increased, the grains inside these bands get fully recrystallized and grain growth occurs at 1323K and 1423K. Twins are also observed at 1423K temperature. However, micro structurally no signature of flow localization observed at 1323K and 1423K. Even though the deformation condition 1323K at $10s^{-1}$ falls at the boundary between the stable and unstable domain as per the processing map Fig. 6.1. No signature of flow localization at this condition can be attributed either to very preliminary stage of initiation of shear band where strain is not sufficient enough for the manifestation of shear band or to the dominance of DRX process over the work hardening.

Fig. 7.6 shows the EBSD maps at 1123K and 1323K. Colors in the maps indicate different crystal orientations. Inverse pole figure (IPF) coloring is used in all maps, according to the color legend attached in Fig. 7.6a. At the low temperature of 1123K, negligible recrystallization has occurred, as evident from the deformed grains shown in Fig. 7.6a. The extent of localized deformation and strain accumulation is studied using intergranular misorientation maps. These maps are colored according to the differences in misorientation between different points inside a grain. High intergranular misorientation values signify several different orientations within a grain, indicating heavy, heterogeneous deformation. Fig. 7.6b shows the intergranular misorientation map corresponding to Fig. 7.6a.

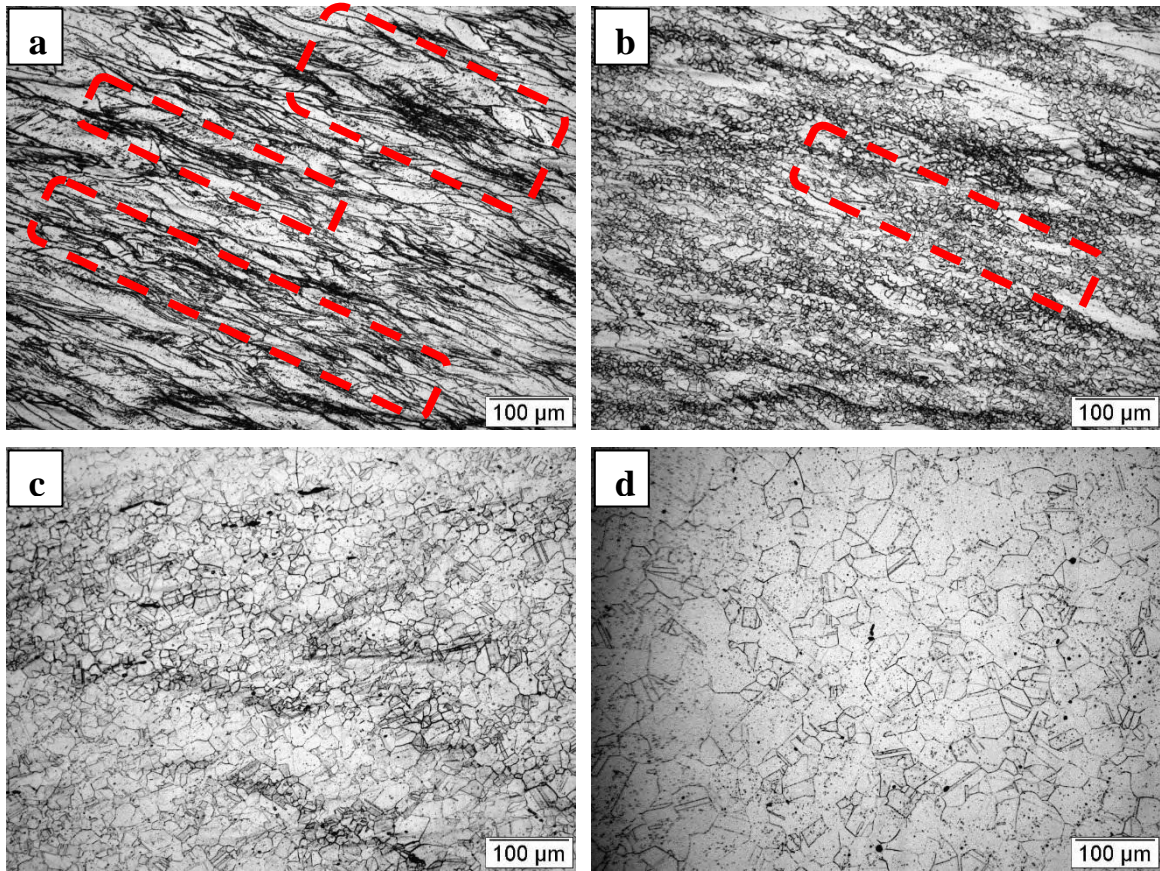


Figure 7.5: Optical microstructures of 7N at $10s^{-1}$ (a) 1123K (the box indicates heavily deformed and highly localized region); (b) 1223K (the box shows the fine nucleation) (c) 1323K and (d) 1423K.

Several areas with high misorientation (above 15°) are seen in Fig. 7.6b, suggesting a higher dislocation density in these areas as compared to their surroundings. However, ΔT value (at 1123K deformation temperature) is as high as 40K, providing adequate thermal energy for smooth material flow in localized bands. The location of these ASBs is non-uniform, as indicated by arrows in Fig.7.6c. It may be noted that the intergranular misorientation inside the marked ASBs is low ($<5^{\circ}$). This is attributed to DRX occurring locally inside the band. As deformation temperature is increased from 1173K to 1323K, the material gets sufficient activation energy for DRX nucleation. This is evident from the IPF map shown in Fig. 7.6c. Fine and equiaxed grains distributed

uniformly across the micrograph are visible in Fig. 7.6c. The corresponding intergranular misorientation map shown in Fig. 7.6d indicates low misorientations across all grains, suggesting extensive occurrence of DRX. From temperature range 1373K-1473K, the ASB formation is delayed as the temperature is reasonably uniform during deformation ($\Delta T < 10^\circ\text{C}$ in all cases) in the steels. The critical strain calculation also confirms the delay in ASB formation. This is majorly due to the high thermal conductivity at higher temperature, which causes simultaneous formation and diffusion of the ASB region. As a result, recrystallized grains are observed throughout the sample and no shear bands are observed.

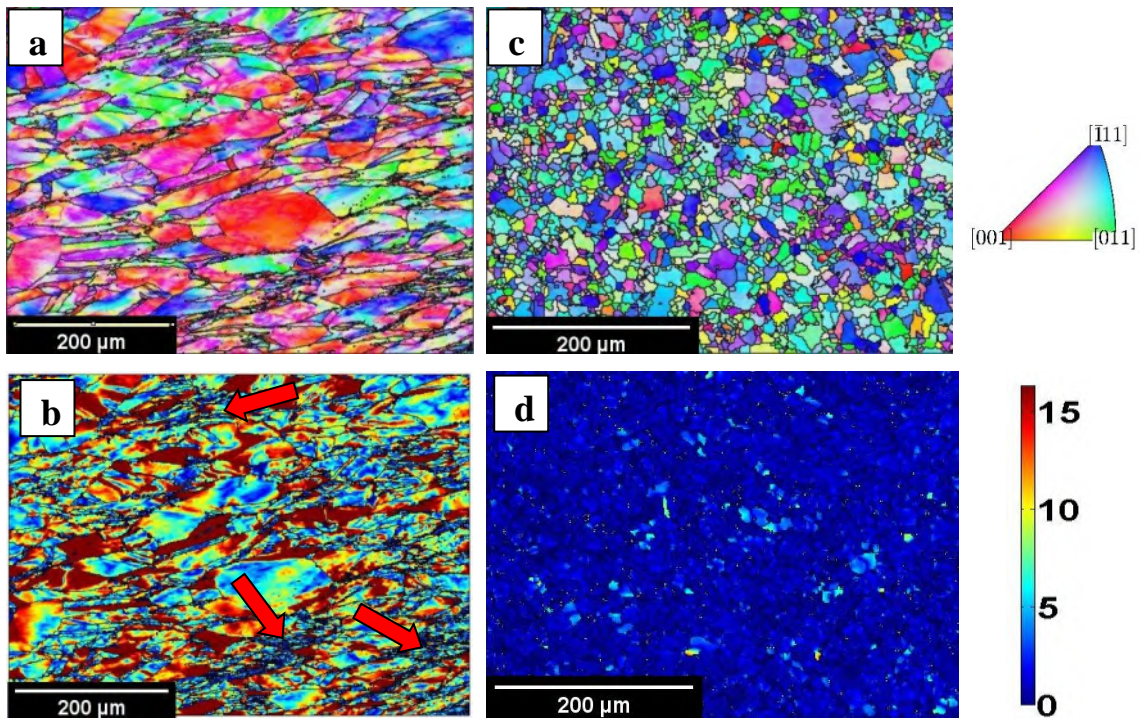


Figure 7.6 : Microstructure of 7N grade steel at 10s^{-1} , taken at temperature : (a) 1123K, IPF map (b) 1123K, intragranular misorientation map, (c) 1323K, IPF map, (d) 1323K, intragranular misorientation map.

7.2.2. Effect of strain rate on microstructures inside ASBs

Having established that the shear banding is more prominent at lower temperatures, the effect of strain rate is studied in this domain. Figs. 7.7(a-c) show the microstructure in ASB zone at 1123K at 0.001, 0.1 and 10s^{-1} strain rate respectively. At low strain rate of 0.001s^{-1} , heavily deformed and elongated grain structures are found. As strain rate is increased to 0.1s^{-1} small pockets of strain localization are observed along with deformed grains. One such pocket is circled in Fig. 7.7b. However at highest strain rate of 10s^{-1} , ASB formation is complete and distinctly visible, as marked in Fig. 7.7c.

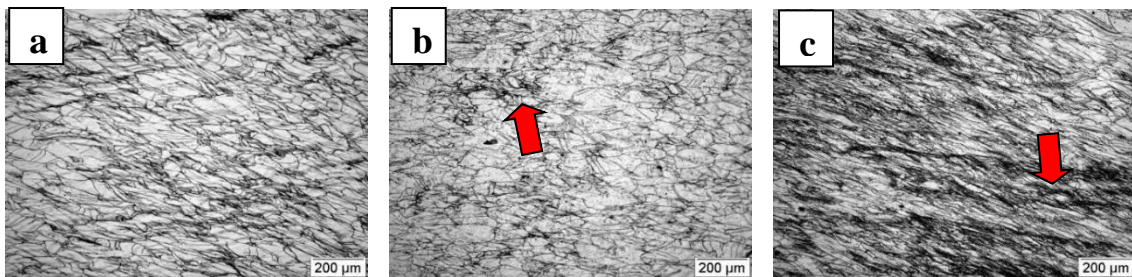


Figure 7.7: Optical microstructures of 7N at 1123K (a) 0.001s^{-1} (b) 0.1s^{-1} (pockets of strain localizations are marked) and (c) 10s^{-1} (the arrow indicates the shear banding).

These features are investigated in greater detail through EBSD analysis. Fig. 7.8a shows the IPF map collected at strain rate 0.01s^{-1} . The black lines indicate the grain boundaries greater than 15° and the red lines represent the grain boundaries greater than 10° . At this low strain rate, the nucleation of grain primarily occurs at grain boundaries by bulging of parent grains [80]. This gives rise to necklace-type DRX, an example of which is marked in Fig. 7.8a. At high strain rates, such as 10s^{-1} , fine grains form in clusters across the microstructures. These nucleating grains destroy the parent grain, causing DRX to progress by the rotational mechanism [173]. This is illustrated in Fig. 7.8b, where the arrow denotes a nucleating front growing into parent grain.

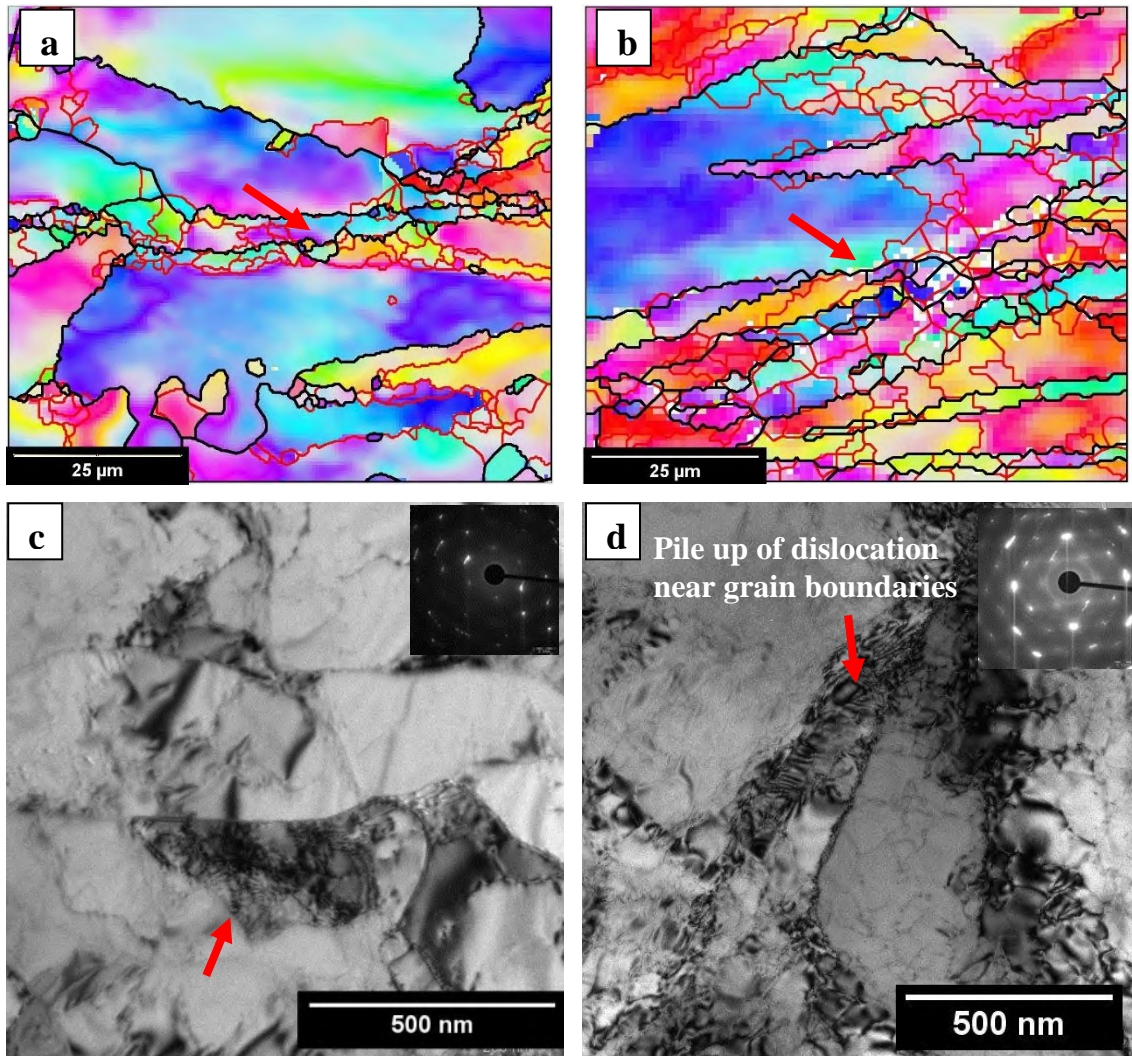


Figure 7.8: Inverse pole figure mapping of 7N at 1123K at a) 0.01 s^{-1} (arrow indicates the necklace structure) and b) 10 s^{-1} (arrow indicates the fine DRX grains). The black lines indicates the grain boundaries $>15^\circ$ and red lines indicates grainboundaries $>10^\circ$. TEM images of 7N at 1123K at c) 0.01 s^{-1} and d) 10 s^{-1} .

Work hardening takes place during deformation, causing dislocation multiplication. At low strain rates, sufficient time is available for dislocation motion, leading to a low rate of dislocation pile-ups. At higher strain rates, deformation completes in a fraction of a second, providing inadequate time for uninterrupted dislocation motion. The mismatch between material flow and dislocation motion leads to more dislocation pile-ups. The nature of dislocations and dislocation pile-ups are studied by using TEM. It is found that the dislocation density is low at low strain rate. As example, Fig. 7.8c shows

the substructure formed in 7N grade steel after deformation at 0.01s^{-1} . Dislocations are predominantly found at triple boundary junctions. On availability of sufficient thermal activation energy, new cells are known to form at these triple junctions [174]. One such cell with high dislocation density inside it is marked in Fig. 7.8c.

On the other hand, after deformation at higher strain rates, several dislocation pileups are formed at grain boundaries [175]. In the present study, similar features have been found, as shown in Fig 7.8d. It is generally accepted that pinned dislocations act as sites for increased internal friction on account of dislocation damping [176]. This internal friction is likely to cause localized heating, which in turn would cause a local annihilation of dislocations. Such regions, therefore, become softer than the surroundings and promote localized flow.

7.2.3. Effect of geometry on ASB formation and propagation

It has been previously mentioned that ASBs forms due to surface contact between die and material surface. During deformation, the friction between these contacts is one of the major cause for the formation of shear band [118]. It is also responsible for the intensity of the banding. This can be reduced by pre-heating the die to the working temperature, and also by applying lubrication for smooth deformation. In our present work, these two factors have been taken care. Consequently, the third factor, i.e. geometry at contact surface is expected to influence ASB formation and propagation as presence of any sharp corner may contribute to initial stress concentration and hence leading to band formation.

The previous sections have established that ASBs are more prominent at lower temperatures and high strain rates for instance, 1123K at 10s^{-1} . Therefore, the effect of deformation geometry has been studied at these banding-prone conditions. Three different

specimen geometries have been used; the widely used cylinder with circular cross-section, cuboid with rectangular cross section and a cuboid with square cross section. The height and cross-sectional area of the specimens has been kept constant, i.e. 15mm and $80\pm 2 \text{ mm}^2$ respectively to keep the applied pressure on the surface constant. The test conditions, including lubricant and atmosphere, are kept constant across all three geometries.

The resulting microstructures are shown for all three geometries in Fig. 7.9. The width of the ASB was found to be highest in rectangular cross-section (Fig. 7.9a), followed by circular cross-section (Fig. 7.9b) and lowest in the square cross-section (Fig. 7.9c). However, the intensity was found to be highest in rectangular cross-section (Fig. 7.9d), followed by square cross-section (Fig. 7.9f) and circular cross-section (Fig. 7.9e). It can be seen that the aspect ratios of grains are highest for rectangular cross section in Fig. 7.9d. The microstructure indicates closely spaced sub bands in the main band. Some smaller grains are also visible at the end of the elongated grains. These grains are usually formed due to grain fragmentation. The aspect ratio is lowest for circular cross section as visible in Fig. 7.9e. The microstructure shows that the spacing between the sub bands is not as regular as it is noticed in case of rectangular cross-section. The square cross-section (Fig. 7.9f) shows elongated grains with aspect ratio intermediate between the rectangular and square cross-sections. Fig. 7.9f also shows that the spacing between the sub bands inside the main bands is somewhat regular. All these results indicates that when the propensity of the material to form shear bands in a deformation domain is an inherent characteristic of material, the deformation geometry plays crucial role in deciding the intensity of the shear bands. In all three geometries, the contact surfaces are constrained by to move normal to the applied load. In the circular cross-section, all

diameters are equal and hence material may flow in any direction. The ASB can form in any direction on the cross-section, while making 45° to the loading axis.

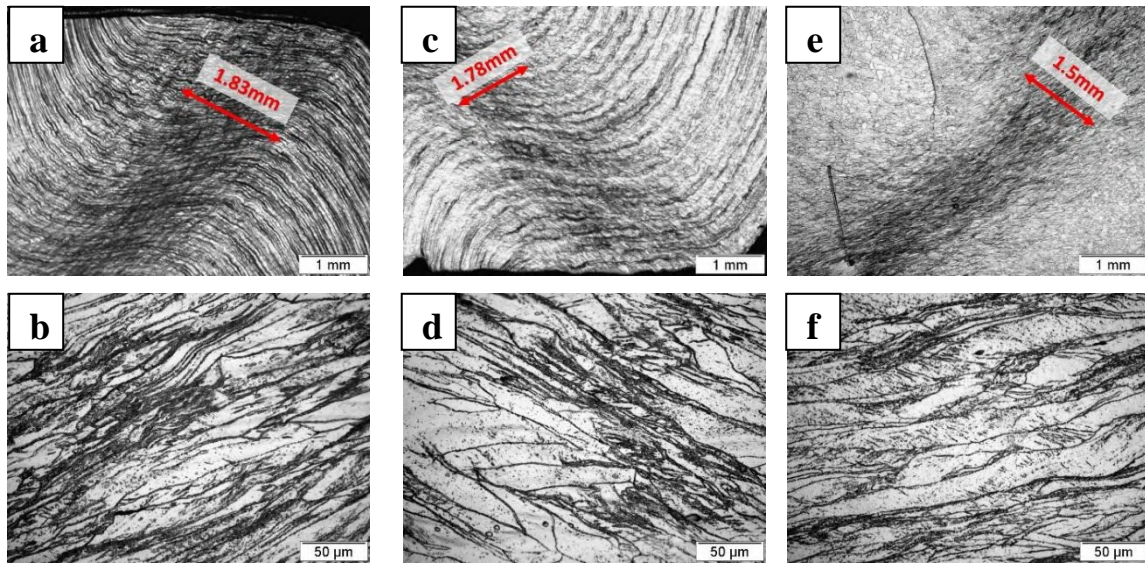


Figure 7.9: Microstructures of 7N at 1123K , 10s^{-1} at 25X and 500X : (a,b) rectangular cross-section, (c,d) circular cross-section ; (e,f) square cross-section.

Formation of the band leads to preferential shear, causing ovality after deformation. Based on loading condition, material properties, adiabatic temperature rise, this band is formed and finally an oval shaped base is obtained. In case of the square cross-section, corners and edges play an important role. These areas are subjected to high friction causing a resistance in material flow. This leads to inhomogeneous flow of material and cause of high intensity of shear bands. In rectangular base specimen, the flow is preferred in breadth direction as it has the shorter edge. Hence deforms to assume rectangular cross-section. The square base specimen has both the edges of equal length. So the flow again chooses random direction gets deformed to rectangular cross-section.

7.2.4. Influence of nitrogen content on ASB formation

In addition to deformation-related variables, the chemical composition of the steel also influences the formation of ASBs. In particular, the effect of nitrogen content is

investigated in the 7N and 22N grades. The microstructures of 7N and 22N grades, following deformation at 1123K, $10s^{-1}$ are shown in Fig. 7.10a and Fig. 7.10b, respectively. The tendency to form flow localization and ASB appears to be higher in 22N steel. In addition, a large number of fine grains along the bands are visible in Fig. 7.10b.

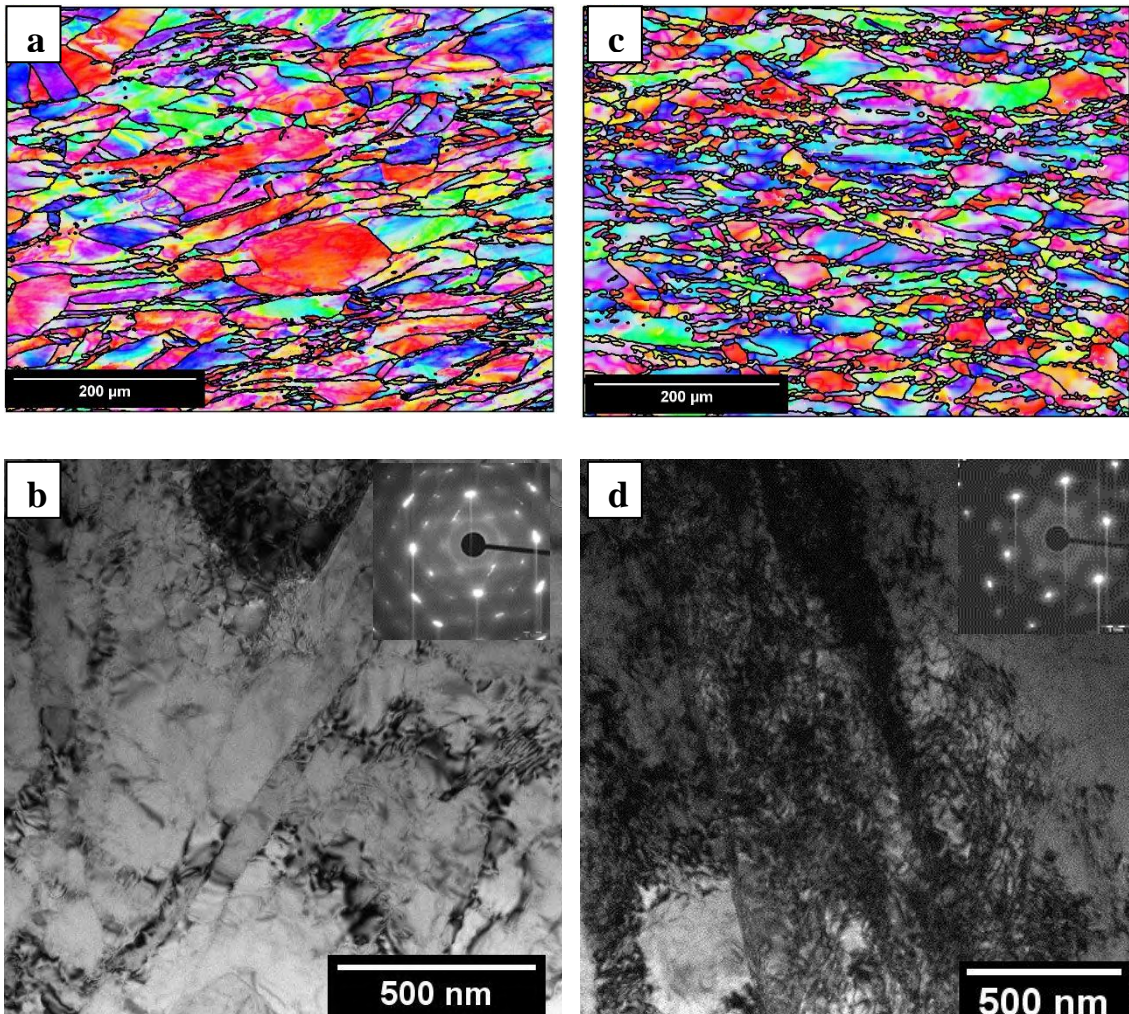


Figure 7.10: Inverse pole figure mapping and TEM images at 1123K, $10s^{-1}$ at 0.5 strain of (a, b) 7N and (c, d) 22N respectively.

The corresponding TEM images in Fig. 7.10c and Fig. 7.10d shows that dislocation density increases with nitrogen addition. Areas with high contrast are seen in Fig. 7.10d (corresponding to 22N grade). These are attributed to excess strain field around dislocations. The nitrogen atoms in solid solution act to obstruction the dislocation

motion. Thus, dislocations get pinned down by the solute atoms restricting material movement [5], necessitating a higher stress for deformation. The localized pinning of dislocations by obstacles (in this case interstitial solute atoms) causes an increase in internal friction even at low strains [176]. The increase in internal friction is expected to locally raise temperature.

In addition, higher nitrogen content is responsible high work hardening in the steel. As a consequence the critical condition for ASB formation is met at lower strain levels. Hence ϵ_{ASB} is lowered with addition of nitrogen, which concurs with Fig. 7.2a. Low critical strain promotes an increase in ASB nucleation together to form denser shear bands. It is therefore concluded that the addition of nitrogen is favorable for ASB. Additionally, during banding, nucleation of fine grains around the parent grain (as shown in Fig. 7.10d) occurs with the aid of additional thermal activation energy due to trapped heat.

7.3. Mechanism behind the formation of ASB in hot isothermal forging

The preceding sections elucidate the various microstructural changes occurring during deformation and ASB formation, along with the parameters that cause the respective changes. The inferences drawn from these studies are used to propose a mechanism of ASB formation. It has been calculated that ASB initiates at strain level of 0.3 for 7N grade steel deformed at 1123K at $10s^{-1}$. Therefore, a separate specimen has been deformed upto strain level of 0.3 at the same temperature-strain rate conditions. A partial band is found to be visible macroscopically. The banded region has subsequently been subjected to extensive microstructural investigation. An EBSD scan of the given region was used to generate the 'band contrast map' shown in Fig. 7.11. The grayscale band contrast map qualitatively shows strain accumulation, with darkest areas

representing maximum strain accumulation. Such maps are useful to identify various boundaries in a material. The map shown in Fig. 7.11 reveals the presence of micro bands inside several grains. These microbands are often found in the vicinity of twins, and frequently at a 24° alignment with respect to the twins. The figure also shows the preferential site for the initiation of flow localization. The high magnification maps in Fig. 7.12a and Fig. 7.12b collected at 1123K, 10 s^{-1} at 50% strain, shows the formation of subgrains along microbands. For the purpose of this study, grain boundaries are considered to have a misorientation greater than 15° , whereas sub-grain boundaries are considered to have a minimum misorientation of 5° . Fig. 7.12a shows the IPF map, with band initiation marked by a box.

The same area is shown in the grain boundary map of Fig. 7.12b, with grains and subgrains indicated separately. It is observed that microbands initiate from grain boundaries. This is especially clear in the area demarcated by a rectangular box. Inside this area, subgrains form in chain-like arrangements along microbands seen in Fig. 7.11. These micro-bands, therefore, are formed when a grain is subjected to loading conditions. The width of microbands is found to vary from 1-5 μm . Grain boundaries and twin boundaries present obstacles to propagation of microbands within a grain [177].

The propagation of these microbands, obstruction at boundaries and the subsequent nucleation of fresh grains is explained by the schematic proposed in Fig. 7.13. Two types of microbands can be formed; one is the primary microbands formed perpendicular to the loading direction, denoted 'A' in Fig. 7.13. The other type is the secondary microbands, formed on account of resistance from grain boundaries. These are denoted 'B' in Fig. 7.13. The intersection of primary and secondary microbands (Step 2 in Fig. 7.13) forms cellular walls of dislocations. On further loading, it is proposed that these cells rotate to form low-angle boundaries. This is responsible for the sub-grains seen

in Fig. 7.12b. On account of higher dislocation density and consequent high internal friction at the intersections, adiabatic heating can occur, leading to recrystallization of a few grains (Fig. 7.13 Step 3).

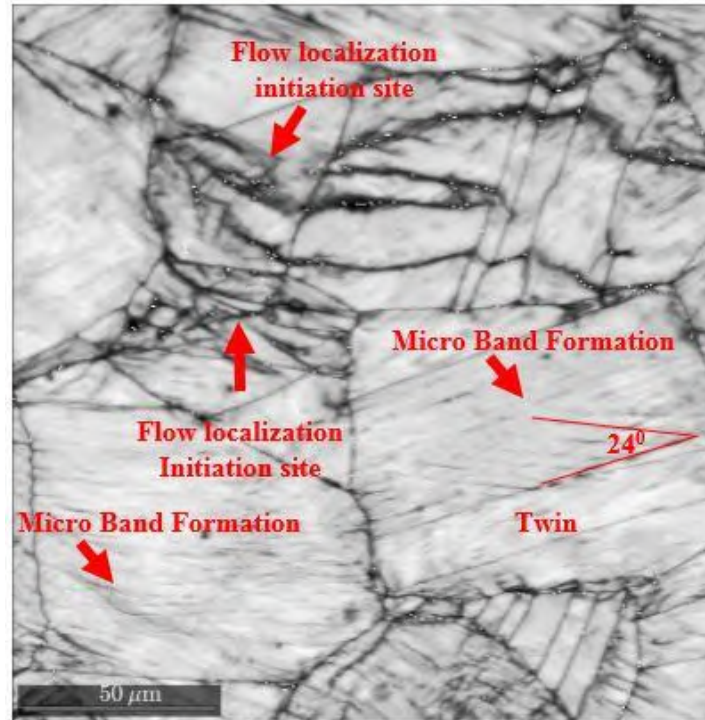


Figure 7.11: Band contrast imaging of 7N at 1123K, $10s^{-1}$ at 0.3 strain. The arrows indicates the formation of micro bands.

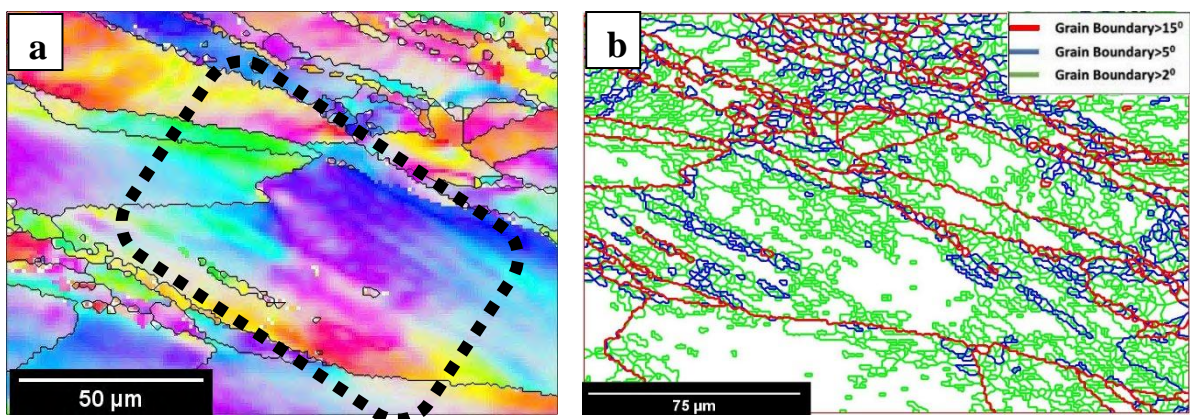


Figure 7.12: EBSD maps of 7N at 1123K, $10s^{-1}$ at 0.5 strain: (a) IPF map and (b) Grain boundary map. The marked area shows the formation of low angle grain boundaries along the bandings.

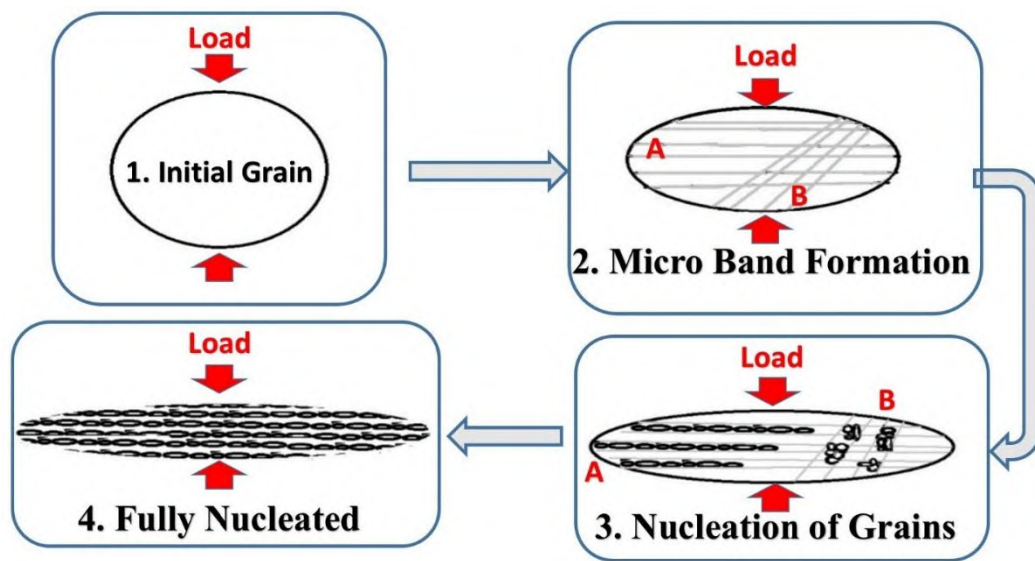


Figure 7.13 : Schematic illustration of the formation process of nucleation of sub grain inside the microbands in a grain in ASB region.

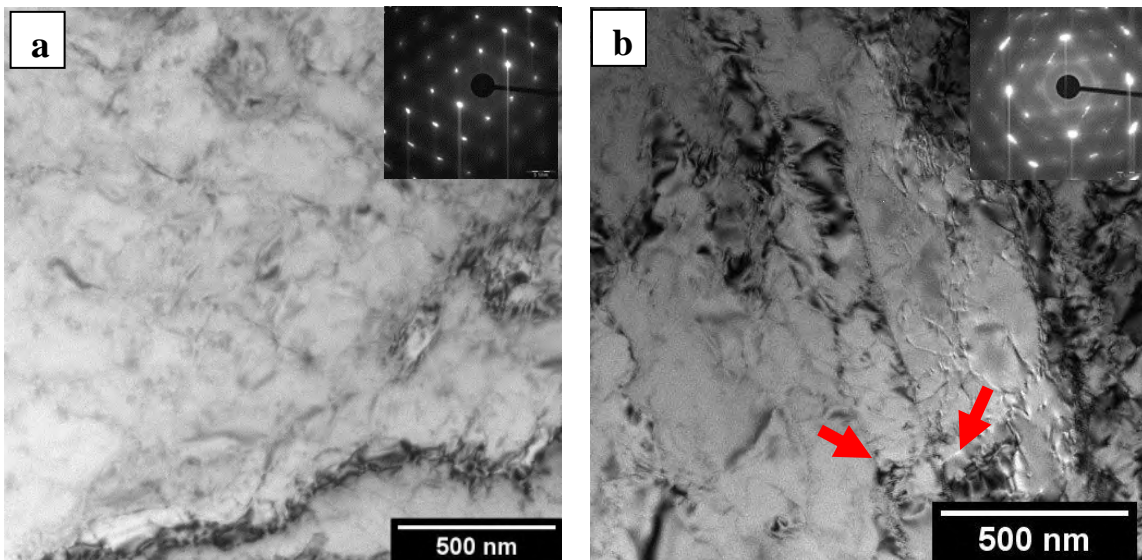


Figure 7.14: TEM images with SAD pattern of 7N at 1123K, 10s^{-1} at (a) 0.3 strain and (b) 0.5 strain (arrow indicates the secondary twins).

This concurs with the conclusion of Rittel et al. [178] that stored energy during working is the driving force for microstructural rearrangement in DRX as well as ASB formation. With continued softening and trapping of heat, clusters of recrystallized grains form, creating a soft, macroscopic shear band (Fig. 7.13 Step 4).

The TEM images at of 7N grade steel deformed at strain levels of 0.3 (partially banded) and 0.5 (fully banded) at 1123K at 10s^{-1} are shown in Fig. 7.14. It is seen in Fig. 7.14a that the dislocation density is quite low at 0.3 strain level. A small region of dislocation tangles is visible. Further, the SAD pattern indicates predominantly single crystal orientation in the examined region. On the other hand, Fig. 7.14b shows that at 0.5 strain level, dislocation density is increased across the microstructure. Additionally, the distortion in the SAD pattern indicates polycrystalline features in the examined region. This is in agreement with the development of fine grains shown in Fig. 7.12. In particular, some lath structures are observed in Fig. 7.14b. The accompanying SAD pattern in Fig. 7.14b faintly indicates secondary twins similar to those reported by Xue et al. in [179]. However, the experiments of Xue et al. have been carried out at room temperature, applying much higher strain rates (10^5s^{-1}) than the present study. These differences between experimental conditions raise uncertainties over the formation of secondary twins at hot deformation conditions. The lath structures observed in TEM examination, therefore, may be microbands or secondary twins. The resolution of this uncertainty merits further detailed investigation. Despite this uncertainty, it may be safely concluded that the formation of dislocation tangles in the partially banded specimen is the precursor to subsequent subgrains formation, recrystallization and ASB formation.

7.4. Conclusions

- Flow behavior of the steel has been analyzed to identify the critical strain and stress for initiation of ASB. It is found that with increase in temperature, the critical strain required for adiabatic shear band formation increases. The same trend is maintained for all the variants.
- The specimens deformed at low temperature, become more susceptible to band formation as adiabatic temperature rise is higher at lower deformation temperature and thermal conductivity of the material is relatively poor at lower temperature compared to that is seen at higher temperatures.
- With increase in nitrogen content in 316LN SS, the steel becomes more prone to form adiabatic shear bands when deformed at higher strain rates. Increase in nitrogen content results in higher work hardening in 316LN SS and reduces the thermal conductivity of the steel. As a result, the critical criterion for shear band formation is easily satisfied at low strain levels.
- On the basis of the micro structural observations, a mechanism of ASB formation in 316LN SS is proposed.

Conclusions and Future Work

8.0. Conclusions

In this work, the influence of nitrogen on hot deformation behavior and workability of 316LN SS has been studied using three variants of the steel containing 0.07 wt. % (7N), 0.11 wt. % (11N) and 0.22 wt. % (22N) nitrogen. Hot isothermal uniaxial compression tests were carried out in the temperature range of 1123K-1473K and at constant strain rates of 0.001-10 s⁻¹ upto 0.65 true strain to generate experimental data. Detailed microstructural investigation was carried out on the deformed specimens using optical microscopy. Electron back scattered diffraction and Transmission electron microscopy were used to investigate selected specimens. The influence of nitrogen on workability and hot deformation behavior was studied using both mechanical response and the microstructural findings. The key outcomes of the present work are:

- 1) The flow behavior of 316LN SS during hot deformation is found to be dependent on processing parameters, such as deformation temperature, strain rate, strain and enhancement of nitrogen content in steel. Enhancement of nitrogen in 316LN SS intensifies work hardening in the material. The utility of constitutive equations for prediction of flow behavior during alloy development stage has been analyzed using experimental results obtained from four grades of 316LN. For this study four commonly used models such as SCA, MJC, Model D8A and ANN model have been critically compared on the basis of six criteria. Both Model D8A and MJC are found suitable for their ease of use and scope for addition of new variables for alloy development. The modified versions of these two models, namely N-amended D8A is preferred to N-amended MJC as constants of the

former model can be directly used to represent the effect of nitrogen on yield stress and work hardening.

- 2) Critical strain for the DRX nucleation is achieved early with enhancement in nitrogen in the steel. With increasing total interstitial (here N+C) content, SFE reduces and the probability of forming stacking faults increases in the Fe-Cr-Ni-Mo system. Since the stacking fault probability increases, the sites for dislocation forest formation increase during deformation. This is manifested as higher micro-strain in the variants having higher interstitial content. As a result, in high nitrogen variants, DRX initiation occurs at lower strain levels.
- 3) More number of nitrogen atoms in the material enhances the probability of formation of more dislocation cells which serve as active sites for nucleation. As a result, number of DRX grains accordingly increases with enhancement in nitrogen in the steels. The increase in nitrogen content makes 316LN SS less prone to grain growth after DRX. The reason could be attributed to the more number of DRX nucleation with increase in nitrogen content in the steel.
- 4) The variation of critical strain with strain rate does not correspond to the overall DRX fraction in any variant. This indicates the importance of time and temperature, in addition to the accumulation of stored energy in controlling the DRX fraction in the alloy. Because of this dependency, some variants show sluggish DRX behavior at strain rate around 1s^{-1} . The degree of dependency of DRX fraction on time, however, varies with interstitial content, and is highest in the alloy with lowest interstitial content. As the interstitial content increases in the alloy, the DRX fraction practically becomes rate-independent.
- 5) 7N variant is suitable for majority of high temperature deformation processes such as rolling, forging and extrusion which are carried out at high speed. 11N and 22N

variants in their present condition are not suitable for high speed extrusion process where material undergo high strain levels during deformation. However, these variants of 316LN SS can be safely used for forgings where low reduction ratio is achieved in one step. 316LN shows two unstable domains; one occurs at high strain rate ($1-10s^{-1}$) domain and the other occurs at low strain rate domains ($0.01-0.1s^{-1}$ at 1123-1273K).

- 6) With increase in nitrogen content in 316LN SS, the steel becomes more prone to form adiabatic shear bands when deformed at higher strain rates. Increase in nitrogen content results in higher work hardening in 316LN SS and reduces the thermal conductivity of the steel. As a result, the critical criterion for shear band formation is easily satisfied at low strain levels. On the basis of the micro structural observations, a mechanism of ASB formation in 316LN SS is proposed.

8.1. Suggestions for future work

- 1) The validity of the results reported here needs to be validated industrially.
- 2) The variation of stacking fault energy needs to be validated with high temperature XRD.
- 3) Role of deformation geometry in deciding the intensity of shear bands can be studied in detail using FEM simulations.
- 4) Approaches are needed to model negative strain rate sensitivity of steel.

References

- [1] Power. India Brand Equity Foundation, February 2018.
- [2] B. Raj, S. Mannan, P.V. Rao, M. Mathew. Development of fuels and structural materials for fast breeder reactors, *Sadhana* 27 (2002) 527-558.
- [3] A. Bhaduri, K. Laha, V. Ganesan, T. Sakthivel, M. Nandagopal, G.P. Reddy, J.G. Kumar, V. Vijayanand, S.P. Selvi, G. Srinivasan. Advanced materials for structural components of Indian sodium-cooled fast reactors, *Int. J. Press. Vessels Pip.* 139 (2016) 123-136.
- [4] M. Matula, L. Hyspecka, M. Svoboda, V. Vodarek, C. Dagbert, J. Galland, Z. Stonawska, L. Tuma. Intergranular corrosion of AISI 316L steel, *Mater. Charact.* 46 (2001) 203-210.
- [5] V. Gavriljuk, H. Berns. High nitrogen steels: structure, properties, manufacture, applications, Springer Science & Business Media, 2013.
- [6] D.W. Kim, J.-H. Chang, W.-S. Ryu. Evaluation of the creep-fatigue damage mechanism of Type 316L and Type 316LN stainless steel, *Int. J. Press. Vessels. Pip.* 85 (2008) 378-384.
- [7] G.P. Reddy, A. Nagesha, R. Sandhya, S. Sankaran, M. Mathew, K.B.S. Rao. Thermomechanical and Isothermal Fatigue Behavior of 316LN Stainless Steel with Varying Nitrogen Content, *Metall. Mater. Trans. A* 46 (2015) 695-707.
- [8] R.P. Reed. Nitrogen in austenitic stainless steels, *JOM* 41 (1989) 16-21.
- [9] T. Jayakumar, A. Bhaduri, M. Mathew, S. Albert, U. Kamachi Mudali. Nitrogen enhanced 316LN austenitic stainless steel for sodium cooled fast reactors. *Advanced Materials Research*, vol. 794: Trans Tech Publ, 2013. p.670-680.
- [10] S. Wang, K. Yang, Y. Shan, L. Li. Plastic deformation and fracture behaviors of nitrogen-alloyed austenitic stainless steels, *Mat. Sci, Eng. A* 490 (2008) 95-104.
- [11] X. Zhang, Y. Zhang, Y. Li, J. Liu. Cracking initiation mechanism of 316LN stainless steel in the process of the hot deformation, *Mat. Sci, Eng. A* 559 (2013) 301-306.
- [12] T. Byun, E. Lee, J. Hunn. Plastic deformation in 316LN stainless steel—characterization of deformation microstructures, *J. Nucl. Mater.* 321 (2003) 29-39.
- [13] D. Samantaray, S. Mandal, C. Phaniraj, A. Bhaduri. Flow behavior and microstructural evolution during hot deformation of AISI Type 316 L (N) austenitic stainless steel, *Mat. Sci, Eng. A* 528 (2011) 8565-8572.

- [14] A. Chelladurai, K. Gopal, S. Murugan, S. Albert, S. Venugopal, T. Jayakumar. Effect of energy transfer modes on solidification cracking in pulsed laser welding, *Sci. Technol. Weld. Joining* 20 (2015) 578-584.
- [15] J. Frenkel. Über die Wärmebewegung in festen und flüssigen Körpern, *Z. Phys.* 35 (1926) 652-669.
- [16] C. Wagner. Point defects and their interaction, *Annu. Rev. Mater. Sci.* 7 (1977) 1-24.
- [17] N. Petch, J. Heslop. The stress to move a free dislocation in alpha iron, *Philos. Mag.* 47 (1956) 8S6.
- [18] S.D. Mesarovic. Dynamic strain aging and plastic instabilities, *J. Mech. Phys. Solids* 43 (1995) 671-700.
- [19] W. Schilling. Self-interstitial atoms in metals, *J. Nucl. Mater.* 69 (1978) 465-489.
- [20] M.O. Speidel. Nitrogen containing austenitic stainless steels, *Materialwiss. Werkstofftech.* 37 (2006) 875-880.
- [21] V. Gavriljuk, B. Shanina. Interstitial elements in steel: effect on structure and properties: Dedicated to Professor Hans Berns on the occasion of his 75th birthday, *HTM J. Heat Treatment Mat.* 65 (2010) 189-194.
- [22] L.-Å. Norström. The influence of nitrogen and grain size on yield strength in Type AISI 316L austenitic stainless steel, *Met. Sci.* 11 (1977) 208-212.
- [23] Production of High Nitrogen Steels: Part Three. *Total Materia*, 2012.
- [24] M.U. Kamachi, B. Raj. *High Nitrogen Steels and Stainless Steels*, New Delhi: Narosa Publishing House 1 (2004) 14.
- [25] S.N. Ghali, A. Ahmed, M. Eissa, H. El-Faramawy, M. Mishreky, T. Mattar. Production and application of advanced high nitrogen steel. *International Conference on Science and Technology of Ironmaking and Steelmaking*, 2013. p.16-18.
- [26] V. Ganesan, M. Mathew, K. Sankara Rao. Influence of nitrogen on tensile properties of 316LN SS, *Mater. Sci. Technol.* 25 (2009) 614-618.
- [27] M. Mathew, K. Laha, V. Ganesan. Improving creep strength of 316L stainless steel by alloying with nitrogen, *Mat. Sci, Eng. A* 535 (2012) 76-83.
- [28] A. Poonguzhali, M. Pujar, U.K. Mudali. Effect of nitrogen and sensitization on the microstructure and pitting corrosion behavior of AISI type 316LN stainless steels, *J. Mater. Eng. Perform.* 22 (2013) 1170-1178.
- [29] A. He, G. Xie, H. Zhang, X. Wang. A comparative study on Johnson–Cook, modified Johnson–Cook and Arrhenius-type constitutive models to predict the high temperature flow stress in 20CrMo alloy steel, *Mater. Des.* 52 (2013) 677-685.

- [30] L. Zhang, X. Feng, X. Wang, C. Liu. On the constitutive model of nitrogen-containing austenitic stainless steel 316LN at elevated temperature, *PLoS One* 9 (2014) e102687.
- [31] B. Guo, H. Ji, X. Liu, L. Gao, R. Dong, M. Jin, Q. Zhang. Research on flow stress during hot deformation process and processing map for 316LN austenitic stainless steel, *J. Mater. Eng. Perform.* 21 (2012) 1455-1461.
- [32] Y. Lin, X.-M. Chen. A critical review of experimental results and constitutive descriptions for metals and alloys in hot working, *Mater. Des.* 32 (2011) 1733-1759.
- [33] G.R. Johnson, W.H. Cook. A constitutive model and data for metals subjected to large strains, high strain rates and high temperatures. *Proceedings of the 7th International Symposium on Ballistics*, vol. 21: The Netherlands, 1983. p.541-547.
- [34] G.R. Johnson, W.H. Cook. Fracture characteristics of three metals subjected to various strains, strain rates, temperatures and pressures, *Eng. fract. mech.* 21 (1985) 31-48.
- [35] F.J. Zerilli, R.W. Armstrong. Dislocation-mechanics-based constitutive relations for material dynamics calculations, *J. Appl. Phys.* 61 (1987) 1816-1825.
- [36] D. Samantaray, S. Mandal, A. Bhaduri, S. Venugopal, P. Sivaprasad. Analysis and mathematical modelling of elevated temperature flow behavior of austenitic stainless steels, *Mat. Sci, Eng. A* 528 (2011) 1937-1943.
- [37] D. Trimble, H. Shipley, L. Lea, A. Jardine, G.E. O'Donnell. Constitutive analysis of biomedical grade Co-27Cr-5Mo alloy at high strain rates, *Mat. Sci, Eng. A* 682 (2017) 466-474.
- [38] Z. Zhu, Y. Lu, Q. Xie, D. Li, N. Gao. Mechanical properties and dynamic constitutive model of 42CrMo steel, *Mater. Des.* 119 (2017) 171-179.
- [39] J. Cai, Y. Lei, K. Wang, X. Zhang, C. Miao, W. Li. A comparative investigation on the capability of modified zerilli-armstrong and arrhenius-type constitutive models to describe flow behavior of BFe10-1-2 cupronickel alloy at elevated temperature, *J. Mater. Eng. Perform.* 25 (2016) 1952-1963.
- [40] Y. Lin, X.-M. Chen, G. Liu. A modified Johnson–Cook model for tensile behaviors of typical high-strength alloy steel, *Mat. Sci, Eng. A* 527 (2010) 6980-6986.
- [41] Y. Lin, X.-M. Chen. A combined Johnson–Cook and Zerilli–Armstrong model for hot compressed typical high-strength alloy steel, *Comp. Mater. Sci.* 49 (2010) 628-633.
- [42] Y.C. Lin, Q.-F. Li, Y.-C. Xia, L.-T. Li. A phenomenological constitutive model for high temperature flow stress prediction of Al–Cu–Mg alloy, *Mat. Sci, Eng. A* 534 (2012) 654-662.

- [43] Z. Akbari, H. Mirzadeh, J.-M. Cabrera. A simple constitutive model for predicting flow stress of medium carbon microalloyed steel during hot deformation, *Mater. Des.* 77 (2015) 126-131.
- [44] S. Mandal, B.T. Gockel, S. Balachandran, D. Banerjee, A.D. Rollett. Simulation of plastic deformation in Ti-5553 alloy using a self-consistent viscoplastic model, *Int. J. Plast.* 94 (2017) 57-73.
- [45] P.S. Follansbee, U.F. Kocks. A constitutive description of the deformation of copper based on the use of the mechanical threshold stress as an internal state variable, *Acta Metall.* 36 (1988) 81-93.
- [46] K.S. Prasad, A.K. Gupta, Y. Singh, S.K. Singh. A Modified Mechanical Threshold Stress Constitutive Model for Austenitic Stainless Steels, *J. Mater. Eng. Perform.* 25 (2016) 5411-5423.
- [47] L.-E. Lindgren, K. Domkin, S. Hansson. Dislocations, vacancies and solute diffusion in physical based plasticity model for AISI 316L, *Mech. Mater.* 40 (2008) 907-919.
- [48] C.M. Sellars, W. McTegart. On the mechanism of hot deformation, *Acta Metall.* 14 (1966) 1136-1138.
- [49] C. Phaniraj, D. Samantaray, S. Mandal, A. Bhaduri. A new relationship between the stress multipliers of Garofalo equation for constitutive analysis of hot deformation in modified 9Cr–1Mo (P91) steel, *Mat. Sci, Eng. A* 528 (2011) 6066-6071.
- [50] Y. Lin, M.-S. Chen, J. Zhong. Constitutive modeling for elevated temperature flow behavior of 42CrMo steel, *Comp. Mat. Sci.* 42 (2008) 470-477.
- [51] C. Zener, J.H. Hollomon. Effect of strain rate upon plastic flow of steel, *J. Appl. Phys.* 15 (1944) 22-32.
- [52] F. Slooff, J. Zhou, J. Duszczyk, L. Katgerman. Constitutive analysis of wrought magnesium alloy Mg–Al4–Zn1, *Scripta Mater.* 57 (2007) 759-762.
- [53] D. Samantaray, S. Mandal, A. Bhaduri. Constitutive analysis to predict high-temperature flow stress in modified 9Cr–1Mo (P91) steel, *Mater. Des.* 31 (2010) 981-984.
- [54] D. Trimble, G.E. O'Donnell. Constitutive Modelling for elevated temperature flow behavior of AA7075, *Mater. Des.* 76 (2015) 150-168.
- [55] J. Wang, G. Zhao, L. Chen, J. Li. A comparative study of several constitutive models for powder metallurgy tungsten at elevated temperature, *Mater. Des.* 90 (2016) 91-100.
- [56] P. Zhang, C. Hu, Q. Zhu, C.-g. Ding, H.-y. Qin. Hot compression deformation and constitutive modeling of GH4698 alloy, *Mater. Des.* (1980-2015) 65 (2015) 1153-1160.

- [57] Y.C. Lin, D.-X. Wen, J. Deng, G. Liu, J. Chen. Constitutive models for high-temperature flow behaviors of a Ni-based superalloy, *Mater. Des.* 59 (2014) 115-123.
- [58] A.K. Shukla, S.V.S. Narayana Murty, S.C. Sharma, K. Mondal. Constitutive modeling of hot deformation behavior of vacuum hot pressed Cu–8Cr–4Nb alloy, *Mater. Des.* 75 (2015) 57-64.
- [59] D. Samantaray, S. Mandal, A. Bhaduri. A comparative study on Johnson Cook, modified Zerilli–Armstrong and Arrhenius-type constitutive models to predict elevated temperature flow behavior in modified 9Cr–1Mo steel, *Comp. Mat. Sci.* 47 (2009) 568-576.
- [60] D. Samantaray, A. Patel, U. Borah, S. Albert, A. Bhaduri. Constitutive flow behavior of IFAC-1 austenitic stainless steel depicting strain saturation over a wide range of strain rates and temperatures, *Mater. Des.* 56 (2014) 565-571.
- [61] A. Jenab, I. Sari Sarraf, D.E. Green, T. Rahmaan, M.J. Worswick. The Use of genetic algorithm and neural network to predict rate-dependent tensile flow behavior of AA5182-O sheets, *Mater. Des.* 94 (2016) 262-273.
- [62] S.-W. Wu, X.-G. Zhou, G.-M. Cao, Z.-Y. Liu, G.-D. Wang. The improvement on constitutive modeling of Nb-Ti micro alloyed steel by using intelligent algorithms, *Mater. Des.* 116 (2017) 676-685.
- [63] S. Mandal, P. Sivaprasad, S. Venugopal, K. Murthy, B. Raj. Artificial neural network modeling of composition–process–property correlations in austenitic stainless steels, *Mat. Sci, Eng. A* 485 (2008) 571-580.
- [64] X. Xia, J. Nie, C. Davies, W. Tang, S. Xu, N. Birbilis. An artificial neural network for predicting corrosion rate and hardness of magnesium alloys, *Mater. Des.* 90 (2016) 1034-1043.
- [65] S. Malinov, W. Sha. Application of artificial neural networks for modelling correlations in titanium alloys, *Mat. Sci, Eng. A* 365 (2004) 202-211.
- [66] D.-X. Wen, Y. Lin, Y. Zhou. A new dynamic recrystallization kinetics model for a Nb containing Ni-Fe-Cr-base superalloy considering influences of initial δ phase, *Vacuum* 141 (2017) 316-327.
- [67] A. Sarkar, A. Marchattiwari, J. Chakravartty, B. Kashyap. Kinetics of dynamic recrystallization in Ti-modified 15Cr–15Ni–2Mo austenitic stainless steel, *J. Nucl. Mater.* 432 (2013) 9-15.
- [68] J.J. Jonas, X. Queleñec, L. Jiang, É. Martin. The Avrami kinetics of dynamic recrystallization, *Acta Mater.* 57 (2009) 2748-2756.
- [69] Y. Han, S. Yan, B. Yin, H. Li, X. Ran. Effects of temperature and strain rate on the dynamic recrystallization of a medium-high-carbon high-silicon bainitic steel during hot deformation, *Vacuum* 148 (2018) 78-87.

- [70] T. Sakai, J.J. Jonas. Overview no. 35 dynamic recrystallization: mechanical and microstructural considerations, *Acta Metall.* 32 (1984) 189-209.
- [71] K. Huang, R. Logé. A review of dynamic recrystallization phenomena in metallic materials, *Mater. Des.* 111 (2016) 548-574.
- [72] C. de Abreu Martins, E. Poliak, L.B. Godefroid, N. Fonstein. Determining the Conditions for Dynamic Recrystallization in Hot Deformation of C–Mn–V Steels and the Effects of Cr and Mo Additions, *ISIJ Int.* 54 (2014) 227-234.
- [73] H.-l. Wei, G.-q. Liu, H.-t. Zhao, M.-h. Zhang. Effect of carbon content on hot deformation behaviors of vanadium microalloyed steels, *Mat. Sci, Eng. A* 596 (2014) 112-120.
- [74] H. Beladi, P. Hodgson. Effect of carbon content on the recrystallization kinetics of Nb-steels, *Scripta Mater.* 56 (2007) 1059-1062.
- [75] I. Mejía, A. Bedolla-Jacuinde, C. Maldonado, J. Cabrera. Determination of the critical conditions for the initiation of dynamic recrystallization in boron microalloyed steels, *Mat. Sci, Eng. A* 528 (2011) 4133-4140.
- [76] E. López-Chipres, I. Mejía, C. Maldonado, A. Bedolla-Jacuinde, M. El-Wahabi, J. Cabrera. Hot flow behavior of boron microalloyed steels, *Mat. Sci, Eng. A* 480 (2008) 49-55.
- [77] S. Kim, S. Choi, Y. Lee. Influence of phosphorous and boron on dynamic recrystallization and microstructures of hot-rolled interstitial free steel, *Mat. Sci, Eng. A* 406 (2005) 125-133.
- [78] A. Soussan, S. Degallaix, T. Magnin. Work-hardening behavior of nitrogen-alloyed austenitic stainless steels, *Mat. Sci, Eng. A* 142 (1991) 169-176.
- [79] J. Simmons. Overview: high-nitrogen alloying of stainless steels, *Mat. Sci, Eng. A* 207 (1996) 159-169.
- [80] D. Samantaray, S. Mandal, M. Jayalakshmi, C. Athreya, A. Bhaduri, V.S. Sarma. New insights into the relationship between dynamic softening phenomena and efficiency of hot working domains of a nitrogen enhanced 316L (N) stainless steel, *Mat. Sci, Eng. A* 598 (2014) 368-375.
- [81] A. Taylor, P. Cizek, P. Hodgson. Comparison of 304 stainless steel and Ni–30wt.% Fe as potential model alloys to study the behavior of austenite during thermomechanical processing, *Acta Mater.* 59 (2011) 5832-5844.
- [82] J.-Y. Lee, Y.M. Koo, S. Lu, L. Vitos, S.K. Kwon. The behavior of stacking fault energy upon interstitial alloying, *Sci. Rep.* 7 (2017) 11074.
- [83] R. Neugebauer, K.-D. Bouzakis, B. Denkena, F. Klocke, A. Sterzing, A. Tekkaya, R. Wertheim. Velocity effects in metal forming and machining processes, *CIRP Annals-Manufact. Tech.* 60 (2011) 627-650.

- [84] G.E. Dieter. Mechanical metallurgy, 2001.
- [85] Y. Prasad, K. Rao, S. Sasidhar. Hot working guide: a compendium of processing maps, ASM international, 2015.
- [86] S. Venugopal, S. Mannan, Y. Prasad. Processing map for mechanical working of stainless steel type AISI 316 L, Scripta metall. 28 (1993) 715-720.
- [87] S. Semiatin, G. Lahoti, S. Oh. The occurrence of shear bands in metalworking. Material Behavior Under High Stress and Ultrahigh Loading Rates. Springer, 1983. pp. 119-159.
- [88] S. Semiatin, G. Lahoti. The occurrence of shear bands in isothermal, hot forging, Metall. Trans. A 13 (1982) 275-288.
- [89] A. Shahan, A.K. Taheri. Adiabatic shear bands in titanium and titanium alloys: a critical review, Mater. Des. 14 (1993) 243-250.
- [90] S. Walley. Shear localization: a historical overview, Metall. Mater. Trans. A 38 (2007) 2629-2654.
- [91] M.E. Backman, S.A. Finnegan. The propagation of adiabatic shear. Metallurgical Effects at High Strain Rates. Springer, 1973. pp. 531-543.
- [92] Q. Xue, G. Gray III. Development of adiabatic shear bands in annealed 316L stainless steel: Part I. Correlation between evolving microstructure and mechanical behavior, Metall. Mater. Trans. A 37 (2006) 2435-2446.
- [93] S. Semiatin, G. Lahoti. The occurrence of shear bands in nonisothermal, hot forging of Ti-6Al-2Sn-4Zr-2Mo-0.1 Si, Metall. Trans. A 14 (1983) 105-115.
- [94] G. Shen, S. Semiatin, T. Altan. Investigation of flow stress and microstructure development in non-isothermal forging of Ti-6242, J. Mater. Process. Technol. 36 (1993) 303-319.
- [95] J. Sun, P. Trimby, F. Yan, X. Liao, N. Tao, J. Wang. Shear banding in commercial pure titanium deformed by dynamic compression, Acta Mater. 79 (2014) 47-58.
- [96] M. Tamizifar, H. Omidvar, S.M.T. Salehi, Z. Salehpour, O. Khoshkalam. Effect of processing parameters on shear bands in non-isothermal hot forging of Ti-6Al-4V, Mater. Sci. Technol. 18 (2002) 21-29.
- [97] D.-l. Sang, R.-d. Fu, Y.-j. Li. Combined deformation behavior and microstructure evolution of 7050 aluminum alloy during hot shear-compression deformation, Mater. Charact. 122 (2016) 154-161.
- [98] V. Nesterenko, M. Meyers, J. LaSalvia, M. Bondar, Y. Chen, Y. Lukyanov. Shear localization and recrystallization in high-strain, high-strain-rate deformation of tantalum, Mat. Sci, Eng. A 229 (1997) 23-41.

- [99] B. Dodd, Y. Bai. Adiabatic shear localization: frontiers and advances, Elsevier, 2012.
- [100] S. Timothy. The structure of adiabatic shear bands in metals: a critical review, *Acta Metall.* 35 (1987) 301-306.
- [101] Y. Yang, B. Wang. Dynamic recrystallization in adiabatic shear band in α -titanium, *Mater. Lett.* 60 (2006) 2198-2202.
- [102] D. Sagapuram, K. Viswanathan, A. Mahato, N.K. Sundaram, R. M'Saoubi, K.P. Trumble, S. Chandrasekar. Geometric flow control of shear bands by suppression of viscous sliding. *Proc. R. Soc. A*, vol. 472: The Royal Society, 2016. p.20160167.
- [103] M. Meyers, Y. Xu, Q. Xue, M. Perez-Prado, T. McNelley. Microstructural evolution in adiabatic shear localization in stainless steel, *Acta Mater.* 51 (2003) 1307-1325.
- [104] J. Lins, H. Sandim, H.-J. Kestenbach, D. Raabe, K. Vecchio. A microstructural investigation of adiabatic shear bands in an interstitial free steel, *Mat. Sci, Eng. A* 457 (2007) 205-218.
- [105] S. Venugopal. Optimization of Workability and control of microstructure in deformation processing of austenitic stainless steels vol. Ph.D. . Madras: Anna University, 1993. p.234.
- [106] D. Samantaray, S. Mandal, A. Bhaduri. A critical comparison of various data processing methods in simple uni-axial compression testing, *Mater. Des.* 32 (2011) 2797-2802.
- [107] R. Goetz, S. Semiatin. The adiabatic correction factor for deformation heating during the uniaxial compression test, *J. Mater. Eng. Perform.* 10 (2001) 710-717.
- [108] F. Bachmann, R. Hielscher, H. Schaeben. Texture analysis with MTEX-free and open source software toolbox. *Solid State Phenomena*, vol. 160: Trans. Tech. Publ, 2010. p.63-68.
- [109] H. Rietveld. A profile refinement method for nuclear and magnetic structures, *J. Appl. Crystallogr.* 2 (1969) 65-71.
- [110] L. Lutterotti, S. Matthies, H. Wenk. MAUD: a friendly Java program for material analysis using diffraction, *IUCr: Newsletter of the CPD* 21 (1999).
- [111] N. Popa. The (hkl) dependence of diffraction-line broadening caused by strain and size for all Laue groups in Rietveld refinement, *J. Appl. Crystallogr.* 31 (1998) 176-180.
- [112] B.E. Warren. *X-ray Diffraction*, Courier Corporation, 1969.
- [113] P. Müllner, C. Solenthaler, P. Uggowitzer, M. Speidel. On the effect of nitrogen on the dislocation structure of austenitic stainless steel, *Mat. Sci, Eng. A* 164 (1993) 164-169.

- [114] J. Simmons. Influence of nitride (Cr₂N) precipitation on the plastic flow behavior of high-nitrogen austenitic stainless steel, *Scripta metall.* 32 (1995) 265-270.
- [115] D. Samantaray, S. Mandal, V. Kumar, S. Albert, A. Bhaduri, T. Jayakumar. Optimization of processing parameters based on high temperature flow behavior and microstructural evolution of a nitrogen enhanced 316L (N) stainless steel, *Mat. Sci, Eng. A* 552 (2012) 236-244.
- [116] D. Samantaray, B. Aashranth, S. Kumar, M.A. Davinci, U. Borah, S.K. Albert, A. Bhaduri. Plastic deformation of SS 316LN: Thermo-mechanical and microstructural aspects, *Procedia Eng.* 207 (2017) 1785-1790.
- [117] S. Kumar, D. Samantaray, U. Borah, A.K. Bhaduri. Analysis of Elevated Temperature Flow Behavior of 316LN Stainless Steel Under Compressive Loading, *Trans. Ind. Inst. Met.* 70 (2017) 1857-1867.
- [118] S.L. Semiatin, J.J. Jonas. Formability and workability of metals: plastic instability and flow localization, *American Society for Metals*, 1984 (1984) 299.
- [119] Y.C. Lin, J. Zhang, J. Zhong. Application of neural networks to predict the elevated temperature flow behavior of a low alloy steel, *Comp. Mat. Sci.* 43 (2008) 752-758.
- [120] G. Ji, F. Li, Q. Li, H. Li, Z. Li. A comparative study on Arrhenius-type constitutive model and artificial neural network model to predict high-temperature deformation behavior in Aermet100 steel, *Mat. Sci, Eng. A* 528 (2011) 4774-4782.
- [121] Y. Qin, Q. Pan, Y. He, W. Li, X. Liu, X. Fan. Artificial neural network modeling to evaluate and predict the deformation behavior of ZK60 magnesium alloy during hot compression, *Mater. Manuf. Processes* 25 (2010) 539-545.
- [122] A. Jenab, A.K. Taheri, K. Jenab. The use of ANN to predict the hot deformation behavior of AA7075 at low strain rates, *J. Mater. Eng. Perform.* 22 (2013) 903-910.
- [123] A. Sarkar, J. Chakravartty. Prediction of Flow Stress in Cadmium Using Constitutive Equation and Artificial Neural Network Approach, *J. Mater. Eng. Perform.* 22 (2013) 2982-2989.
- [124] T. Holota, M. Kotus, M. Holienčinová, J. Mareček, M. Zach. Application of Radar Chart in the Selection of Material for Clutch Plates, *Acta Universitatis Agriculturae et Silviculturae Mendelianae Brunensis* 63 (2015) 5.
- [125] G. Ji, F. Qin, L. Zhu, Q. Li, L. Li. Dynamic Recrystallization Kinetics of Cu-0.36Cr-0.03Zr Alloy During Hot Compression, *J. Mater. Eng. Perform.* 26 (2017) 2698-2707.
- [126] B. Aashranth, D. Samantaray, S. Kumar, A. Dasgupta, U. Borah, S.K. Albert, A. Bhaduri. Flow Softening Index for Assessment of Dynamic Recrystallization in an Austenitic Stainless Steel, *J. Mater. Eng. Perform.* 26 (2017) 3531-3547.

- [127] A. Fernández, P. Uranga, B. López, J. Rodríguez-Ibabe. Dynamic recrystallization behavior covering a wide austenite grain size range in Nb and Nb–Ti microalloyed steels, *Mat. Sci, Eng. A* 361 (2003) 367-376.
- [128] S. Zhu, H. Yan, J. Chen, Y. Wu, J. Liu, J. Tian. Effect of twinning and dynamic recrystallization on the high strain rate rolling process, *Scripta Mater.* 63 (2010) 985-988.
- [129] S. Mandal, M. Jayalakshmi, A. Bhaduri, V.S. Sarma. Effect of strain rate on the dynamic recrystallization behavior in a nitrogen-enhanced 316L (N), *Metall. Mater. Trans. A* 45 (2014) 5645-5656.
- [130] H. Zhang, K. Zhang, H. Zhou, Z. Lu, C. Zhao, X. Yang. Effect of strain rate on microstructure evolution of a nickel-based superalloy during hot deformation, *Mater. Des.* 80 (2015) 51-62.
- [131] T. Sakai, A. Belyakov, R. Kaibyshev, H. Miura, J.J. Jonas. Dynamic and post-dynamic recrystallization under hot, cold and severe plastic deformation conditions, *Prog. Mater Sci.* 60 (2014) 130-207.
- [132] T. Karthikeyan, V.T. Paul, S. Mishra, S. Saroja, M. Vijayalakshmi, I. Samajdar. Effect of thermomechanical treatment on the grain boundary character distribution in a 9Cr-1Mo ferritic steel, *Metall. Mater. Trans. A* 40 (2009) 2030-2032.
- [133] J. Favre, Y. Koizumi, A. Chiba, D. Fabregue, E. Maire. Deformation behavior and dynamic recrystallization of biomedical Co-Cr-W-Ni (L-605) alloy, *Metall. Mater. Trans. A* 44 (2013) 2819-2830.
- [134] H. Jiang, J. Dong, M. Zhang, Z. Yao. A Study on the Effect of Strain Rate on the Dynamic Recrystallization Mechanism of Alloy 617B, *Metall. Mater. Trans. A* 47 (2016) 5071-5087.
- [135] S.S. Kumar, T. Raghu, P.P. Bhattacharjee, G.A. Rao, U. Borah. Strain rate dependent microstructural evolution during hot deformation of a hot isostatically processed nickel base superalloy, *J. Alloys Compd.* 681 (2016) 28-42.
- [136] Q. Guo, D. Li, H. Peng, S. Guo, J. Hu, P. Du. Nucleation mechanisms of dynamic recrystallization in Inconel 625 superalloy deformed with different strain rates, *Rare Metals* 31 (2012) 215-220.
- [137] J. Zhao, H. Ding, Z. Jiang, D. Wei, K. Linghu. Effects of hydrogen on the critical conditions for dynamic recrystallization of titanium alloy during hot deformation, *Metall. Mater. Trans. A* 45 (2014) 4932-4945.
- [138] Z. Xu, G.-R. Zhang, T. Sakai. Effect of carbon content on static restoration of hot worked plain carbon steels, *ISIJ Int.* 35 (1995) 210-216.
- [139] G. Olson, M. Cohen. A general mechanism of martensitic nucleation: Part I. General concepts and the FCC→ HCP transformation, *Metall. Trans. A* 7 (1976) 1897-1904.

- [140] S. Curtze, V.-T. Kuokkala. Dependence of tensile deformation behavior of TWIP steels on stacking fault energy, temperature and strain rate, *Acta Mater.* 58 (2010) 5129-5141.
- [141] S. Curtze, V.-T. Kuokkala, A. Oikari, J. Talonen, H. Hänninen. Thermodynamic modeling of the stacking fault energy of austenitic steels, *Acta Mater.* 59 (2011) 1068-1076.
- [142] A.T. Dinsdale. SGTE data for pure elements, *Calphad* 15 (1991) 317-425.
- [143] I. Yakubtsov, A. Ariapour, D. Perovic. Effect of nitrogen on stacking fault energy of fcc iron-based alloys, *Acta Mater.* 47 (1999) 1271-1279.
- [144] R. Schramm, R. Reed. Stacking fault energies of seven commercial austenitic stainless steels, *Metall. Mater. Trans. A* 6 (1975) 1345-1351.
- [145] Y. Ma, W. Song, W. Bleck. Investigation of the Microstructure Evolution in a Fe-17Mn-1.5 Al-0.3 C Steel via In Situ Synchrotron X-ray Diffraction during a Tensile Test, *Materials* 10 (2017) 1129.
- [146] B.E. Warren. X-ray diffraction, 1990.
- [147] H. McQueen, S. Yue, N. Ryan, E. Fry. Hot working characteristics of steels in austenitic state, *J. Mater. Process. Technol.* 53 (1995) 293-310.
- [148] V.G. Gavriljuk, H. Berns, C. Escher, N. Glavatskaya, A. Sozinov, Y.N. Petrov. Grain boundary strengthening in austenitic nitrogen steels, *Mat. Sci, Eng. A* 271 (1999) 14-21.
- [149] H. Sun, Y.-N. Shi, M.-X. Zhang, K. Lu. Plastic strain-induced grain refinement in the nanometer scale in a Mg alloy, *Acta Mater.* 55 (2007) 975-982.
- [150] M. Olsson. Thermodynamic modeling of the stacking fault energy in austenitic stainless steels. PhD Dissertation, 2014.
- [151] J.W. Christian, S. Mahajan. Deformation twinning, *Prog. Mater Sci.* 39 (1995) 1-157.
- [152] L. Lutterotti, S. Gialanella. X-ray diffraction characterization of heavily deformed metallic specimens, *Acta Mater.* 46 (1998) 101-110.
- [153] E. Lee, T. Byun, J. Hunn, M. Yoo, K. Farrell, L. Mansur. On the origin of deformation microstructures in austenitic stainless steel: part I—microstructures, *Acta Mater.* 49 (2001) 3269-3276.
- [154] L. Mosecker, A. Saeed-Akbari. Nitrogen in chromium–manganese stainless steels: a review on the evaluation of stacking fault energy by computational thermodynamics, *Sci. Tech. of Adv. Mater.* 14 (2013) 033001.

- [155] H. Miura, M. Ozama, R. Mogawa, T. Sakai. Strain-rate effect on dynamic recrystallization at grain boundary in Cu alloy bicrystal, *Scripta Mater.* 48 (2003) 1501-1505.
- [156] H. Jiang, J. Dong, M. Zhang, Z. Yao. Evolution of twins and substructures during low strain rate hot deformation and contribution to dynamic recrystallization in alloy 617B, *Mat. Sci, Eng. A* 649 (2016) 369-381.
- [157] V. Randle, G. Rohrer, Y. Hu. Five-parameter grain boundary analysis of a titanium alloy before and after low-temperature annealing, *Scripta Mater.* 58 (2008) 183-186.
- [158] H. Gleiter. The formation of annealing twins, *Acta Metall.* 17 (1969) 1421-1428.
- [159] W. Wang, F. Brisset, A. Helbert, D. Solas, I. Drouelle, M. Mathon, T. Baudin. Influence of stored energy on twin formation during primary recrystallization, *Mat. Sci, Eng. A* 589 (2014) 112-118.
- [160] I. Karaman, H. Sehitoglu, H. Maier, Y. Chumlyakov. Competing mechanisms and modeling of deformation in austenitic stainless steel single crystals with and without nitrogen, *Acta Mater.* 49 (2001) 3919-3933.
- [161] V. Kutumbarao, T. Rajagopalachary. *Hot Workability and Processing Maps*, (1994).
- [162] Sivaprasad PV. Hot deformation behavior of 15Cr-15Ni-2.2 Mo-Ti modified stainless steels and 9Cr-1Mo Ferritic Steels: A study using processing maps and process modelling. vol. PhD. Bombay: Indian Institute of Technology, 1997.
- [163] S. Venugopal, P. Sivaprasad. A journey with Prasad's processing maps, *J. Mater. Eng. Perform.* 12 (2003) 674-686.
- [164] H. Ziegler. Some extremum principles in irreversible thermodynamics, with application to continuum mechanics, *Progress in solid mech.*, vol. 4 (1963) 93-193.
- [165] P.E. Wellstead. *Introduction to physical system modelling*, Academic Press London, 1979.
- [166] I. Prigogine. Time, structure, and fluctuations, *Science* 201 (1978) 777-785.
- [167] Y. Prasad, T. Seshacharyulu. Modelling of hot deformation for microstructural control, *Int. Mater. Rev.* 43 (1998) 243-258.
- [168] Y. Prasad, H. Giegel, S. Doraiavelu, J. Malas, J. Morgan, K. Lark, D. Barker. Modeling of dynamic material behavior in hot deformation: forging of Ti-6242, *Metall. Trans. A* 15 (1984) 1883-1892.
- [169] D. Samantaray, S. Mandal, A. Bhaduri. Optimization of hot working parameters for thermo-mechanical processing of modified 9Cr-1Mo (P91) steel employing dynamic materials model, *Mat. Sci, Eng. A* 528 (2011) 5204-5211.

- [170] J. Jonas, R. Holt, C. Coleman. Plastic stability in tension and compression, *Acta Metall.* 24 (1976) 911-918.
- [171] S. Semiatin, G. Lahoti. Deformation and unstable flow in hot forging of Ti-6Al-2Sn-4Zr-2Mo-0.1 Si, *Metall. Trans. A* 12 (1981) 1705-1717.
- [172] D. Rittel, P. Landau, A. Venkert. Dynamic recrystallization as a potential cause for adiabatic shear failure, *Phys. Rev. Lett.* 101 (2008) 165501.
- [173] M.A. Meyers, V.F. Nesterenko, J.C. LaSalvia, Q. Xue. Shear localization in dynamic deformation of materials: microstructural evolution and self-organization, *Mat. Sci., Eng. A* 317 (2001) 204-225.
- [174] D. Hughes, M. Kassner, M. Stout, J. Vetrano. Metal forming at the center of excellence for the synthesis and processing of advanced materials, *JOM* 50 (1998) 16-21.
- [175] P. Landau, A. Venkert, D. Rittel. Microstructural aspects of adiabatic shear failure in annealed Ti6Al4V, *Metall. Mater. Trans. A* 41 (2010) 389-396.
- [176] A.v. Granato, K. Lücke. Theory of mechanical damping due to dislocations, *J. Appl. Phys.* 27 (1956) 583-593.
- [177] A. Rollett, F. Humphreys, G.S. Rohrer, M. Hatherly. *Recrystallization and related annealing phenomena*, Elsevier, 2004.
- [178] D. Rittel. A different viewpoint on adiabatic shear localization, *J. Phys. D: Appl. Phys.* 42 (2009) 214009.
- [179] Q. Xue, E. Cerreta, G. Gray. Microstructural characteristics of post-shear localization in cold-rolled 316L stainless steel, *Acta Mater.* 55 (2007) 691-704.
- [180] D.T. Pierce, J.A. Jiménez, J. Bentley, D. Raabe, C. Oskay, J. Wittig. The influence of manganese content on the stacking fault and austenite/ ϵ -martensite interfacial energies in Fe-Mn-(Al-Si) steels investigated by experiment and theory, *Acta Mater.* 68 (2014) 238-253.
- [181] L. Kaufman, H. Bernstein. *Computer calculation of phase diagrams. With special reference to refractory metals*, (1970).
- [182] Y. Ishikawa, Y. Endoh. Antiferromagnetism of γ -FeMn Alloys, *J. Appl. Phys.* 39 (1968) 1318-1319.
- [183] M. Hillert, M. Jarl. A model for alloying in ferromagnetic metals, *Calphad* 2 (1978) 227-238.
- [184] G. Inden. The role of magnetism in the calculation of phase diagrams, *Physica B+C* 103 (1981) 82-100.
- [185] W. Huang. An assessment of the Fe-Mn system, *Calphad* 13 (1989) 243-252.

- [186] H. Suzuki. Dislocations and mechanical properties of crystals, New York (1957) 361.
- [187] T. Kamino, Y. Ueki, H. Hamajima, K. Sasaki, K. Kuroda, H. Saka. Direct evidence for Suzuki segregation obtained by high-resolution analytical electron microscopy, *Philos. Mag. Lett.* 66 (1992) 27-31.
- [188] K. Tauer. *RJ Weiss J. Phys. Ghent. Solids*, 4 (1958), *J. Phys. Ghent. Solids* 4 (1958) 135.
- [189] V. Pecherskaya, D. Bolshutkin, V.Y. Ilichev. Peculiarities of the electrical resistivity and structural-magnetic transformations in Fe-18r-(10–25) Ni steels at low temperatures, *Cryogenics* 19 (1979) 261-264.
- [190] A.F. Guillermet. An assessment of the Fe- Mo system, *Calphad* 6 (1982) 127-140.
- [191] K. Ishida. Direct estimation of stacking fault energy by thermodynamic analysis, *physica status solidi (a)* 36 (1976) 717-728.
- [192] T. Ericsson. On the Suzuki effect and spinodal decomposition, *Acta Metall.* 14 (1966) 1073-1084.
- [193] S. Chen, C. Chung, C. Yan, T. Hsu. Effect of fcc antiferromagnetism on martensitic transformation in Fe–Mn–Si based alloys, *Mat. Sci, Eng. A* 264 (1999) 262-268.
- [194] J.-O. Andersson. A thermodynamic evaluation of the Fe- Mo-C system, *Calphad* 12 (1988) 9-23.
- [195] S. Cotes, M. Sade, A.F. Guillermet. Fcc/Hcp martensitic transformation in the Fe-Mn system: Experimental study and thermodynamic analysis of phase stability, *Metall. Mater. Trans. A* 26 (1995) 1957-1969.
- [196] C. Ko, R. McLellan. Thermodynamics of ternary nitrogen austenites, *Acta Metall.* 31 (1983) 1821-1827.

Appendix

A) Thermodynamic calculation of stacking fault Energy

The SFE is represented by a function of change in free energy (ΔG) due to the transition from FCC (γ) to HCP (ζ) phase in the faulted layer. On the basis of this hypothesis, the SFE is represented as [141]:

$$\gamma_{SFE} = 2\sigma_{IE} + 2\psi(\Delta G_{bulk}^{\gamma \rightarrow \zeta} + \Delta G_{Mag}^{\gamma \rightarrow \zeta} + \Delta G_{Seg}^{\gamma \rightarrow \zeta}) \quad (i)$$

where σ_{IE} is the interfacial energy in the faulted region, ψ is the molar surface density, $\Delta G_{bulk}^{\gamma \rightarrow \zeta}$, $\Delta G_{Mag}^{\gamma \rightarrow \zeta}$ and $\Delta G_{Seg}^{\gamma \rightarrow \zeta}$ are the changes in bulk free energy, magnetic free energy and free energy due to segregation, respectively. The value of σ_{IE} for (111) plane has been taken as 8 mJm^{-2} as suggested by Curtze et al. [141]. The value of ψ has been calculated using the equation given by Pierce et al. [180]:

$$\psi = \frac{4}{\sqrt{3}N_A a^2} \quad (ii)$$

where N_A and a are the Avogadro number and lattice parameter, respectively. The lattice parameter of the 316LN used in this study has been found to be $\sim 3.6 \text{ \AA}$ from XRD line profile analysis using the Rietveld refinement method [109].

The $\Delta G_{bulk}^{\gamma \rightarrow \zeta}$ depends on the chemical composition of the alloy, and has two components; contribution from substitutional elements and contribution from interstitial elements:

$$\Delta G_{bulk}^{\gamma \rightarrow \zeta} = \Delta G_{b(sub)}^{\gamma \rightarrow \zeta} + \Delta G_{b(int)}^{\gamma \rightarrow \zeta} \quad (iii)$$

The contribution of substitutional elements to change in bulk free energy is given by:

$$\Delta G_{b(sub)}^{\gamma \rightarrow \zeta} = \sum_i \chi_i \Delta G_{(sub)i}^{\gamma \rightarrow \zeta} + \sum_{ij} \chi_i \chi_j \Omega_{ij}^{\gamma \rightarrow \zeta} \quad (iv)$$

where $\Delta G_{(sub)i}^{\gamma \rightarrow \zeta}$ represents the contribution from 'ith' substitutional element and $\Omega_{ij}^{\gamma \rightarrow \zeta}$ is the excess free energy due to formation of stable compound by 'ith' and 'jth' elements. χ_i represents the mole fraction of 'ith' element. For the present alloy used in this study, Eq. iv can be written as:

$$\Delta G_{b(sub)}^{\gamma \rightarrow \zeta} = \left[\begin{aligned} & \left(\chi_{Fe} \Delta G_{Fe}^{\gamma \rightarrow \zeta} + \chi_{Mn} \Delta G_{Mn}^{\gamma \rightarrow \zeta} + \chi_{Cr} \Delta G_{Cr}^{\gamma \rightarrow \zeta} + \chi_{Ni} \Delta G_{Ni}^{\gamma \rightarrow \zeta} + \chi_{Si} \Delta G_{Si}^{\gamma \rightarrow \zeta} + \chi_{Mo} \Delta G_{Mo}^{\gamma \rightarrow \zeta} \right) \\ & + \left(\chi_{Fe} \chi_{Mn} \Omega_{FeMn}^{\gamma \rightarrow \zeta} + \chi_{Fe} \chi_{Cr} \Omega_{FeCr}^{\gamma \rightarrow \zeta} + \chi_{Fe} \chi_{Ni} \Omega_{FeNi}^{\gamma \rightarrow \zeta} + \chi_{Fe} \chi_{Mo} \Omega_{FeMo}^{\gamma \rightarrow \zeta} + \chi_{Fe} \chi_{Si} \Omega_{FeSi}^{\gamma \rightarrow \zeta} + \chi_{Cr} \chi_{Ni} \Omega_{CrNi}^{\gamma \rightarrow \zeta} \right) \end{aligned} \right] \quad (v)$$

Bulk free energy change due to interstitial element (N), $\Delta G_{b(int)}^{\gamma \rightarrow \zeta}$, is mathematically represented as [143]:

$$\Delta G_{b(\text{int})}^{\gamma \rightarrow \zeta} = \chi_{\lambda} \Delta G_{(\text{int})\lambda}^{\gamma \rightarrow \zeta} \quad (\text{vi})$$

where χ_{λ} represents the mole fraction of the interstitial element ‘ λ ’ and $\Delta G_{(\text{int})\lambda}^{\gamma \rightarrow \zeta}$ represents the contribution from interstitial element ‘ λ ’ (here $\lambda = \text{C, N}$). This has been calculated by the method of Yakubstov et al. [143]:

$$\Delta G_{(\text{int})\lambda}^{\gamma \rightarrow \zeta} = 6 \left[\begin{aligned} & \frac{(U_{\text{Mo}\lambda}^{\zeta} - U_{\text{Mo}\lambda}^{\gamma}) + \frac{(U_{\text{Fe}\lambda}^{\zeta} - U_{\text{Mo}\lambda}^{\zeta})\chi_{\text{Fe}}}{\exp\left[\frac{(U_{\text{Fe}\lambda}^{\zeta} - U_{\text{Mn}\lambda}^{\zeta})}{RT}\right] + \frac{\chi_{\text{Cr}}}{\exp\left[\frac{(U_{\text{Fe}\lambda}^{\zeta} - U_{\text{Cr}\lambda}^{\zeta})}{RT}\right]} + \frac{\chi_{\text{Ni}}}{\exp\left[\frac{(U_{\text{Fe}\lambda}^{\zeta} - U_{\text{Ni}\lambda}^{\zeta})}{RT}\right]} + \frac{\chi_{\text{Mo}}}{\exp\left[\frac{(U_{\text{Fe}\lambda}^{\zeta} - U_{\text{Mo}\lambda}^{\zeta})}{RT}\right]}}{\chi_{\text{Fe}} + \frac{\chi_{\text{Mn}}}{\exp\left[\frac{(U_{\text{Cr}\lambda}^{\zeta} - U_{\text{Mn}\lambda}^{\zeta})}{RT}\right]} + \chi_{\text{Cr}} + \frac{\chi_{\text{Ni}}}{\exp\left[\frac{(U_{\text{Cr}\lambda}^{\zeta} - U_{\text{Ni}\lambda}^{\zeta})}{RT}\right]} + \frac{\chi_{\text{Mo}}}{\exp\left[\frac{(U_{\text{Cr}\lambda}^{\zeta} - U_{\text{Mo}\lambda}^{\zeta})}{RT}\right]}} \\ & + \frac{(U_{\text{Cr}\lambda}^{\zeta} - U_{\text{Mo}\lambda}^{\zeta})\chi_{\text{Cr}}}{\exp\left[\frac{(U_{\text{Cr}\lambda}^{\zeta} - U_{\text{Fe}\lambda}^{\zeta})}{RT}\right] + \frac{\chi_{\text{Mn}}}{\exp\left[\frac{(U_{\text{Cr}\lambda}^{\zeta} - U_{\text{Mn}\lambda}^{\zeta})}{RT}\right]} + \chi_{\text{Cr}} + \frac{\chi_{\text{Ni}}}{\exp\left[\frac{(U_{\text{Cr}\lambda}^{\zeta} - U_{\text{Ni}\lambda}^{\zeta})}{RT}\right]} + \frac{\chi_{\text{Mo}}}{\exp\left[\frac{(U_{\text{Cr}\lambda}^{\zeta} - U_{\text{Mo}\lambda}^{\zeta})}{RT}\right]}} \\ & + \frac{(U_{\text{Ni}\lambda}^{\zeta} - U_{\text{Mo}\lambda}^{\zeta})\chi_{\text{Ni}}}{\exp\left[\frac{(U_{\text{Ni}\lambda}^{\zeta} - U_{\text{Fe}\lambda}^{\zeta})}{RT}\right] + \frac{\chi_{\text{Mn}}}{\exp\left[\frac{(U_{\text{Ni}\lambda}^{\zeta} - U_{\text{Mn}\lambda}^{\zeta})}{RT}\right]} + \frac{\chi_{\text{Cr}}}{\exp\left[\frac{(U_{\text{Ni}\lambda}^{\zeta} - U_{\text{Cr}\lambda}^{\zeta})}{RT}\right]} + \chi_{\text{Ni}} + \frac{\chi_{\text{Mo}}}{\exp\left[\frac{(U_{\text{Ni}\lambda}^{\zeta} - U_{\text{Mo}\lambda}^{\zeta})}{RT}\right]}} \\ & + \frac{(U_{\text{Mn}\lambda}^{\zeta} - U_{\text{Mo}\lambda}^{\zeta})\chi_{\text{Mn}}}{\exp\left[\frac{(U_{\text{Mn}\lambda}^{\zeta} - U_{\text{Fe}\lambda}^{\zeta})}{RT}\right] + \frac{\chi_{\text{Mo}}}{\exp\left[\frac{(U_{\text{Mn}\lambda}^{\zeta} - U_{\text{Mo}\lambda}^{\zeta})}{RT}\right]} + \frac{\chi_{\text{Cr}}}{\exp\left[\frac{(U_{\text{Mn}\lambda}^{\zeta} - U_{\text{Cr}\lambda}^{\zeta})}{RT}\right]} + \frac{\chi_{\text{Ni}}}{\exp\left[\frac{(U_{\text{Mn}\lambda}^{\zeta} - U_{\text{Ni}\lambda}^{\zeta})}{RT}\right]} + \chi_{\text{Mn}}} \\ & \frac{(U_{\text{Fe}\lambda}^{\gamma} - U_{\text{Mo}\lambda}^{\gamma})\chi_{\text{Fe}}}{\chi_{\text{Fe}} + \frac{\chi_{\text{Mn}}}{\exp\left[\frac{(U_{\text{Fe}\lambda}^{\gamma} - U_{\text{Mn}\lambda}^{\gamma})}{RT}\right]} + \frac{\chi_{\text{Cr}}}{\exp\left[\frac{(U_{\text{Fe}\lambda}^{\gamma} - U_{\text{Cr}\lambda}^{\gamma})}{RT}\right]} + \frac{\chi_{\text{Ni}}}{\exp\left[\frac{(U_{\text{Fe}\lambda}^{\gamma} - U_{\text{Ni}\lambda}^{\gamma})}{RT}\right]} + \frac{\chi_{\text{Mo}}}{\exp\left[\frac{(U_{\text{Fe}\lambda}^{\gamma} - U_{\text{Mo}\lambda}^{\gamma})}{RT}\right]}} \\ & - \frac{(U_{\text{Cr}\lambda}^{\gamma} - U_{\text{Mo}\lambda}^{\gamma})\chi_{\text{Cr}}}{\exp\left[\frac{(U_{\text{Cr}\lambda}^{\gamma} - U_{\text{Fe}\lambda}^{\gamma})}{RT}\right] + \frac{\chi_{\text{Mn}}}{\exp\left[\frac{(U_{\text{Cr}\lambda}^{\gamma} - U_{\text{Mn}\lambda}^{\gamma})}{RT}\right]} + \chi_{\text{Cr}} + \frac{\chi_{\text{Ni}}}{\exp\left[\frac{(U_{\text{Cr}\lambda}^{\gamma} - U_{\text{Ni}\lambda}^{\gamma})}{RT}\right]} + \frac{\chi_{\text{Mo}}}{\exp\left[\frac{(U_{\text{Cr}\lambda}^{\gamma} - U_{\text{Mo}\lambda}^{\gamma})}{RT}\right]}} \\ & - \frac{(U_{\text{Ni}\lambda}^{\gamma} - U_{\text{Mo}\lambda}^{\gamma})\chi_{\text{Ni}}}{\exp\left[\frac{(U_{\text{Ni}\lambda}^{\gamma} - U_{\text{Fe}\lambda}^{\gamma})}{RT}\right] + \frac{\chi_{\text{Mn}}}{\exp\left[\frac{(U_{\text{Ni}\lambda}^{\gamma} - U_{\text{Mn}\lambda}^{\gamma})}{RT}\right]} + \frac{\chi_{\text{Cr}}}{\exp\left[\frac{(U_{\text{Ni}\lambda}^{\gamma} - U_{\text{Cr}\lambda}^{\gamma})}{RT}\right]} + \chi_{\text{Ni}} + \frac{\chi_{\text{Mo}}}{\exp\left[\frac{(U_{\text{Ni}\lambda}^{\gamma} - U_{\text{Mo}\lambda}^{\gamma})}{RT}\right]}} \\ & - \frac{(U_{\text{Mo}\lambda}^{\gamma} - U_{\text{Mo}\lambda}^{\gamma})\chi_{\text{Mn}}}{\exp\left[\frac{(U_{\text{Mn}\lambda}^{\gamma} - U_{\text{Fe}\lambda}^{\gamma})}{RT}\right] + \frac{\chi_{\text{Mo}}}{\exp\left[\frac{(U_{\text{Mn}\lambda}^{\gamma} - U_{\text{Mo}\lambda}^{\gamma})}{RT}\right]} + \frac{\chi_{\text{Cr}}}{\exp\left[\frac{(U_{\text{Mn}\lambda}^{\gamma} - U_{\text{Cr}\lambda}^{\gamma})}{RT}\right]} + \frac{\chi_{\text{Ni}}}{\exp\left[\frac{(U_{\text{Mn}\lambda}^{\gamma} - U_{\text{Ni}\lambda}^{\gamma})}{RT}\right]} + \chi_{\text{Mn}}} \end{aligned} \right] \quad (\text{vii})$$

where $U_{i\lambda}^{\gamma} - U_{j\lambda}^{\gamma} = \Delta U_{ij}^{\gamma}$, represents the change in interaction energy between λ and each substitutional alloying element pair i - j , in γ phase. Similarly, $U_{i\lambda}^{\zeta} - U_{j\lambda}^{\zeta} = \Delta U_{ij}^{\zeta}$ represents the change in interaction energy between λ and each substitutional alloying element pair i - j , in ζ phase. The values of ΔU_{ij}^{γ} are given in Table I. To calculate the values of ΔU_{ij}^{ζ} , the equation proposed by Kaufman et al. [181] and Ishikawa et al. [182] has been used:

$$\Delta U_{ij}^{\zeta} = \Delta U_{ij}^{\gamma} + (\Delta G_i^{\gamma \rightarrow \zeta} - \Delta G_j^{\gamma \rightarrow \zeta}) \quad (\text{viii})$$

The alloy used for the present study contains two distinct interstitial elements (C and N). To represent the change in bulk free energy due to these elements, the original Eq. vi, as given in [143], has been modified as:

$$\Delta G_{b(\text{int})}^{\gamma \rightarrow \zeta} = \chi_N \Delta G_N^{\gamma \rightarrow \zeta} + \chi_C \Delta G_C^{\gamma \rightarrow \zeta} \quad (\text{ix})$$

The second component of free energy change is the change associated with magnetic transitions. The following equation describes the change associated with the anti-ferromagnetic-to-paramagnetic transition (Neel transition) of each phase [140]:

$$\Delta G_{Mag}^{\gamma \rightarrow \zeta} = G_{Mag}^{\gamma} - G_{Mag}^{\zeta} \quad (\text{x})$$

where G_{Mag}^{γ} and G_{Mag}^{ζ} are the change in magnetic free energy for γ and ε phase, respectively. These values have been estimated using a modified-Hillert-Jarl model [183] proposed by Inden [184]:

$$G_{Mag}^{\gamma} = K^{\gamma} RT \ln(\beta^{\gamma} + 1) \quad (\text{xi.a})$$

$$G_{Mag}^{\zeta} = K^{\zeta} RT \ln(\beta^{\zeta} + 1) \quad (\text{xi.b})$$

where R' is the universal gas constant and T is the absolute temperature where the change in free energy is calculated. The parameter β is magnetic moment and is calculated using the following equations given in [140, 141, 181, 184, 185]:

$$\beta^{\gamma} = 0.7\chi_{Fe} + 0.62\chi_{Mn} + 0.62\chi_{Ni} - 0.8\chi_{Cr} - 0.64\chi_{Fe}\chi_{Mn} - 4\chi_C \quad (\text{xii})$$

$$\beta^{\zeta} = 0.62\chi_{Mn} - 4\chi_C \quad (\text{xiii})$$

The parameters K^{γ} and K^{ζ} given in Eq. (xi.a) and (xi.b) are represented by the following functions [186-188]:

$$K^{\Phi} = 1 - \frac{1}{D} \left[\frac{79 \left(\frac{T}{T_{Neel}^{\Phi}} \right)^{-1}}{140p} + \frac{474 \left(\frac{1}{p} - 1 \right)}{494} \left(\frac{\left(\frac{T}{T_{Neel}^{\Phi}} \right)^3}{6} + \frac{\left(\frac{T}{T_{Neel}^{\Phi}} \right)^9}{135} + \frac{\left(\frac{T}{T_{Neel}^{\Phi}} \right)^{15}}{600} \right) \right] \text{ if } \frac{T}{T_{Neel}^{\Phi}} \leq 1, \Phi = \gamma, \zeta \quad (\text{xiv})$$

and

$$K^{\Phi} = -\frac{1}{D} \left[\frac{\left(\frac{T}{T_{Neel}^{\Phi}} \right)^{-5}}{10} + \frac{\left(\frac{T}{T_{Neel}^{\Phi}} \right)^{-15}}{315} + \frac{\left(\frac{T}{T_{Neel}^{\Phi}} \right)^{-25}}{1500} \right] \text{ if } \frac{T}{T_{Neel}^{\Phi}} > 1, \Phi = \gamma, \zeta \quad (\text{xv})$$

where the Neel temperature, T_{Neel} of each phase is calculated using the empirical relations given by Curtze et al. [141] and Pecherskaya et al. [189]:

$$T_{Neel}^{\gamma} = 90 - (1.25\chi_{Cr}) - (2.75\chi_{Ni}) - (5.5\chi_{Mo}) - (14\chi_{Si}) + (7.75\chi_{Mn}) \quad (\text{xvi})$$

$$T_{Neel}^{\zeta} = 580\chi_{Mn} \quad (xvii)$$

The parameter D used in Eq.xiv-xv has been calculated using:

$$D = \left[\frac{518}{1125} + \frac{11692}{15975} \left(\frac{1}{p} - 1 \right) \right] \quad (xviii)$$

where p is the fraction of magnetic enthalpy absorbed above T_{Neel} ; typical values for FCC and HCP being 0.28 [143]. In the calculation of $\Delta G_{mag}^{\gamma \rightarrow \zeta}$, the contribution of Si, C, N and Mo has not been taken into account since the effect of these elements on $\Delta G_{mag}^{\gamma \rightarrow \zeta}$ has been reported to be trivial [141, 190]. Finally, the effect of segregation has three components; chemical segregation due to Suzuki interaction, surface segregation between matrix and stacking fault, and elastic segregation effect due to difference in atomic size. This is mathematically defined as [191]:

$$\Delta G_{Seg}^{\gamma \rightarrow \zeta} = \Delta G_{chemical}^{\gamma \rightarrow \zeta} + \Delta G_{surface}^{\gamma \rightarrow \zeta} + \Delta G_{elastic}^{\gamma \rightarrow \zeta} \quad (xix)$$

The free energy change due to chemical segregation is given by:

$$\Delta G_{chemical}^{\gamma \rightarrow \varepsilon} = RT \left[\chi_N \ln \frac{\chi_{N(Seg)}}{\chi_N} + (1 - \chi_N) \ln \frac{(1 - \chi_{N(Seg)})}{(1 - \chi_N)} \right] \quad (xx)$$

where $\chi_{N(Seg)}$ is fraction of nitrogen segregated in the faulted region, and can be calculated as per the following equation used by Yakubtsov [143]:

$$\chi_{N(Seg)} = \left[1 + \frac{1 - \chi_N}{\chi_N} \exp \left(\frac{-\Lambda}{RT} \right) \right]^{-1} \quad (xxi)$$

where Λ denotes the interaction energy between nitrogen atom and dislocations in FCC matrix and is represented by a polynomial function of nitrogen content in the alloy [143]:

$$\Lambda = 5.62 + 39800.93N - 129734.85N^2 + 151349N^3 \quad (xxii)$$

where N symbolizes the nitrogen content in % (by weight).

Change in free energy due to surface segregation has been proposed by Ericsson et al. [192] as

$$\Delta G_{surface}^{\gamma \rightarrow \zeta} = 0.25\Lambda(\chi_{N(Seg)} - \chi_N)^2 \quad (xxiii)$$

The effect of elastic segregation on free energy proposed by Suzuki [186] is given by:

$$\Delta G_{elastic}^{\gamma \rightarrow \zeta} = 0.23G' \frac{1+\nu}{1-\nu} \left(\frac{dV}{dX} \right) \frac{1}{V} (\chi_{N(Seg)} - \chi_N)^2 \quad (xxiv)$$

where G' , ν and V represent the shear modulus, Poisson's ratio and molar volume of the alloy, respectively.

Table I: Values of various parameters and functions used for the thermodynamic calculation of stacking fault energy.

Thermodynamic Variable	Value(Jmol ⁻¹)	Reference
$\Delta G_{Fe}^{\gamma \rightarrow \zeta}$	-2243.38+4.309T	[191]
$\Delta G_{Mn}^{\gamma \rightarrow \zeta}$	-1000+1.123T	[191]
$\Delta G_{Cr}^{\gamma \rightarrow \zeta}$	1370-0.163T	[141]
$\Delta G_{Ni}^{\gamma \rightarrow \zeta}$	1046+1.255T	[141]
$\Delta G_{Mo}^{\gamma \rightarrow \zeta}$	-3776.47-0.3517T	[142]
$\Delta G_{Si}^{\gamma \rightarrow \zeta}$	-560-8T	[184]
$\Omega_{FeMn}^{\gamma \rightarrow \zeta}$	2873 - 717($\chi_{Fe} - \chi_{Mn}$)	[193]
$\Omega_{FeCr}^{\gamma \rightarrow \zeta}$	2095	[143]
$\Omega_{FeNi}^{\gamma \rightarrow \zeta}$	2095	[141]
$\Omega_{FeMo}^{\gamma \rightarrow \zeta}$	1495	[194]
$\Omega_{FeSi}^{\gamma \rightarrow \zeta}$	2850 - 3520($\chi_{Fe} - \chi_{Si}$)	[184]
$\Omega_{CrNi}^{\gamma \rightarrow \zeta}$	4190	[141]
$U_{FeN}^{\gamma} - U_{MnN}^{\gamma}$	8800	[195]
$U_{FeN}^{\gamma} - U_{CrN}^{\gamma}$	18800	[196]
$U_{FeN}^{\gamma} - U_{NiN}^{\gamma}$	-17000	[196]
$U_{FeN}^{\gamma} - U_{MoN}^{\gamma}$	71404	[196]
$U_{CrN}^{\gamma} - U_{MnN}^{\gamma}$	-10000	[195]
$U_{NiN}^{\gamma} - U_{MnN}^{\gamma}$	25800	[195]
$U_{MnN}^{\gamma} - U_{MoN}^{\gamma}$	57558	[196]
$U_{CrN}^{\gamma} - U_{NiN}^{\gamma}$	35800	[141]
$U_{CrN}^{\gamma} - U_{MoN}^{\gamma}$	56680	[196]
$U_{NiN}^{\gamma} - U_{MoN}^{\gamma}$	90342	[196]
$U_{FeC}^{\gamma} - U_{MnC}^{\gamma}$	-7699	[196]
$U_{FeC}^{\gamma} - U_{CrC}^{\gamma}$	12307	[196]
$U_{FeC}^{\gamma} - U_{NiC}^{\gamma}$	7795	[196]
$U_{FeC}^{\gamma} - U_{MoC}^{\gamma}$	47139	[196]
$U_{CrC}^{\gamma} - U_{MnC}^{\gamma}$	-1315	[196]
$U_{NiC}^{\gamma} - U_{MnC}^{\gamma}$	12202	[196]

$U_{MnC}^\gamma - U_{MoC}^\gamma$	36148	[196]
$U_{CrC}^\gamma - U_{NiC}^\gamma$	16809	[196]
$U_{CrC}^\gamma - U_{MoC}^\gamma$	31540	[196]
$U_{NiC}^\gamma - U_{MoC}^\gamma$	51642	[196]

B) Equation involved in calculation of microstrain and stacking fault probability

The peak broadening width (B_r) in X-ray diffraction profile is due to combined effect of microstrain (B_{strain}) and crystallite size (B_{size}). These can be expressed as

$$B_r = B_{size} + B_{strain}$$

$$B_r = \frac{k\lambda}{L \cos \theta_b} + \vartheta \tan \theta_b \quad (xxv)$$

where λ is the wavelength of the x-rays used, θ_b is the Bragg's angle, L is the average crystallite size measured in a direction perpendicular to the surface of the specimen, ϑ is the microstrain and k is a constant.

Similarly, from the measured peak $\Delta(2\theta_b)$, we can obtain the Stacking fault probability (α_p) directly as [144]

$$\Delta(2\theta_b) = \frac{90\sqrt{3}\alpha_p \tan \theta_b}{\pi^2 h_o^2 (u+b)} \sum_b \pm L \quad (xxvi)$$

The details about the notations are reported by Warren et al [146].